Design, Implementation, and Calibration of Half-Wave Plate Polarimetry for the E and B Experiment

A DISSERTATION
SUBMITTED TO THE FACULTY OF THE GRADUATE SCHOOL
OF THE UNIVERSITY OF MINNESOTA
BY

Jeffrey Michael Klein

IN PARTIAL FULFILLMENT OF THE REQUIREMENTS
FOR THE DEGREE OF
Doctor of Philosophy

Professor Shaul Hanany

October, 2014

Acknowledgements

This scientific pursuit, like all of them, is my best attempt at empericism and objectivity. But the process of creating it was very much a human one, enabled by people who I wish to give my graditute for their intellectual and emotional support.

I want to thank the entire EBEX collaboration, and specifically the EBEX field team and UMN cosmology lab; those who were there with me on late, hot Texas nights: François Aubin, Chaoyun Bao, Daniel Chapman, Joy Didier, Matt Dobbs, Seth Hillbrand, Kyle Helson, Hannes Hubmayr, Andrei Korotkov, Michele Limon, Kevin MacDermid, Tomotake Matsumura, Amber Miller, Michael Milligan, Dan Polsgrove, Kate Raach, Britt Reichborn-Kjennerud, and Ben Westbrook. I want to give special mention to those whom I worked with the closest, Asad Aboobaker and Kyle Zilic; without their infinite patience during the darkest moments of this journey I would never have completed it. Not only working with, but living with, traveling with, and recreating with this group has been one of the most rewarding aspects of my life.

My thanks to my advisor, Shaul Hanany, for his leadership and his success in teaching me a few things, even when I resisted.

To Jon Kilgore and the rest of the UMN research machine shop; your knowledge and skill made it possible for clueless graduate students to design and build a telescope from the ground up.

To my long-suffering parents; your infinite patience, support, and love that is apparently not conditional on actual employment is a gift for which I cannot thank you enough.

To my friends and girlfriend; I can't understate the importance of having something I valued outside of the world of physics.

I want to acknowledge funding from the Minnesota Space Grant Foundation, NASA, and in particular thank the CSBF team for putting up with us; we're all aware we were a special challenge. And finally, to the good people of the great state of Minnesota; it is your unfailing support of the University of Minnesota that gave me a home at which to do my work; thank you.

Abstract

The E and B Experiment (EBEX) is a balloon-borne telescope designed to measure the polarization of the Cosmic Microwave Background (CMB) and dust foregrounds at 10' scales and three frequency bands of 150 GHz, 250 GHz, and 410 GHz in order to detect or constrain B-mode polarization. Results may provide evidence to support the theory of cosmological inflation, or constrain specific models.

EBEX's polarization measurement capability is implemented via continuously-rotating Half-Wave Plate (HWP) polarimetry. We discuss the design and implementation of the polarimetry hardware for the E and B Experiment (EBEX). In order to achieve low-temperature rotation of our 15 cm, 635 g achromatic HWP stack, we implement a unique application of a Superconducting Magnetic Bearing (SMB), building off an earlier prototype. We discuss design constraints, detail our implementation, and present results of tests of power dissipation, rotation speed stability, dynamic stability, and operational lifetime. We find power dissipation of 15 mW in our LDB configuration, and achieve successful operation of the system in both a 2009 test flight and a 2012 Long Duration (LDB) flight.

We design and carry out calibration tests to verify our ability to measure polarized signals. We develop a data analysis pipeline to extract polarization measurements from the chopped polarized signals we use in calibration; we verify and optimize the performance of this pipeline with a simulation. We find that a thorough understanding of the time constants of EBEX's bolometric sensors is essential to measure polarization. We develop methods to measure and remove the effects of these time constants. Tests of polarization rotation across our bands verify predictions of rotation due to our achromatic HWP 5-stack. Polarized beam scans allow us to set an absolute calibration for EBEX with a standard deviation of 1.5°.

Contents

List of Tables

List of Figures

Chapter 1

Cosmological inflation, polarization of the CMB, and the E and B Experiment

1.1 Cosmological inflation

Our universe is well-described by the Λ Cold Dark Matter model (ΛCDM). The model posits an expanding universe in terms of three contributions to its energy density: ordinary baryonic matter, dark matter, and dark energy, which today we observe at ratios of 4.6%, 22.7%, and 72.8% respectively. To these is added three more parameters: the curvature fluctuation amplitude, the optical depth at reionization, which defines when young starlight began to ionize hydrogen after the "dark ages" period, and the scalar spectral index, the index of the amplitude power spectrum which is near unity (that is, currently consistent with scale invariant). This simple six-parameter model is consistent with the observed Cosmic Microwave Background (CMB), as well as observations of the Hubble parameter, baryon acoustic oscillation (BAO), and the abundance of elements.

The consistency we find with this model presents some puzzles. We consider two illustrative ones: the apparent flatness of the universe, which begs for an explanation beyond fine-tuning, and the largely isotropic CMB, which appears to be a remnant of a fully-thermalized plasma. In a naive model it is not clear why we see such apparent thermalization in the CMB when looking in opposite directions, since these patches should never have been in causal contact with each other (in fact, it can be shown using the ΛCDM model that patches only 2°apart on the sky

were never in causal contact in a naive model of the universe).

These puzzles suggest a potential solution: both would be explained by a rapid expansion in the size of the universe at an early time. Extant observations constrain such a model to ending around 10^{-33} seconds from the universe's beginning, at which point an expansion on the order of 60 e-foldings has occurred. Most typically, inflationary theory supposes an "inflaton" field, which has a shallow potential and a "slow roll", with energy $\rho \propto \frac{1}{2}\phi^2 + \dot{V}(\phi)$. In this situation the Friedman equation gives

$$H^2 = \frac{1}{3M_{pl}^2}(\frac{\dot{\phi}^2}{2} + V(\phi)), \tag{1.1}$$

where M_{pl} is the Planck energy and H the Hubble constant during inflation. We then define two parameters for convenience,

$$\epsilon = \frac{M_{pl}^2}{2}(\frac{V'(\phi)}{V(\phi)})^2 \tag{1.2}$$

$$\eta = M_{pl}^2(\frac{V''(\phi)}{V(\phi)}) \tag{1.3}$$

where $V' \equiv \frac{dV(\phi)}{d\phi}$, the spatial derivative of V. To create exponential expansion, these parameters must be $<< 1$ to satisfy what is described as a "slow roll" situation. In this case, the scale factor $a(t) \propto e^{Ht}$.

Inflation has the added benefit of creating an origin for cosmological structure; quantum fluctuations in the space-time metric, when subjected to inflation, become a macroscopic power spectrum of density perturbations and primordial gravity waves such that

$$P_s(k) = P_s(k_*)(\frac{k}{k_*})^{n_s(k_*)-1+\frac{1}{2}\alpha_s(k_*)ln(k/k_*)} \tag{1.4}$$

$$P_t(k) = P_t(k_*)(\frac{k}{k_*})^{n_t(k_*)} \tag{1.5}$$

where P_s and P_t are the power levels of the scalar and tensor perturbations, k is the wave vector, n_s is the spectral index, α_s allows for a rate of change of this index, and k_* is an arbitrary reference point. We note a "tensor to scalar ratio" that is a function of the Planck energy in the case of slow-roll inflation:

$$r = \frac{P_t}{P_s} = \frac{M_{pl}^2}{\pi}(\frac{V'}{V})^2 \tag{1.6}$$

Measurement of this ratio is as direct a probe of the inflationary paradigm as we are aware of.

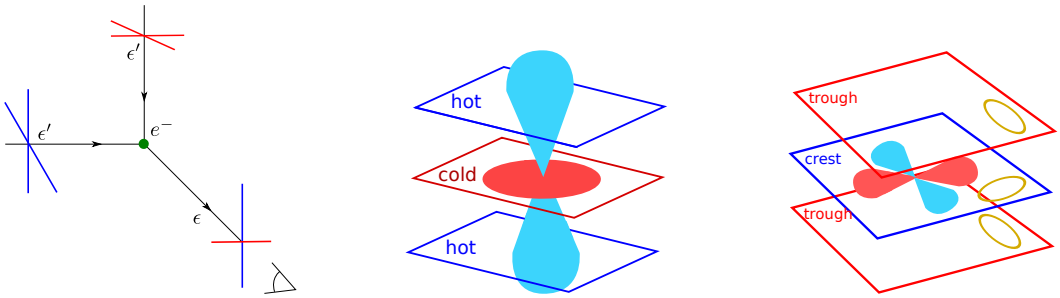

Figure 1.1: Left: Thompson scattering converts temperature anisotropies into polarized light. Center: An electron exposed to a scalar perturbation in k-space sees the quadrupole anisotropy Y_2^0. Right: An electron exposed to a tensor perturbation sees the quadrupole anisotropy $Y_2^{\pm 2}$. All figures in this section are adapted from Hu 1997 [1].

1.2 Polarization of the CMB

Local polarization of the CMB occurs due to Thompson scattering, when an electron in a sea of photons is subject to a quadrupole temperature anisotropy. This is the case in the universe until recombination, at which point protons and electrons combined to form neutral hydrogen.

The local scattering pattern for a given electron in the presence of a Fourier space inhomogeneity mode in terms of Stokes vectors Q and U is different depending on which quadrapole the electron is exposed to. The quadrapole moment can come from scalar (gravitational under and over-densities) or tensor (gravitational wave) configurations, and is governed by the Thompson scattering cross section $\frac{d\sigma_T}{d\Omega} \propto |\hat{\epsilon} \cdot \hat{\epsilon'}|^2$ (Figure 1.1, left). Specifically, in terms of the observer's angle θ and ϕ,

Scalar	Y_2^0	$Q = \sin^2\theta$	$U = 0$
Tensor	$Y_2^{\pm 2}$	$Q = (1 + \cos^2\theta)e^{2i\phi}$	$U = -2i\cos\theta e^{2i\phi}$

(Figure 1.1, center and right). These local configurations are modulated over the last scattering surface for all modes. We now consider the macroscopic polarization patterns in terms of E- (curl-free) and B- (divergence-free) modes. They have a property which survives integration over all modes, which is their differing parities: in the case of $\vec{x} \to -\vec{x}$, the E-modes are unchanged but the B-modes flip their sign. For a pure E-mode,

$$\frac{d^2U}{d\hat{\theta}^2} = \frac{d^2U}{d\hat{\phi}^2} \tag{1.7}$$

$$\frac{d^2Q}{d(\hat{\theta} + \hat{\phi})^2} = \frac{d^2Q}{d(\hat{\theta} - \hat{\phi})^2} \tag{1.8}$$

and for pure B-mode,

$$\frac{d^2Q}{d\hat{\theta}^2} = \frac{d^2Q}{d\hat{\phi}^2} \tag{1.9}$$

$$\frac{d^2U}{d(\hat{\theta}+\hat{\phi})^2} = \frac{d^2U}{d(\hat{\theta}-\hat{\phi})^2} \tag{1.10}$$

Since gravity wave perturbations and scalar perturbations produce different mixes of Q and U, they can be distinguished on the sky by searching for E and B-modes. A considerably more in-depth treatment of this topic can be found in Hu 1997 [1] or Dodelson [1]. The tensor (gravitational wave) signature is expressed as B-modes in the CMB; E-modes are a factor of r higher in signal are directly related to the primary temperature anisotropies.

1.3 EBEX and its science goals

1.3.1 EBEX science context

EBEX is a balloon-borne polarimetry telescope with observation frequencies at 150 GHz, 210 GHz, and 410 GHz. EBEX has an 8' beam and roughly 1200 TES bolometric cooled to 270 mK on two focal planes.

EBEX is designed with several science goals in mind:

- To measure the B-mode signature of primordial gravitational waves
- To measure B-mode polarization created via lensing of E-modes
- To characterize the galactic dust signature at mm-wave frequencies. Thermal emission from galactic dust is a foreground to the B-mode CMB signal; the best information currently available suggests that it is approximated by a modified 19 K black body with a power law emissivity.

During the course of EBEX's implementation and deployment, new data has been released regarding CMB polarization. Specifically, the BICEP2[3] (Figure 1.2) collaboration has claimed a preliminary detection of gravitational B-modes. However, as a ground-based single-frequency instrument, it was necessary for BICEP2 to use data from the Planck satellite to characterize the dust signal for subtraction. The interpretation of the BICEP2 data is contested ([4]) due to the lack of information on the spectral index and polarization fraction of dust in low-dust regions.

EBEX is on a balloon-based platform in order to have better access to the high frequencies that are necessary to constrain dust, and offers smaller angular scales and higher frequencies (410 GHz vs. 353 GHz) than Planck. EBEX and its successor, EBEX6k, will contribute valuable

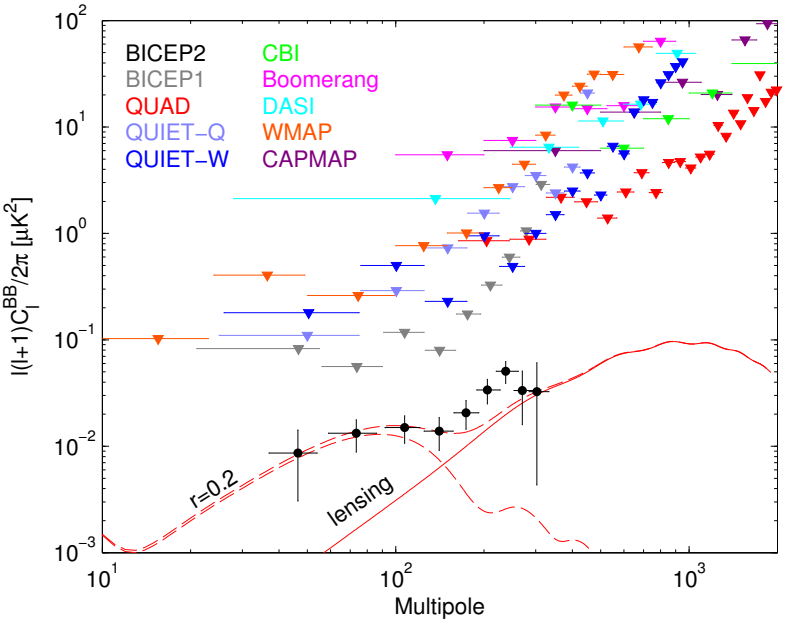

Figure 1.2: 95% upper limits from a selection of previous experiments and the claimed $r = 0.2$ detection by BICEP2. Signature from primordial gravitational waves are shown as a dashed line; contribution from E mode lensing as solid line. (Figure from BICEP2 [3])

information on the dust model, helping facilitate the subtraction of dust to and verify the validity of apparent gravitational wave B-mode detections.

1.3.2 Overview of the EBEX instrument

EBEX is an off-axis Gregorian telescope that focuses light onto two focal planes located in a cryogenic chamber (Figure 1.3). The chamber has two toroidal cryogen takes, with liquid helium filling the inner and liquid nitrogen the outer. Two intermediate sub-300 K stages serve as extra shields and are cooled with boiloff. A filtering scheme ([34]) allows in-band photons to enter the cryostat through a HDPE vacuum window while minimizing out-of-band photons. An ^{4}He/^{4}He closed-cycle adsorption refrigerator cools internal lenses to $\sim$ 950 mK while a ^{4}He/^{3}He/^{4}He refrigerator cools the focal planes to $\sim$ 250 mK (Figure 1.4). The fridges have a hold time of 2–3 days depending on loading specifics; they must be recycled several times during our 12-day flight.

Focal planes contain approximately 1200 operational Transition Edge Sensor bolometers (Figure 1.5) read out by custom multiplexed readout electronics designed by EBEX collaborators at McGill University. In-depth information on these detectors, their operation and noise

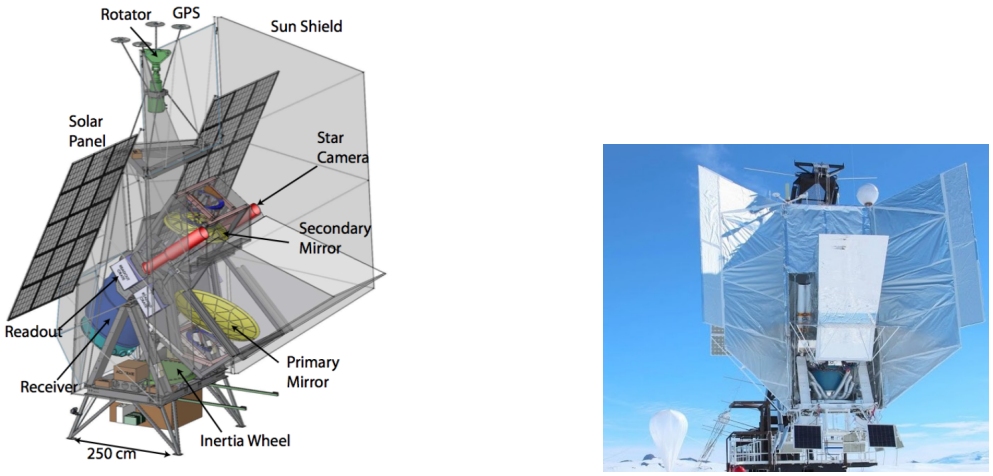

Figure 1.3: Left: A model shows EBEX in its launch configuration. The receiver and the rest of the optics reside on an inner frame that rotates relative to the outer frame. Right: EBEX before LDB launch, with the balloon filling in the background

performance, and the readout system can be found in [36, 37]. We discuss their characteristic time constants at length in this work as this particular property is closely related to measurment of polarization.

The EBEX gondola points in elevation via an actuator that rotates the inner frame from 20° to 60° relative to the outer frame (Figure 1.3); azimuth pointing is done via a motor/rotator at the top of the gondola, with added precision from an inertial rotator located underneath the cryostat on the outer frame. An Attitude Control System (ACS) measures EBEX pointing to 0.5° in real time and 9″ in post flight reconstruction ([38]), and controls EBEX's scanning strategy, which nominally called for 15° throws at speeds of $0.4°/s$. The system consists of absolute pointing via star camera ([35]) at the end of each throw, with inter-throw integration performed by gyroscopes and a magnetometer, and additional relative and absolute sensors ([39]).

Data from all systems is piped into redundant pressure vessel storage via two redundant flight control computers running the Flight Control Program (FCP). FCP controls pointing, and electrical commanding via General Housekeeping Boards (GHKs) developed by collaborators at the Weizmann Institute ([8]). It is this system that interfaces with the HWP system control electronics and readout discussed in section 2.3. A small subset of the data is downlinked via line-of-sight (LOS) and later relay satellite (TDRSS) and Iridium satellite; additionally, commanding is available via these systems most of flight. Downlink prioritization software ([40]) allowed for occasional downlinking of HWP readout data, discussed in section 2.5.1, to verify HWP operation.

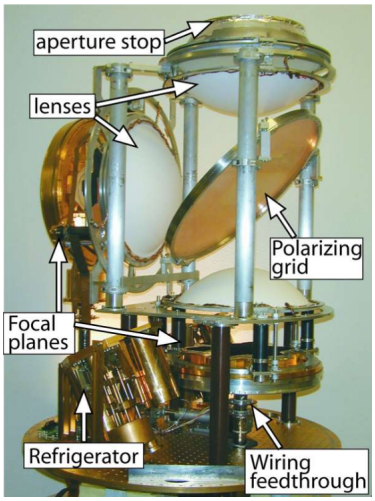

Figure 1.4: The EBEX ∼1 K lenses and focal planes reside inside the cryostat. Light enters the cryostat through a window above the aperture stop, passes through the HWP (not shown), and is split by a polarizing grid. Lenses then focus the light on to two focal plans, one horizontal (H) and one vertical (V).

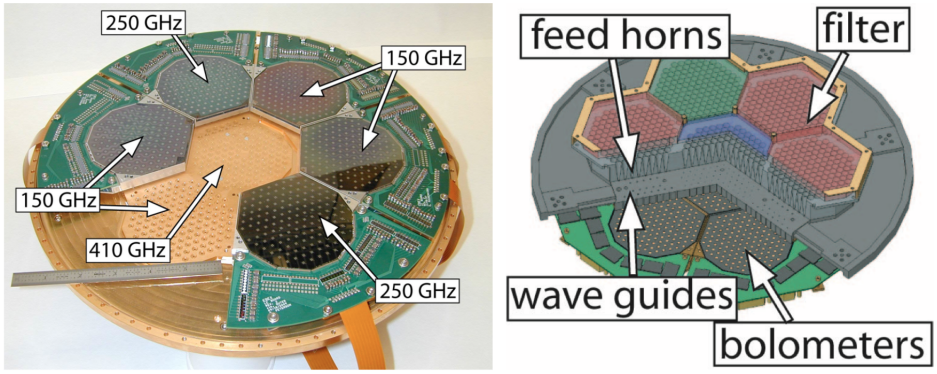

Figure 1.5: Left: EBEX focal plane photograph shows the detectors and cold readout electronics. Right: A model shows the detectors in situ with the feed horns.

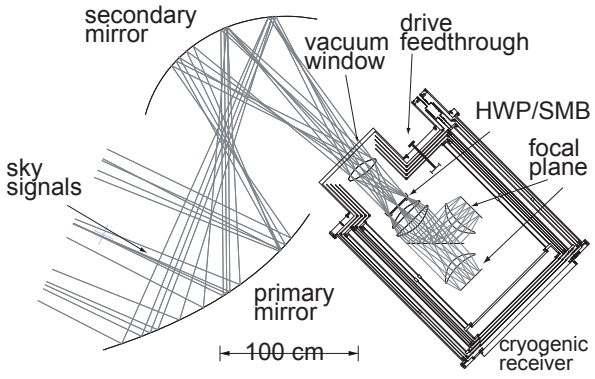

Figure 1.6: Cross-sectional view of the EBEX optical system. The HWP subsystem resides at 4 K, at the top of the cryostat, at an aperture stop in the optics.

EBEX underwent a 12-hour test flight from New Mexico in June 2009 and a 12-day (data taking time) science flight from McMurdo, Antarctica in December 2012 – January 2013. All calibration data discussed in this work was taken in Palestine, Texas in the summer of 2012.

1.3.3 Measuring polarization with EBEX

EBEX's detectors measure incident power only. Polarization is measured with a continuously-rotating Half-Wave Plate (HWP) and fixed lithographed 40 cm polarizing grid; this technique is novel to mm-wave polarimetry and its implementation and calibration will be the main focus of this work. We choose this method because constant rotation moves the signal to a known frequency above our detectors' $1/f$ noise (we give a mathematical treatment of HWP polarization in section 3.1.2).

The HWP rotation subsystem that allows for polarimetry is affixed inside the 4 K stage (Figure 1.6) at the top with the window oriented up (it is not part of the removable "instrument" assembly shown in Figure 1.4, all of which operates at < 1 K.) The 4 K placement of the HWP system is sufficient to minimize thermal emission while preventing direct conductive loading of the fridges, the hold time of which are an important driver of total cryogenic hold time. Its placement is at an aperture stop in EBEX's optical system.

Chapter 2

A SMB for HWP polarimetry

2.1 Choice of an SMB

We developed a cryogenic rotating half-wave plate (HWP) for EBEX.

In balloon-borne CMB telescopes emissive optical elements must be cooled to cryogenic temperatures so that the radiation they emit is not a dominant part of the total optical load on the detector. For example, at a temperature of 28 K thermal emission from the EBEX 24 cm diameter HWP[1] would be equivalent to the power from the CMB. Therefore the HWP in the EBEX receiver is mounted at the liquid helium cooled stage.

Continuous HWP rotation on a Long Duration Balloon (LDB) flight requires reliable, remotely controlled operation for about two weeks. At the targeted rotation speed of 2 Hz the rotation mechanism should produce less than ∼25 mW of power on the EBEX liquid helium stage to ensure that cryogens do not run out in a 12 day flight. The system must operate at tilt angles of up to 60° and withstand periods of strong acceleration of up to 10g, primarily during flight termination. We find an open-aperture ball bearing is predicted to dissipate as much as 1 W in our configuration. For this reason, we turn to Superconducting Magnetic Bearing (SMB) technology to achieve low-power rotation.

2.1.1 Introduction to SMBs

A Superconducting Magnetic Bearing (SMB) is a specialized type of magnetic bearing that uses the combination of a Type-II superconductor and a permanent magnet to create a levitation gap between a stator and a rotor. While any superconductor will act as a magnetic "mirror", repelling a magnet placed near it, Type-II superconductors also exhibit flux pinning behavior

[1] More information about the construction of the HWP is available in Hanany et. al. (2005)[11]

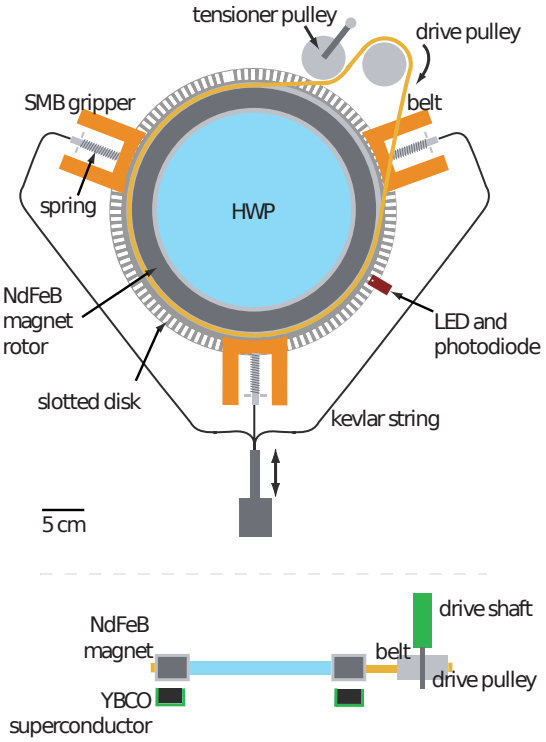

Figure 2.1: Top view (upper panel) and side view (lower panel) sketches of the SMB system. The HWP is rotated by a pulley system coupled to an external motor. Three spring-loaded grippers support the rotor at temperatures above ∼80 K.

that allows for stable levitation; a magnet held near such a superconductor while it is cooled through its transition will see both its reflection and a trapped image. Azimuthally symmetric geometry allows for rotation.

While SMB experimentation has occurred since the 1940s ([12]), it has become more common since the introduction of high-temperature superconductors with transition temperatures greater than liquid nitrogen such as YBCO. A common research application is SMB flywheels ([13]).

2.1.2 Overview of previous SMB for HWP polarimetry work

Hanany et al. (2003) [14] proposed using a SMB for continuous rotation of a HWP. They discussed requirements for such a system and constructed and demonstrated a prototype system. Subsequent papers [15, 16] presented characterization of coefficient of friction, vibrational amplitudes, resonant frequencies, and sources of power dissipation. The novelty of this system is twofold: first, the implementation at 4 K instead of the more typical 77 K, and second, the use of open-aperture geometry necessary for HWP polarimetry. They find bearing performance is largely independent of temperature, though there is a small reduction in the COF at 4 K. The successful implementation of this small prototype system suggested a larger system might be viable for EBEX.

2.2 Design of EBEX HWP/SMB installation

The SMB consists of a NdFeB ring permanent magnet rotor that is levitating relative to a stator made of a ring of superconducting YBCO; see Figure 2.1. (Both magnet and superconductor were made by Adelwitz Technologiezentrum GmbH). The magnet, which is 28.4 cm ID, 31.6 cm OD, and 1.6 cm in height, is made of two layers with 8 sections each. At 0.5 cm above the surface of the magnet, the mean field is 2.1 kG with variations of 4% around the magnet azimuthally. The HWP is mounted inside the ring magnet. The overall mass of the rotor, including HWP, magnet, and frame is 5.6 kg. At temperatures above $\sim$80 K the rotor is held above the superconductor by a warm support mechanism consisting of three linear motion grippers made of copper. Each gripper is mounted on two linear circulating ball bearing stages and is pushed forward into the rotor by a spring. A cryogenic mechanical linear actuator is used to move all the grippers simultaneously away from the rotor via a Kevlar string and several pulleys (Figure 2.1). Two grippers are connected with heat straps to the 4 K stage to cool the significant thermal mass of the rotor. The third is thermally isolated and is used to occasionally measure the temperature of the rotor upon re-gripping. The position of these grippers is encoded with linear potentiometers.

The rotor is driven with a belt made of 2.5 cm wide Kevlar tape (Figure 2.1). This approach avoids possible magnetic interference with bolometers from an electro-magnetic drive. The

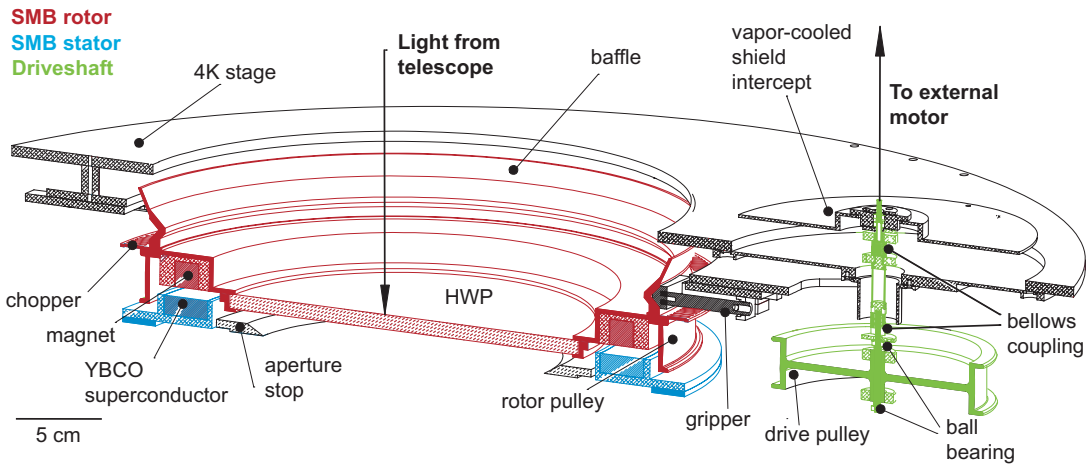

Figure 2.2: A cutaway model showing the implementation of the SMB in the EBEX receiver with color coding for the different functional elements. The drive pulley and shaft are shown in green, rotating elements — the SMB magnet, HWP, holder, and baffle — in red, and the SMB stator — the YBCO superconductor tiles and holder — in blue.

belt is connected to a pulley that is driven by a shaft extended to the outside of the receiver (Figure 2.2). The shaft is rotated with a DC brushless motor. Inside the receiver the drive shaft is coupled to a helium vapor-cooled shield and to the liquid helium stage using two extra-clearance, molybdenum disulfide dry lubricated ball bearings of 0.79 cm OD. A tensioner pulley that is mounted with the same type of bearings is used to maintain belt tension. These bearings provide over 30 million rotations, sufficient for an EBEX LD flight, with no evidence of failure, and are discussed in detail in section 2.4.

The rotor has a baffle to block external radiation from entering the HWP and to help radiatively cool the rotor. All available surfaces are coated with a mm/sub-mm wave emissive coating to maximize radiative coupling to 4 K[17].

2.3 Electronics interface

The HWP subsystem has its wiring run out of the cryostat at the top due to assembly constraints. The wiring, as well as the wiring to the DC motor, runs to a VME crate dedicated to HWP subsystem electronics (Figure 2.3). Temperature sensors are routed through to a housekeeping board residing in the "power" crate ([34]). Two redundant photodiode signals from the encoding system (discussed in section 2.5.1) run to two McGill dfMUX boards on a half backplane in the crate; those boards communicate with the rest of the readout system and flight computer via ethernet. A series of AllMotion stepper motor controllers operates the warm support mechanism

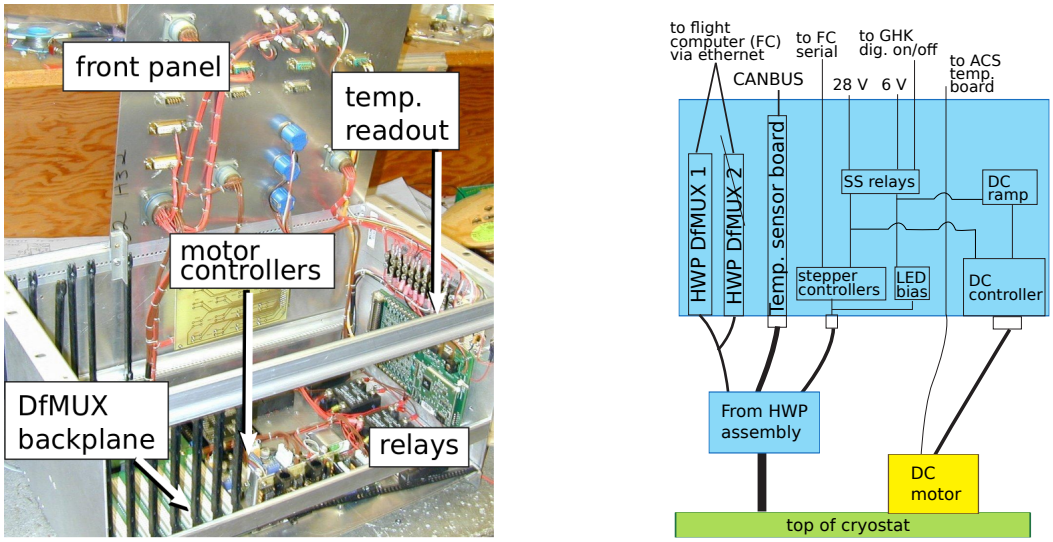

Figure 2.3: Left: photograph of HWP control electronics crate. Right: Schematic of HWP control electronics

and is controlled via serial connection to the flight computers. A Maxon EC-max 30 DC motor controller controls the Maxon 251601 Flat 8-pole motor that drives the HWP mechanism from the outside. Analog circuits control the amount of bias for the LEDs and are not adjustable during flight. On/off of all components are controlled with Crydom D1D07 solid state relays, which are switched via the housekeeping board (GHK) in the power crate ([34]) and are fully commandable in flight.

2.4 Ball Bearings

2.4.1 Introduction

The design of our SMB rotation mechanism (section 2.2) requires four small ball bearings that operate without failure for at least ~ 5 million rotations, dissipating on the order of 5 mW of power or less.

Various instruments have used miniature ball bearings to allow mechanical motion at cryogenic temperatures. Such applications are particularly common in infrared and microwave astronomy. The use of dry lubricants such as MoS_2 is typical of these applications, as is stepped motion with very low duty cycles [21, 22, 23]. At liquid helium temperatures when continuous rotation is desired, torque performance is essential to minimizing power loads on cryogenically cooled stages. Further, long bearing lifetimes are necessary.

While tests have been done of continuously rotating bearings at cryogenic temperatures [24], most have focused on larger bearings of 20mm bore or greater fitted with PTFE transfer film cages that are not available on bearings of miniature sizes. Gould, Roberts and Anderson [25, 26] tested 20mm bore bearings with PTFE transfer film, lead, and MoS_2 dry lubrication for 3 million rotations with a preload of 38 N. In their tests, all bearings showed modest increases in torque over the course of testing, and the authors observed that the MoS_2 lubricant was worn away on post-testing inspection.

We perform tests to compare the torque performance at cryogenic and room temperatures of specially prepared MoS_2 coated bearings before and after undergoing 30 million or 90 million rotations in a 4 K vacuum environment, and compare them to uncoated bearings.

2.4.2 Test Setup

All ball bearings are Pacamor-Kubar model SR2-5 K8-11 with 1/8" ID and 5/16" OD. All bearings have balls, races, and cages all made of 440C stainless steel. Extra large clearances of .0008"-.0011" are used to allow for MoS_2 coating. For coated bearings, the coating process is done separately by Donwell, Inc, and the bearings are then assembled by Pacamor. Races are coated to .0002" ($\sim$ 5 micron) and cages to .0003" - .0005" ($\sim$ 10 micron). Uncoated bearings are geometrically identical but are delivered assembled and without any lubrication by Pacamor.

We took torque measurements using a liquid nitrogen cryostat at temperatures of 80 – 110 K. We made measurements using a "spin-down" technique, in which two identical bearings support a rotor with an inertia I which takes on known values from 3.32 to 4.72×10^{-5} kg-m^2 due to minor changes in the rotor setup between test runs. The rotor has a disc with slots used to encode its speed optically with a laser diode and photo diode combination. The rotor is "kicked" with a half gear, and from its subsequent speed vs. time profile, bearing torque is determined. This assembly is shown in Figure 2.4.

We used two different mounting brackets for testing. Using a 440C stainless steel frame is natural to prevent differential thermal contraction; a slip fit clearance hole was used to allow small movement of the bearing while cooling occurred. We also used a bracket of identical geometry made from 6061 aluminum. The use of aluminum was considered due to some advantages for our application, such as better thermal conduction and lack of ferromagnetic properties. To account for differential thermal contraction, the clearance hold in the aluminum was oversized by 0.0005".

The frames were machined from a single piece of material to allow the best possible alignment between the two holes. We used a wave washer to establish a small preload of less than 1 N. We used a mechanical heat switch to ensure cooling of the bearing rotor, which is otherwise weakly thermally linked to the 77 K stage. We also make use of a radiation shield to prevent ambient

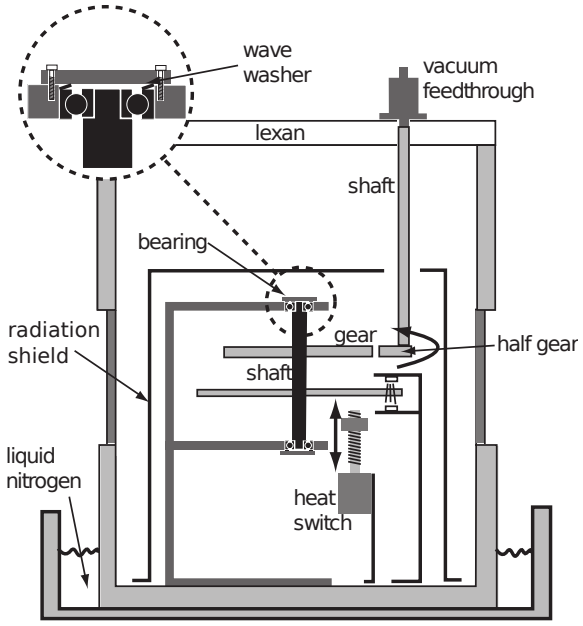

Figure 2.4: Test setup for bearing torque performance measurements.

300 K radiation from warming the rotor.

We ran a cooling calibration test with temperature sensors on the rotor and stator (Figure 2.5). We allowed three hours of cooling time minimum for subsequent runs, putting the stator at 80 K and the rotor at 110 K during bearing testing based on this calibration. During the calibration run, we opened the heat switch and monitored the temperature. We did not observe a significant change in rotor temperature during the amount of time necessary to complete our spin-down tests.

2.4.3 Results

We show typical spin-down curves in Figure 2.6. We make a linear fit to the spin-down data. In this case, the torque τ is then

$$\tau = I\frac{d\omega}{dt} \tag{2.1}$$

where I is the known rotor inertia and $\frac{d\omega}{dt}$ is the slope of the fit.

The tests were repeated with two sets of bearings for each MoS_2 coated and completely uncoated bearings, as well as two sets of MoS_2 bearings that had rotated more than 30 million and 90 million rotations at 4 K at 200 rpm respectively prior to these torque measurements. These bearings underwent this life test in the aluminum mounting bracket. The results are summarized in Tables 2.1 and 2.2. Numbers shown are the average between three and six

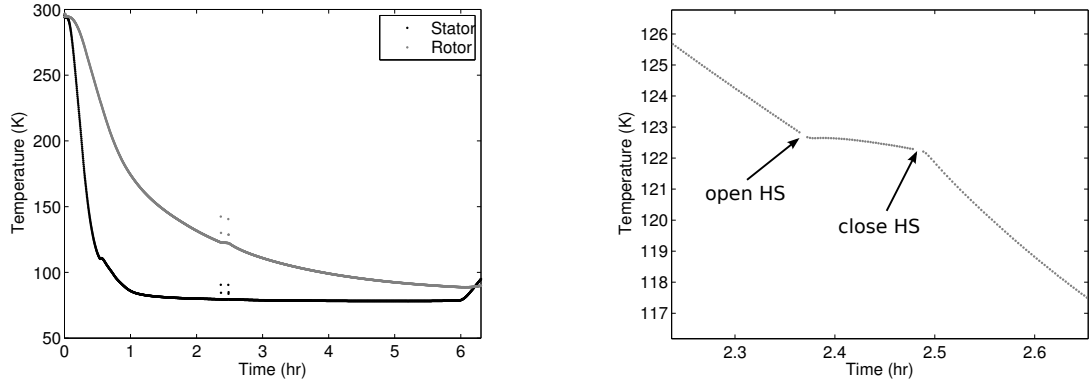

Figure 2.5: Left: Cool-down calibration of rotor and stator of test setup. Right: Zoom on test of opening heat switch

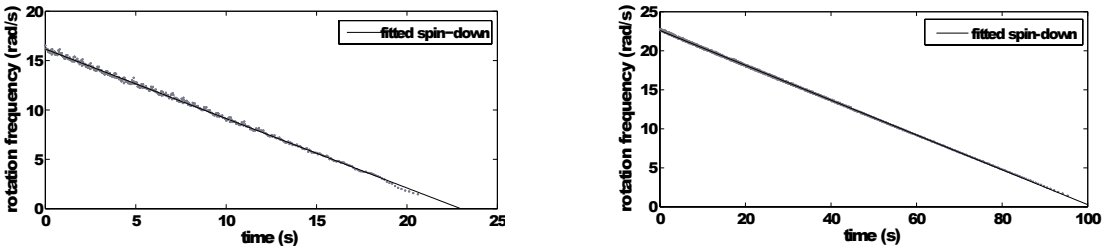

Figure 2.6: MoS_2 Spin-down curve at 77K (left) and 300K (right).

Bearing	Torque ($Nm \times 10^6$)
MoS_2 bearings A, 300K	12.20 ± 1.10
MoS_2 bearings A, 77K	22.20 ± 2.00
MoS_2 bearings B, 300K	7.10 ± 0.40
MoS_2 bearings B, 77K	10.50 ± 2.70
MoS_2 used bearings 30M, 300K	2.60 ± 0.40
MoS_2 used bearings 30M, 77K	14.20 ± 3.30
MoS_2 used bearings 90M, 300K	6.27 ± 3.60
MoS_2 used bearings 90M, 77K	8.00 ± 2.00
Plain bearings A, 300K	1.20 ± 0.02
Plain bearings A, 77K	4.20 ± 0.10
Plain bearings B, 300K	1.50 ± 0.01
Plain bearings B, 77K	10.20 ± 3.40

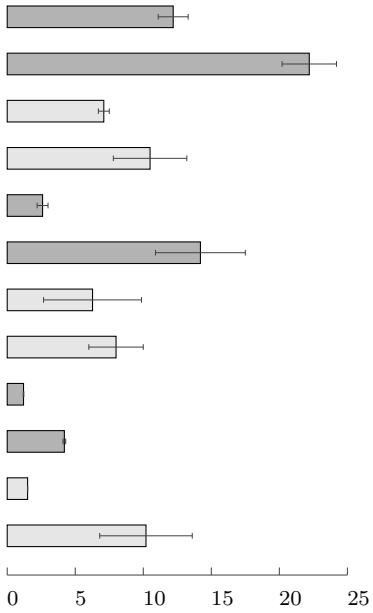

Table 2.1: Torque performance in a SST bracket setup.

spin-downs, and error bars are one standard deviation of these measurements.

2.4.4 Discussion

The aluminum bracket measurements show very large torque discrepancies between room and cryogenic temperatures. Because all thermal contraction differentials were properly accounted for to the best of our knowledge, we do not fully understand these discrepancies. We speculate that stresses in the material may have caused slight changes in geometry during thermal contraction. It is notable that bearings that underwent lifetime tests did so in what appears to have been a less than ideal setup.

When using the SST bracket, a MoS_2 coated bearing shows an increase in bearing torque of a factor of 2–4 over an unlubricated bearing. We understand this to be a trade-off for the relatively long bearing life span provided by the coating, given that plain unlubricated bearings have been shown to fail in less than 100,000 revolutions [26].

Cryogenic operation also contributes a small increase in friction of a factor of 1.5–5 over room-temperature operation. We posit that this is likely due to small changes in the geometry of the mount or bearings themselves during the cooling process.

Used bearings actually show a small decrease in torque compared to new bearings. We

Bearing	Torque ($Nm \times 10^6$)
MoS_2 bearings A, 300K	35.00 ± 5.30
MoS_2 bearings A, 77K	510.00 ± 100.00
MoS_2 bearings B, 300K	7.40 ± 0.20
MoS_2 bearings B, 77K	32.00 ± 0.50
MoS_2 used bearings 30M, 300K	3.10 ± 0.05
MoS_2 used bearings 30M, 77K	95.00 ± 9.50
MoS_2 used bearings 90M, 300K	6.90 ± 0.70
MoS_2 used bearings 90M, 77K	210.00 ± 21.30
Plain bearings A, 300K	18.00
Plain bearings A, 77K	100.00 ± 19.40
Plain bearings B, 300K	1.40 ± 0.08
Plain bearings B, 77K	3.10 ± 0.40

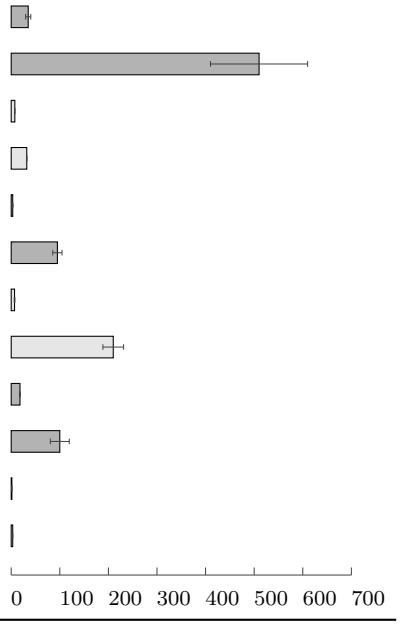

Table 2.2: Torque performance in an aluminum bracket setup.

interpret this as the bearings still being in operating condition after the 4 K endurance test. We attribute this long lifetime to the ~ 10 micron thickness of the MoS_2 coating allowed by oversized clearances, and the very light preload of < 1 N our application required. By contrast, Gould and Roberts [26] applied only about 1 micron coatings and were using a considerably higher load of 38 N in the case where they described their MoS_2 as having worn off. The decrease in torque we attribute to the used bearings having undergone a "break-in" period where the freshly applied lubricant was smoothed out.

We conclude that the prescribed process for preparing and installing these instrumentation bearings allows cryogenic in-vacuo operation for continuous rotation of at least 90 million rotations without degradation in bearing performance. We use bearings of this prescription in the SMB rotation mechanism.

2.5 Angular Encoding

2.5.1 Angular encoding system and electronic readout

Polarimetry depends on angular position encoding of the HWP. To achieve its science goals the EBEX angular position reconstruction should be accurate to better than 0.3°. We encode the

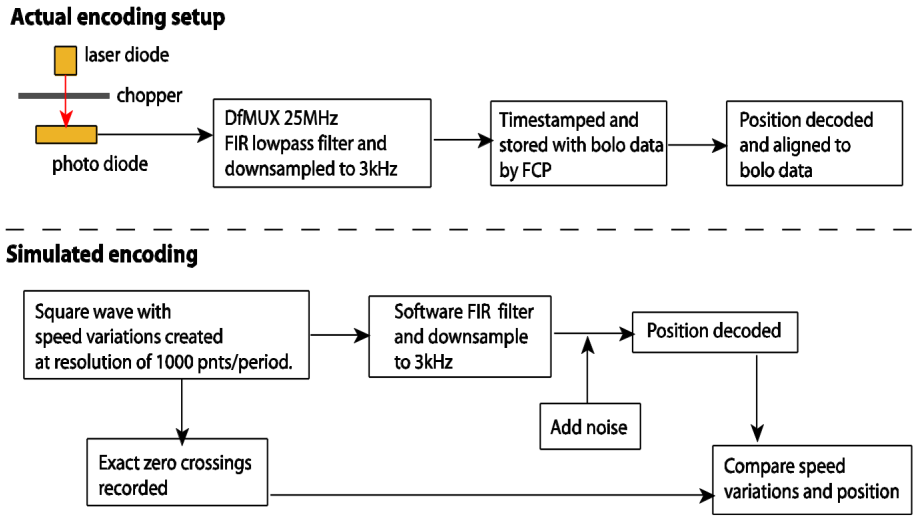

Figure 2.7: Encoding and simulating the encoding of the HWP

position of the HWP at all times using an optical encoder consisting of an LED, a photo diode, and a chopper ring at the outside edge of the SMB rotor assembly that holds the HWP (Figure 2.7). We find through 77 K and 4 K trial runs of LEDs and photo diodes that a Cree 5-mm Round LED C503C-WAS/WAN and a Centronic OSD5-5T perform reliably at 4 K. We initially chose a laser diode, since the more focused light would theoretically allow more efficient use of power. However, we find that despite the LED's nominal operating power of 64 mW, we see a clear signal on the photo diode of 195 mV at only 1 mW of power dissipation; further, the LED becomes considerably more efficient at 4 K, giving us a clear signal from the photo diode at a power dissipation of only $\sim 40\mu W$. We voltage bias the LED; the 4 V voltage bias necessary is higher than nominal at 4 K. It is essential to fully heat sink the LED to achieve this lower power dissipation; otherwise, it can warm up and then takes increasingly higher bias voltages to produce a signal.

We run the leads of the photo diode directly into the inputs of the same McGill DfMUX readout boards we use for bolometers. Minor modifications to the hardware – the removal of a capacitor to allow for low-frequency input signals – and to the firmware allow us to use the boards to measure this voltage, time stamp it in the same manner as the bolometer data, and sent out packets to be collected by FCP along with bolometer data.

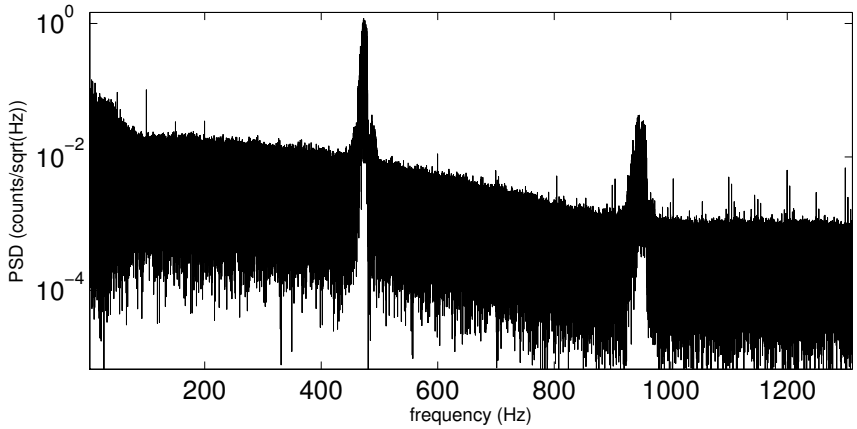

Figure 2.8: The spectrum of raw HWP data at 2 Hz rotation speed

2.5.2 Angular reconstruction process

The DfMUX boards set aside for HWP use each produce their own binary file of data, along with a set of binary files that encodes the EBEX time for each data point. This same timebase is used for the bolometer system and the attitude control system, and the timing is absolute modulo an offset of ~ 11 ms due to differences in board firmware versions and on-board digital filters. The file simply contains counts representing the voltage read out from the photo diode; counts are low when light from the LED strikes the diode and high when they are blocked. While the dfMUX boards sample all data at 25 MHz, the data is downsampled and digitally filtered such that data is written to disk at a frequency f_{sample} =3050 Hz, a number that is chosen as compromise between encoding accuracy and a combination of disk space and network and flight computer throughput. This raw data stream is useless as an ingredient for further data analysis since it says nothing on its surface about the angle of the HWP at any given time.

A software pipeline is used to convert this raw HWP data into a usable HWP angle as a function of time data set.

Figure 2.8 shows the spectrum of this raw HWP data before any angle reconstruction is performed. The peak at 480 Hz is the consequence of the 2 Hz rotation of a chopper wheel with 240 slots. At this speed there are about 6–7 data points for every chopper wheel slot. One slot is double-wide to provide an absolute reference every rotation. Sampling above the Nyquist frequency allows for a simpler and faster angle reconstruction process. The reconstruction process starts with the identification of the main peak. This nominal speed is used to determine where double-slot passes exist and identify data that may have an error such as a dropped packet. It is assumed that there are no large changes in absolute rotation speed during any

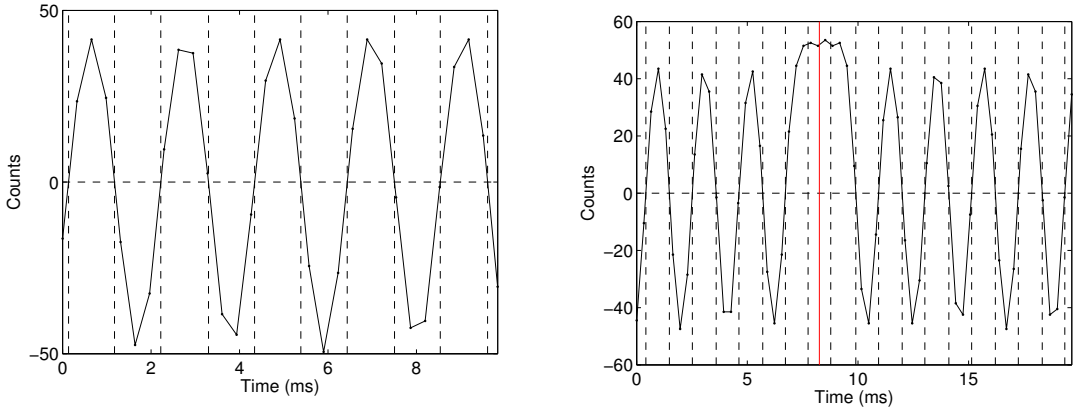

Figure 2.9: Left: using "zero-crossings" to determine HWP rotation angle. Right: a double-blanked slot indicates absolute zero.

given scan. The width of the peak does represent small variations in rotation speed, discussed in more detail in section 2.6.4.

We subtract the overall mean from the entire data set. Each slot-crossing time is found by iterating through the data, taking note of points where the value of the readout passes, and then linearly finding where the line between the two points bookending the slot-crossing passes the value zero (Figure 2.9, left). When a double-blanked slot is found, its center indicates the absolute reference for the HWP rotation angle $\theta_{HWP} = 0°$, indicated here by the red line in Figure 2.9. The other zero-crossings are shifted accordingly. This center is physically measured and referenced to the HWP itself, so it can be used for absolute calibration later.

What is generated, then, is a list of angles from 0° to 359.25° in 0.75° increments and their respective absolute EBEX timestamps, for each full HWP rotation, fifteen seconds of which are plotted in Figure 2.10.

This data can be easily linearly interpolated onto the bolometer timebase. Optionally, the result can be written to a dirfile for use later. It is then possible to proceed with any manner of data analysis where it is necessary to know the HWP rotation angle θ_{HWP} for each bolometer sample, in particular, any analysis of polarization.

2.5.3 Angular reconstruction accuracy

A software simulation can be used to determine the accuracy of the process described in the previous section (see Figure 2.7). A square wave is generated to mimic the signal produced by the HWP chopper wheel. The square wave can encode speed variations, which are added in the same amount as observed in short time periods (∼2 seconds) of physical HWP rotation. This

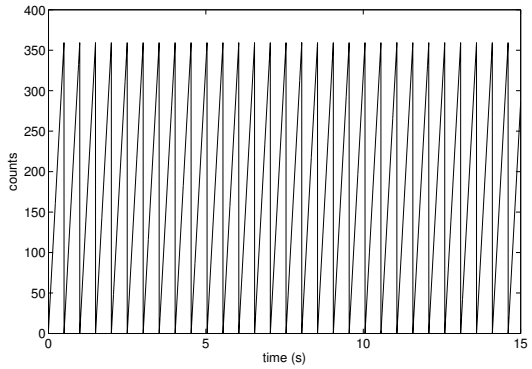

Figure 2.10: Fifteen seconds of HWP angle data.

signal is sampled at a frequency that is large compared to the frequency of the raw HWP time stream signal; a factor of 2000 above this frequency, or 2 MHz, is used. The exact edge locations in time of the generated square wave are recorded. A perfect reconstruction should return these times and their associated angles. The signal is then FIR filtered and downsampled to 3 kHz, following the processing done by the dfMUX boards to the actual optical signal. Noise is added at the same level as observed in the actual optical data. The resulting time stream is then run through the HWP reconstruction software, and the results are compared to the original edge locations and angles recorded earlier in the process.

The results of this analysis are shown in Figure 2.11. The top panel of Figure 2.11 shows the speed of HWP rotation shown over four full rotations (2 seconds). The speed profile that was created by the simulation is shown in green, and the speed profile recovered in black. The second panel shows the difference between the simulated angle and the recovered angle. The bottom panel is a histogram of this difference. The simulation includes the inherit error in the machining of the chopper wheel. The wheel is 14.3 in. diameter to the slot centers and was laser-cut to 0.002" precision. This error can be included in the simulation by modifying the width of each slot randomly, scaled to the appropriate error, and repeating it for each rotation. In this configuration, the angle was recovered to a standard deviation of 0.010°, significantly better than the EBEX target of 0.3°. It can be seen in the histogram in Figure 2.11 that the error is apparently not centered around zero. This is because there is a relatively large error of $\sim 0.1°$during the passing of the double-slot. This error represents only$\sim 0.6\%$ of the angle data and is still within our targets.

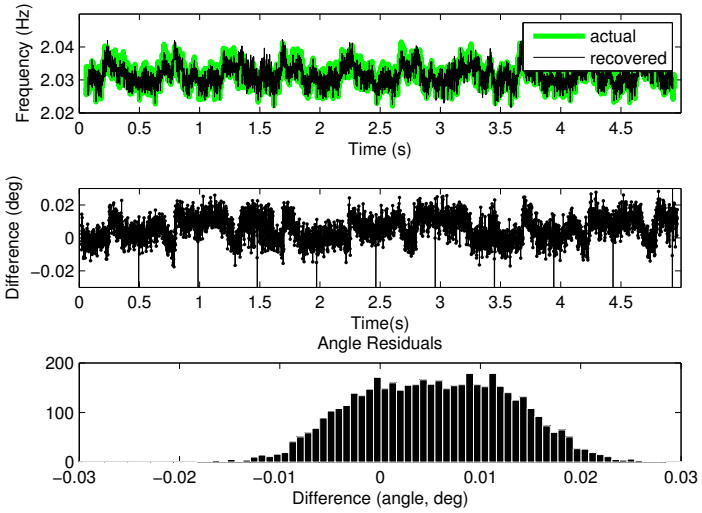

Figure 2.11: Recovery of HWP angle from simulation

2.6 SMB characterization and performance

2.6.1 HWP power dissipation and temperature

We measured total power dissipation by monitoring the steady state liquid helium boil-off of the EBEX cryostat. Since we are interested in measuring the dissipation due to the HWP rotation sub-system in isolation, we deconvolve the effect thermal feedback due to the EBEX cryostat's vapor-cooled shields by applying known amounts of power electrically; we find that a raw boiloff measurment produces a value of 74% of the power applied. We also measure a baseline value that is the boiloff with no rotations. With these values in mind, we rotate the HWP for several days at a time and measure the power dissipation (Figure 2.12).

We find that the dissipation is stable after 2 days of rotation. From this, we summarize total power dissipation as a function of HWP rotation speed (Figure 2.13).

We suggest the following model for the cryogenic circuit and for power flow and dissipation in the system. It is illustrated in Table 2.3 and in Figure 2.14. We separate the system to one element that consists of all the moving parts and another element that consists of the stationary parts. The moving parts include anything that moves and is inside of the helium vapor-cooled shield.

Assuming a weak conductive coupling of the moving parts to the helium stage and to higher temperature stages, power dissipation of the moving parts occurs primarily radiatively to the

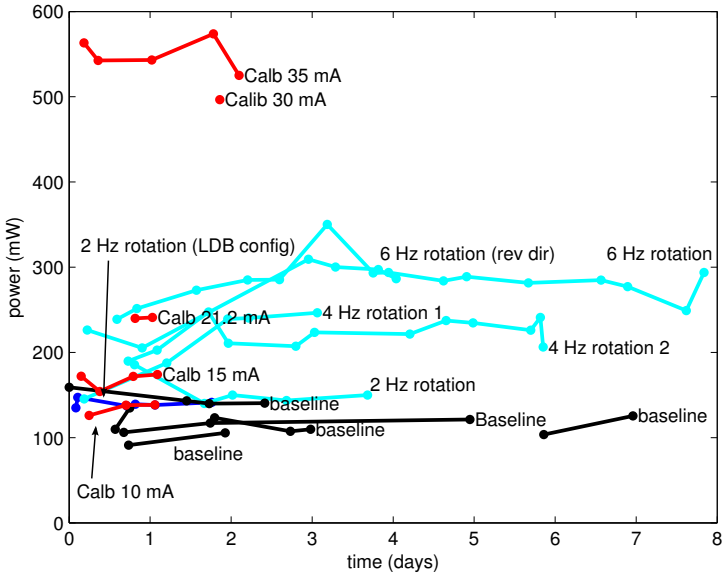

Figure 2.12: Raw power dissipation measurements from cryostat LHe boiloff. Baseline (no power applied) measurements are shown in black, calibration (electrical power applied) measurements in red, and rotation measurements in cyan..

Moving parts		**Stationary parts**	
Heat input	**Heat output**	**Heat input**	**Heat output**
• eddy currents • magnet hysteresis • belt friction • ball bearing friction • conductance from higher stages via shaft	• radiation • conductance via ball bearings through shaft to 4K stage • conductance via ball bearings through tension pulley to 4K stage	• eddy currents • super-conductor hysteresis • conduction and radiation from moving parts	• boiling liquid helium

Table 2.3: Summary of heat flows in the SMB system. Power dissipation from HWP rotation must eventually reach the EBEX cryostat 4 K liquid helium stage.

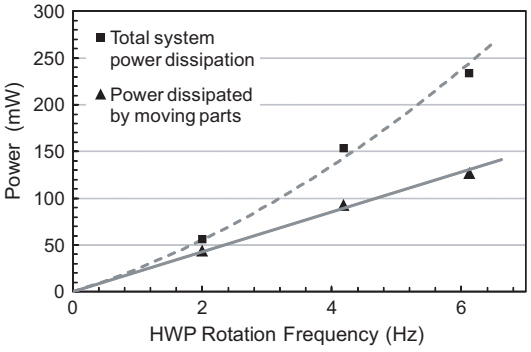

Figure 2.13: HWP system total power dissipation and power dissipation on the SMB's moving parts as estimated from the rotor's temperature shown in Figure 2.15. Typical error on total power dissipation is ∼4 mW. The fit to power dissipation in the moving parts is linear (solid line). Adding this fit to the quadratic fit applied to stator power dissipation, shown in Figure 2.16, gives the overall fit shown as a dashed line.

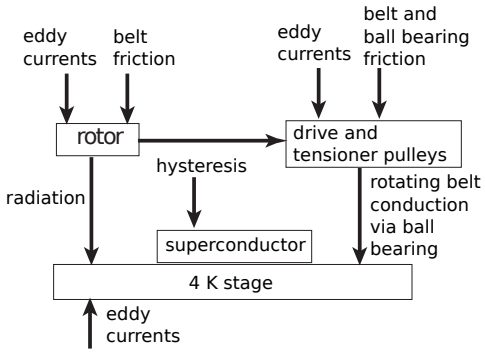

Figure 2.14: Cryogenic circuit of power dissipation in the rotating HWP system. Rotating elements are shown on top, stationary elements are shown on bottom. Arrows show power flows.

helium stage. We assume weak conductive coupling because conduction is facilitated through the point contacts of four stainless steel ball bearings and because power from shaft conductance is calculated from known material properties to be 2 mW, which is small compared to the radiated power, as we now show.

We estimate the radiative power dissipated from the moving parts by assuming that radiation is most dominant from the HWP. For rotations at or above 2 Hz the steady state temperature of the HWP is higher than 45 K (Figure 2.15)

At these temperatures the peak of the emission is in the IR, a wavelength band in which the emissivity of the 0.86 cm thick sapphire HWP is nearly 1[18]. The following measurement is used to infer the steady state temperature of the rotor. For each rotation speed f_{HWP} we let the temperatures in the system stabilize. This typically takes several days. We then stop the rotation, which takes less than 5 minutes, and monitor the temperature rise of the isolated gripper upon re-gripping. The peak temperature of the gripper is taken to be the stable temperature of the rotor during rotation.

With these assumptions we calculate that the power radiated from the moving parts is 44 mW at 2 Hz. The rotation speed dependence of the power on the moving parts is linear (solid line in Figure 2.13), consistent with mechanical friction. Subtracting this power from the total power

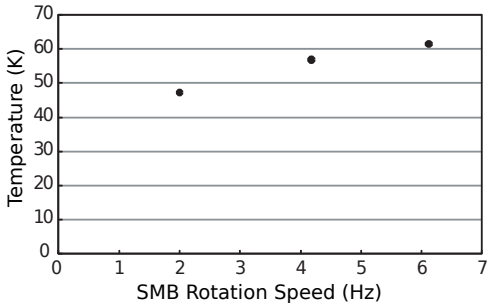

Figure 2.15: Peak temperature of the isolated gripper upon gripping the SMB rotor temperature after rotation at the frequency given by the horizontal axis. The peak temperature of the gripper is presumed to be an indicator of the temperature of the rotor.

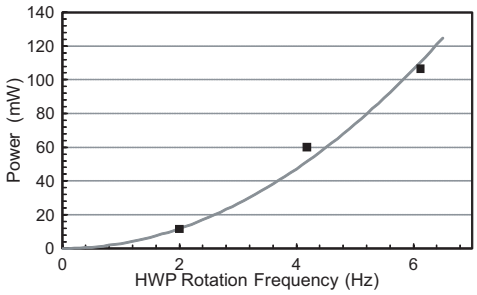

Figure 2.16: Power dissipated on the stationary parts. The fit is quadratic, matching the expected dependence of eddy current power dissipation on rotation speed.

dissipated in the system gives the power dissipated by the stationary sub-system and is shown in Figure 2.16. The observed dependence on rotation speed is quadratic suggesting that the source for the dissipation may be eddy currents[19]. The addition of the two fits is consistent with total power dissipation (dashed line in Figure 2.13).

Measurements of HWP power dissipation up to this point describe a configuration in which the warm support grippers were made from copper; this choice was made to maximize thermal conductivity. Geometry of these grippers was designed to minimize eddy current power dissipation; nonetheless we later switched to aluminum grippers in order to attempt to reduce power dissipation further. After switching to aluminum, we saw our 2 Hz power dissipation drop from 54 mW$\pm$ 13 mW to 30 mW$\pm$ 12 mW. We used this configuration for the EBEX Long Duration Balloon flight in 2012.

2.6.2 Vibrations and damping

Levitating bearings have associated resonance frequencies and time constants for axial and radial modes. Tests were performed to monitor the behavior of the SMB when exposed to vertical and axial driving forces with the bearing stationary. Bearing vibrations were measured with a Hall probe. Tests were done at 77 K with the bearing cooled by liquid nitrogen. A typical result is shown in Figure 2.17. The dependence of resonant frequency on levitation height is shown in Figure 2.18. The ratio between axial and radial modes is consistent with a simple SMB model[14] that predicts a value of $\sqrt{2}$. Vibration decay times were measured. Both axial and radial modes are observed simultaneously. For the approximate levitation heights of 0.32 cm, 0.63 cm, and

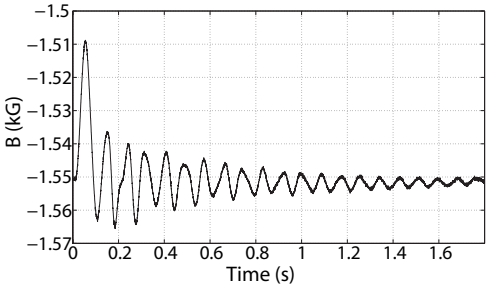

Figure 2.17: Typical profile for resonance and decay of the SMB after excitation by a radial shock. The measurement is done with a Hall sensor located near the SMB rotor. For this data the levitation height is 0.95 cm.

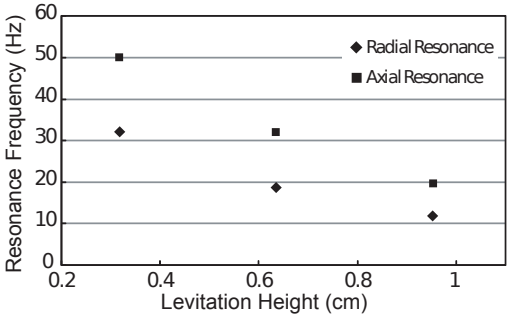

Figure 2.18: Measured axial and radial resonant frequencies as a function of rotor levitation height. Typical error is ∼1 Hz. Measurements made only once are shown without error bars.

0.95 cm, these radial vibrations decay in 0.16 ± 0.07 seconds, 0.11 ± 0.01 seconds, and 0.13 ± 0.04 seconds, respectively.

2.6.3 Detector magnetic interference

The EBEX detectors and SQUID amplifiers are sensitive to changing magnetic fields. The detectors and SQUIDs are at a distance of 65 cm and 110 cm from the HWP system, respectively. The SQUIDs are surrounded by a mu-metal shield. We searched for spurious signals induced on the data by the rotation of the SMB. Five minutes of data were binned by HWP rotation angle and compared to the noise level. The data was fit with a model that has dipole and quadrupole variation to capture a potential dependence on the largest magnetic field multipole moments. The fits have amplitudes of 3 and 1% of the noise level for the dipole and quadrupole moments, respectively, but are poor fits to the data. (A level of 3% of the noise is approximately 0.4 nAmp RMS.) The probability to exceed obtained from χ^2 tests is 2% and 1% , respectively, indicating that the data does not support these models. Our interpretation is that we are not detecting magnetic fields and that the fitted amplitudes are upper limits on the magnitude of possible pick-up.

2.6.4 Speed Variations

It is useful to investigate rotational speed variations to better understand the dynamics of the system and to constrain our errors on angular reconstruction (section 2.5.3). The RMS magnitude of rotational speed variations of the HWP system is 0.2% as calculated over the ∼10

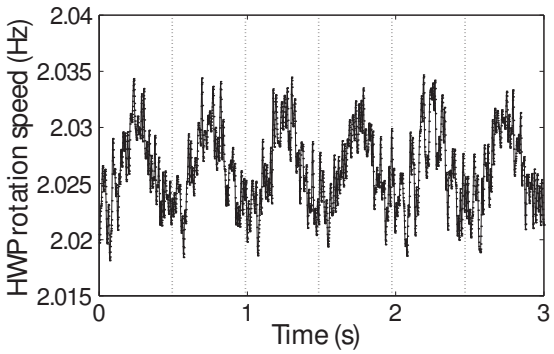

Figure 2.19: RMS speed variations are small, about 0.2%, but are most pronounced at the frequency of rotation. Dotted lines mark the start of each rotation. The variations are synchronous with HWP rotations, thus, it is thought that the variations are due to SMB angular asymmetry.

hour NA flight. The rotational speed variations occur at several frequencies. Ordered from larger to smaller, the largest contributors are variations that occur once, twice, and four times for each full SMB rotation (Figure 2.19). We hypothesize that the $1f$ speed variation, where f is the rotation frequency of the rotor, is due to the inhomogeneity of the magnetic field of the rotor. A typical ratio $1f : 2f : 4f$ for speed variations in a power spectrum of speed variation amplitude vs. frequency is 1:0.15:0.05.

2.6.5 Test Flight performance

EBEX was launched in a North American test flight in June 2009. Rotation of the SMB was continuous during the flight as shown in Figure 2.20. Failure of the telescope elevation actuator during launch led to angular accelerations of up to $\sim$220 deg/sec^2 of the receiver housing the HWP and SMB. The data show speed variations at a frequency of 13.5 Hz; see Figure 2.21. We interpret the data as radial vibrations in the rotor that appear as speed variations in angular encoding. Data presented in section 2.6.2 show that the 13.5 Hz frequency of speed variations is consistent with bench-top axial vibration measurements conducted at 0.64 cm levitation height, which is also the flight levitation height. For the laboratory bench top measurements the axial resonant frequency is 19.5 Hz because the mass of the rotor in this measurement was lower. The ratio 19.5/13.5 closely matches the square root of the ratio of rotor masses in flight and in the lab measurement.

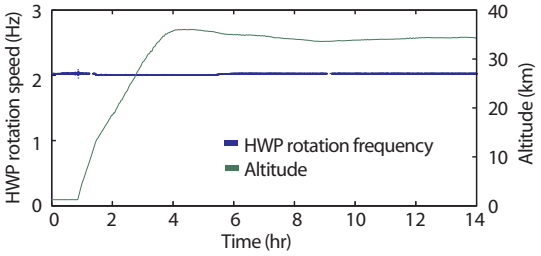

Figure 2.20: HWP rotation speed (left ordinate) and EBEX payload altitude above sea level (right ordinate) as a function of time during the North American flight of the payload. The zero offset in time is arbitrary. Rotation of the HWP was started about an hour before launch, and rotation continued through launch and the ∼10 hours flight. Gaps in the rotation data correspond to lost data, not to breaks in rotation. The RMS speed variation throughout the flight is 0.2%.

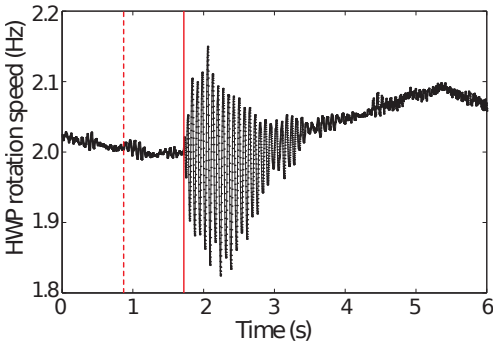

Figure 2.21: An elevation actuator failure (solid line) that took place shortly after launch (dashed line), caused the receiver to undergo a strong angular acceleration of ∼220 deg/sec^2. Despite the shock, the rotor continued to turn. We interpret the observed speed variations as arising from rotor vibrations that affected the angular encoding. The launch and failure times are determined using on board speed gyroscope information, not from the SMB data.

2.6.6 Long Duration Balloon flight performance

We lowered the rotation speed of the HWP to 1.23 Hz for LDB to account for detector time constants. The HWP performed as designed throughout the long duration flight, accruing 6.1 days of total rotation time (∼ 650000 HWP rotations), and being stopped and started (but not gripped) nine times during flight. Hold time observed during flight was consistent with a 15 mW load derived from the data and model in section 2.6.1; this load represented about 5 % of the total cryogen boiloff [34].

A failure occurred immediately before the end of observation, from an unexpected elevation slew from highest to lowest elevation. Based on our knowledge of the HWP rotation system, we posit that the drive belt slipped off the pulleys. At low elevations the tensioner gets progressively loser, due to the fact that the tensioner sits below the HWP in its LDB configuration. This did not affect our observations; however, we suggest a design change to move the pulley to the top side of the HWP. In this configuration, the tension will get tighter as the elevation goes down.

Chapter 3

Analysis of polarization calibration

3.1 An analytic overview of HWP polarimetry

3.1.1 Introduction to single-HWP polarimetry

In order to develop a data analysis process for calibration of the EBEX instrument, it is first necessary to understand mathematical formalism behind HWP polarimetry. HWP polarimetry has been used in optical and infrared astrophysical instruments and a description is available in several textbooks [29, 28, 28, 30]. Formalism used here is adopted from Matsumra 2009 [27], which also contains a more complete treatment of the HWP for the specific case of EBEX. EBEX makes use of a stack of five HWPs in order to create a broadband instrument. In contrast to a single HWP, a 5-stack will have frequency dependent effects in modulation efficiency and output polarization phase angle [27]; we discuss models and measurements of this effect in section 3.7. However, the focus here is to develop a set of steps to extract the polarization measured during various calibration tests of EBEX, and for this, single-HWP polarimetry suffices.

The polarimeter component of EBEX consists of a rotating HWP 5-stack, here modeled as a single HWP, and a linear polarizing grid. The HWP is rotated a fixed frequency f_{HWP}, and at any given time is at some angle $\rho(t)$. The actual HWP has some small variations in its rotation frequency, detailed in section 2.6.4. For this discussion its rotation speed will be assumed to be constant, as the mathematical formalism is unchanged in the case where the rotation angle is known. Incident light from some source is coupled to the instrument by the warm and cold optics (section 1.3.2), and passes first through the HWP and then through the grid before being

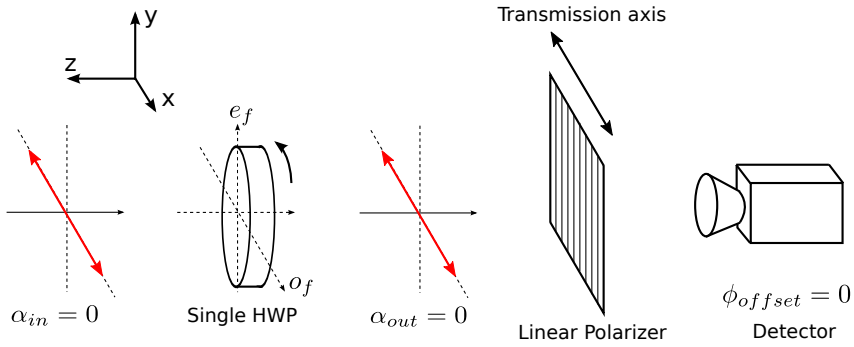

Figure 3.1: A schematic model of a single-HWP system (Figure adapted from [27]).

focused on power detecting TES bolometers. Each bolometer forms an independent polarimeter in concert with the polarizer and HWP, and a DC polarized source will appear in the bolometer time streams at a frequency of $4 \times f_{HWP}$.

3.1.2 Single HWP polarimetry in the time or angle domain with a chopped source

Mueller matrices are used to describe the optical elements and stokes vectors the signal. Axes are defined such that rotation occurs around the z-axis where angles increase in the counter-clockwise direction starting from the x-axis (Figure 3.1). The x-axis is also the transmission axis of the grid, and $\rho = 0$ when the ordinary axis of the single HWP is aligned with the x-axis of the coordinate system. The vector entering the single HWP polarimetry system can be written as

$$\vec{S} = \begin{bmatrix} I \\ Q \\ U \\ V \end{bmatrix} = GR(-\rho)\Gamma R(\rho)\vec{S}_{in}(\alpha_{in}, \beta_{in}, P_{in}) = I_{in} \begin{bmatrix} 1 \\ P_{in}\cos 2\alpha \cos 2\beta \\ P_{in}\sin 2\alpha \cos 2\beta \\ P_{in}\sin 2\beta \end{bmatrix}. \tag{3.1}$$

We also define

$$I_p = \sqrt{Q^2 + U^2} = I_{in}P_{in} \tag{3.2}$$

for the case where $V = 0$. A HWP is a combination of a rotation, represented by R, and a retarder, represented by Γ. The input signal to the system $\vec{S}$ is a function of the input polarization angle α_{in}, the amount of input power I_0, the polarization fraction P_{in}, and ellipticity β. Input light is assumed to be linearly, not circularly, polarized. The components of the Mueller

matrices are:

$$R(\rho) = \begin{bmatrix} 1 & 0 & 0 & 0 \\ 0 & \cos\rho & -sin\rho & 0 \\ 0 & \sin\rho & \cos\rho & 0 \\ 0 & 0 & 0 & 1 \end{bmatrix} \tag{3.3}$$

$$G_x = \begin{bmatrix} 1 & 1 & 0 & 0 \\ 1 & 1 & 0 & 0 \\ 0 & 0 & 0 & 0 \\ 0 & 0 & 0 & 0 \end{bmatrix} \tag{3.4}$$

$$\Gamma(\Delta\delta) = \begin{bmatrix} 1 & 0 & 0 & 0 \\ 0 & 1 & 0 & 0 \\ 0 & 0 & \cos\Delta\delta & \sin\Delta\delta \\ 0 & 0 & \sin\Delta\delta & \cos\Delta\delta \end{bmatrix} \tag{3.5}$$

The retarder is a function of a phase delay $\Delta\delta$ where $\Delta\delta = \pi$ for ideal single wave plate polarimetry. Given that EBEX bolometers detect only power, the output intensity I_{out} is then (equation 3.29 from [27])

$$I_{out} = G_x R(-\rho)\Gamma(\Delta\delta)R(\rho)\vec{S}_{in} \tag{3.6}$$

$$I_{out} = \frac{I_{in}}{2}(1 + P_{in}\cos(2\alpha_{in})\cos(2\beta_{in})\cos^2(\frac{\Delta\delta}{2}) + P_{in}\cos(2\alpha_{in})\cos(2\beta_{in})\sin^2(\frac{\Delta\delta}{2})\cos 4\rho + P_{in}\sin(2\alpha_{in})\cos(2\beta_{in})\sin^2(\frac{\Delta\delta}{2})\sin 4\rho - P_{in}\sin(2\beta_{in})\sin(\Delta\delta)\sin(2\rho)) \tag{3.7}$$

For the purposes of understanding how to extract polarization from calibration data, some simplifying assumptions will be made here. The ellipticity β is assumed to be 0. Then equation 3.7 simplifies to:

$$I_{out} = \frac{I_{in}}{2}(1 + P_{in}(\cos(2\alpha_{in})\cos(4\rho) + \sin(2\alpha_{in})\sin(4\rho)) \quad (3.8)$$

$$I_{out} = \frac{I_{in}}{2}(1 + P_{in}\cos(4\omega_{HWP}t - 2\alpha_{in})) \quad (3.9)$$

It is also important to bear in mind that α_{in} may be a slowly-varying function of time (with respect to the HWP frequency), since it is possible in some calibration tests for the gondola to move or for instrumental effects to produce small variations in the detected α_{in} over the beam. It will also become apparent that the effects of detector noise will manifest themselves as a varying α_{in}. It is only necessary for the physical variations in α_{in} to occur on time scales slower than f_{HWP} and f_{chop} for the following analysis to apply.

During all calibration tests, a chopped source was used. While several different mechanisms were implemented, we approximate all of them by a sine wave that chops from "off" to "on".

$$I_{in}(t) = \frac{I_0}{2}(1 + \cos(\omega_{chop}t)) \quad (3.10)$$

Substituting this this chopped signal for I_{in} and expanding gives:

$$I_{out}(t) = \frac{I_0}{2}(\frac{1}{2} + \frac{1}{2}\cos(\omega_{chop}t) + \frac{P_{in}}{2}\cos(4\omega_{HWP}t - 2\alpha_{in}) + \frac{P_{in}}{4}\cos(\omega_{chop}t - 4\omega_{HWP}t + 2\alpha_{in}) + \frac{P_{in}}{4}\cos(\omega_{chop}t + 4\omega_{HWP}t - 2\alpha_{in})) \quad (3.11)$$

These terms, shown in the frequency domain in Figure 3.5, have the following physical interpretations respectively:

1. This term is a DC offset proportional to the power of the source.
2. This term contains no information about the polarization angle, but can be used to extract the exact chop frequency.
3. This $4f$ term encodes information about polarization angle of the chopped source in addition to any DC polarized light observed by the instrument
4. This lower sideband of $4f$ encodes the polarization angle.
5. This higher sideband of $4f$ encodes the polarization angle and is additional signal that can be combined with (3). However, in practice it is often attenuated by the optical time constant of the detector. This time constant effect is discussed in detail in section 3.3.

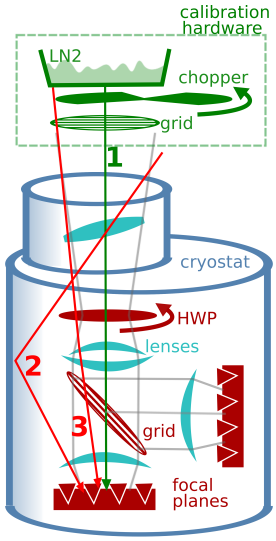

Figure 3.2: Schematic of EBEX cryostat (blue) with optics (red, cyan) and a chopped calibration setup (green). We show various light paths that cause systematic effects.

It is worth noting here that equation 3.11 is only applicable if $\omega_{chop} > 4\omega_{HWP}$. In the other case where $\omega_{chop} < 4\omega_{HWP}$, the lower side band term in the equation becomes

$$\frac{P_{in}}{8}\cos(4\omega_{HWP}t - \omega_{chop}t - 2\alpha_{in}). \tag{3.12}$$

Due to possible systematic effects, it is desirable to use (3) and (4) to decode polarization angle rather than (2). This is because any polarized, unchopped source will also appear at this frequency. In Figure 3.2, the light Ray 1 comes from the source, is chopped at the chop frequency f_{chop}, and is polarized by an external polarizing grid. This is the light that will ultimately fall into the $4f_{HWP}$ sidebands and reside in the well-defined frequency bands described in terms (3) and (4). Ray 2 is chopped power that is not polarized; these rays will add extra power to term (1). Ray 3 is polarized but has bypassed the chopper; this will result in extra power in term (2).

$$I_{outsys} = \frac{I_{sys}}{2}(1 + \frac{1}{2}P_{sys}\cos(4\omega_{HWP}t - 2\alpha_{sys})) \tag{3.13}$$

This signal will have a different phase $2\alpha_{sys}$ where α_{sys} is the polarization angle of the contaminant source. Decoupling this phase from the desired phase of the chopped calibration source is not possible.

A single noise-free detector with a perfect polarizing grid and 100% polarized chopped source will produce the time stream signal shown in the top panel of Figure 3.3. Because the rotation angle of the HWP is known as a function of time, the signal is interchangeable between the time

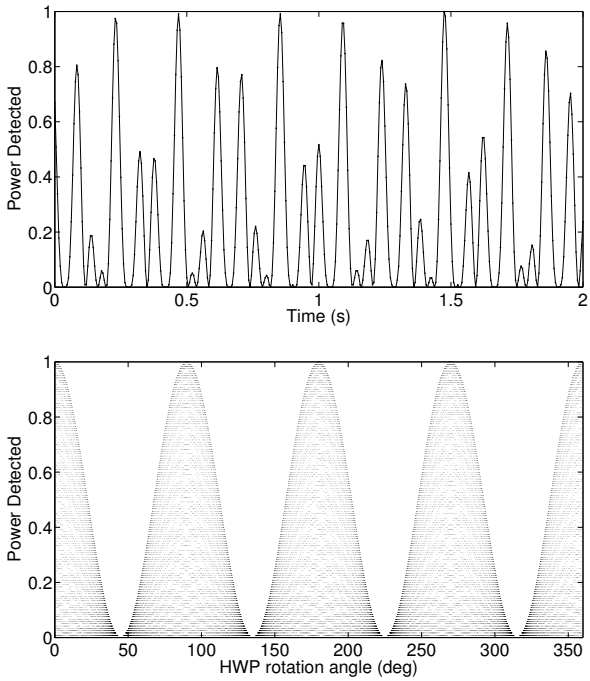

Figure 3.3: Simulation of the bolometer signal for the model HWP system. Top figure shows one rotation in the time domain. The bottom figure is 10 minutes overlayed in the angle domain. The simulation is of HWP rotation frequency $f_{HWP} = 2$ Hz and a chop frequency $f_{chop} = 13$ Hz.

and HWP-angle domains. The bottom panel of Figure 3.3 shows the HWP-domain signal.

3.1.3 Extraction of polarization angle from a time-domain bolometer signal

We seek to understand and outline the mathematical process needed to extract the incoming polarization angle α_{in} from the time-domain signal discussed in the previous section. The details of the software pipeline used to extract polarization angle from EBEX data for various calibration measurements will be discussed in section 3.2.

The first step is to multiply the time stream by$\cos(\omega_{chop}t)$), which is obtained by band-pass filtering it from the original time signal I_{out} to obtain $\frac{I_0}{2}(1+\cos(\omega_{chop}t))$ and then removing an offset and normalizing.

$$I_{out}(t) \times \cos(\omega_{chop}t) = \cos(\omega_{chop}t)\frac{I_0 P_{in}}{8}(\cos(\omega_{chop}t - 4\omega_{HWP}t + 2\alpha_{in}) + \frac{I_0}{2}\cos(\omega_{chop}t) \times N$$

$$= \frac{I_0 P_{in}}{16}\cos(4\omega_{HWP}t - 2\alpha_{in}) \tag{3.14}$$

where N represents the collection of terms 1, 2 and 4 from section 3.1.2 that will not be used. Next, we multiply by the HWP angle $\theta_{HWP}(t)$, which in the case of constant rotation speed is $t \times \omega_{HWP}$. This will provide Q and U in the time domain.

$$\begin{aligned} Q(t) &= I_{out}(t) \times \cos(\omega_{chop}t) \times \cos(4\theta_{HWP}(t)) \\ &= \frac{I_0 P_{in}}{16}\cos(4\omega_{HWP}t - 2\alpha_{in})\cos(4\theta_{HWP}(t)) \\ &\sim \frac{I_0 P_{in}}{16}\cos(4\omega_{HWP}t - 2\alpha_{in})\cos(4\omega_{HWP}t) \end{aligned} \tag{3.15}$$

$$\begin{aligned} U(t) &= I_{out}(t) \times \cos(\omega_{chop}t) \times \sin(4\theta_{HWP}(t)) \\ &= \frac{I_0 P_{in}}{16}\cos(4\omega_{HWP}t - 2\alpha_{in})\sin(4\theta_{HWP}(t)) \\ &\sim \frac{I_0 P_{in}}{16}\cos(4\omega_{HWP}t - 2\alpha_{in})\sin(4\omega_{HWP}t) \end{aligned} \tag{3.16}$$

This demodulation moves the relevant polarization angle information $Q(t)$ and $U(t)$ to DC. Multiplying and removing the non-DC terms gives:

$$Q = \frac{I_0 P_{in}}{32}\cos(2\alpha_{in})$$

$$U = \frac{I_0 P_{in}}{32}\sin(2\alpha_{in}) \tag{3.17}$$

Q and U will be larger by a factor of 2 if we include both sideband terms after the first demodulation. We multiply Q and U so they are consistent with their original definition where the maximum value of $I_{in} = I_0$:

$$Q = I_0 P_{in}\cos(2\alpha_{in})$$

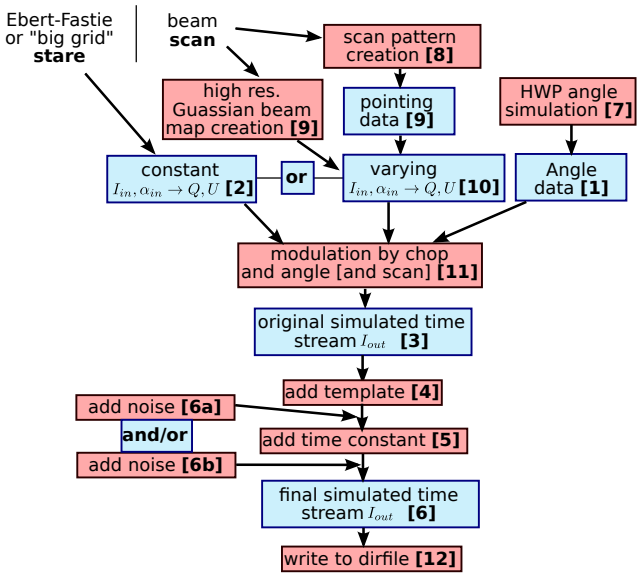

Figure 3.4: Schematic overview of the polarized chopped-source calibration simulation procedure

$$U = I_0 P_{in} \sin(-2\alpha_{in}) \tag{3.18}$$

Now,

$$\alpha_{in} = \frac{1}{2} \arctan(\frac{U}{Q})$$

$$I_p = I_0 P_{in} = \sqrt{Q^2 + U^2} \tag{3.19}$$

It is theoretically possible to obtain Q and U directly from the $4\omega_{HWP}$ signal. This is a consequence of the fact that the chopped source chops between 0 and I_0 and thus has an average DC level that is $I_0/2$. This method has the disadvantage of mixing in any instrumental polarization signal due to the instrument mixing unchopped, unpolarized signal into unchopped, polarized signal. It is used later in this work to investigate this effect.

$$Q(t) = I_{out}(t) \times \cos(4\theta_{HWP}(t)) = \frac{I_0 P_{in}}{4} \cos(4\omega_{HWP} t - 2\alpha_{in}) \times \cos(4\theta_{HWP}(t)) = \frac{I_0 P_{in}}{8} \cos(2\alpha_{in}) \tag{3.20}$$

3.1.4 Simulated data in the angle domain

We developed a simulation to better understand the analysis of calibration data from the EBEX instrument. We show a summary of the process in Figure **3.4.** We highlight some of the steps below for a calibration test that does not involve a scanning gondola, which we refer to as a "stare" configuration. This simulation will be expanded in later sections to cover the various physical calibration setups that were used; we include these extra steps in Figure **3.4**, which we will reference later.

1. A set of HWP angle data is created. Using the known number of slots in the HWP encoder and given a rotation speed, we create a set of time-ordered HWP angles $\theta_{HWP}(t)$. We feed this into the simulation because the HWP decoding code produces the same type of array (section 2.5.1. It is possible to add small HWP speed variations to better simulate the physical behavior of the HWP.

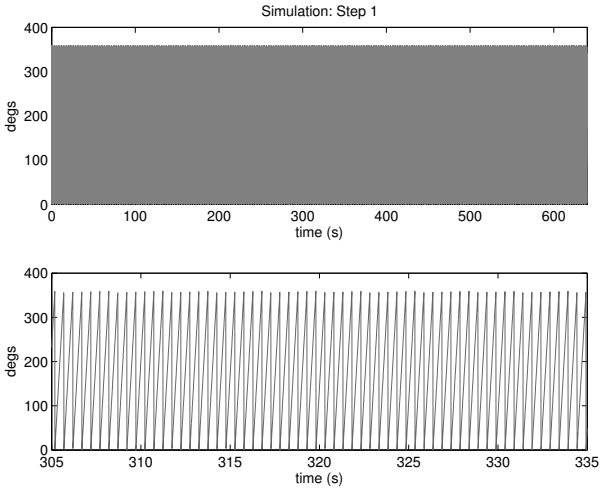

Parameters:

- $f_{HWP} = 1.98$ Hz
- $\frac{\Delta f_{HWP}}{f_{HWP}} = 0$ (no HWP speed variations included)

2. For calibration tests that do not involve gondola scans, the simulation is set to "stare" mode and the attitude is fixed. All data points in the time series, then, have the same incoming power $I_{in}(t) = I_{in}$ and polarization angle $\alpha_{in}(t) = \alpha_{in}$:

$$Q = \sqrt{\frac{I_{in}^2}{1 + \tan(\alpha_{in})}}$$

$$U = Q \times (1 + \tan(\alpha_{in}))$$

Parameters:

- $\alpha = 22.5°$
- $I_p = 1000$ counts

3. A simulated time series for an individual bolometer $I_{bolo}(t)$ can be calculated given a polarization fraction P_{in} and a source chop frequency f_{chop}.

$$\alpha_{in} = \frac{1}{2}\arctan\left(\frac{U}{Q}\right)$$

$$I = \sqrt{U+Q}$$

$$I_{bolo}(t) = I(t)\times(1+\cos(2\pi f_{chop}t))\times (1+\frac{P_{in}}{2}\cos(4\theta_{HWP}(t)-2\alpha_{in}))$$

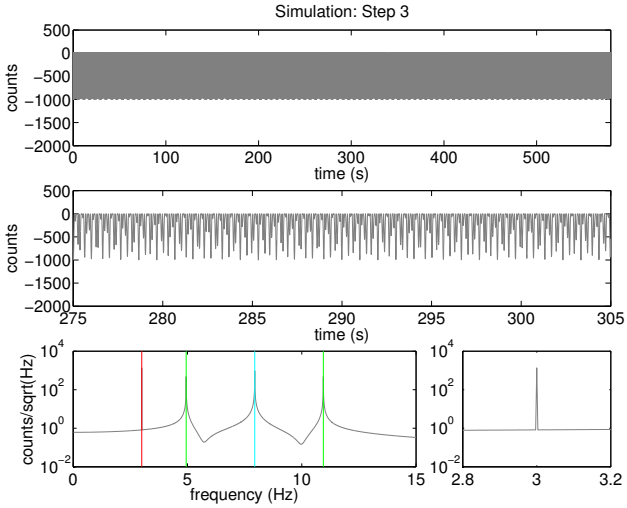

Parameters:

- $f_{chop} = 3.00$ Hz
- $P_{in} = 1$
- Scan length = 600 s

4. Extra power is added at the frequency $4f_{HWP}$. This is referred to as part of the "HWP template", and represents partially polarized, unchopped light that is modulated by the HWP.

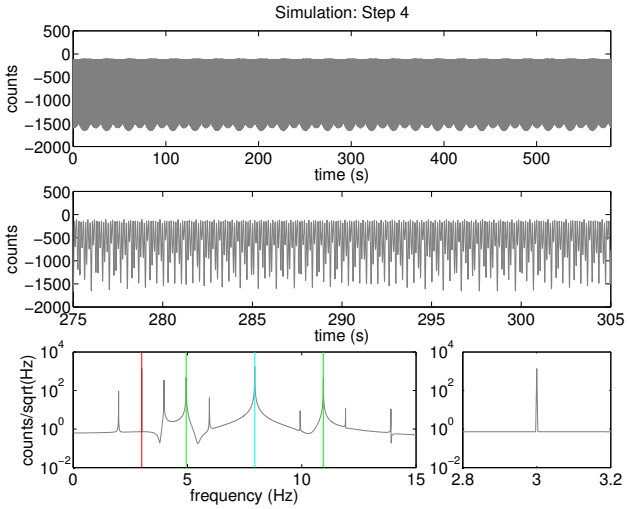

Parameters:

- $I_{4Hz} = 1000$ counts

5. The time series $I_{bolo}(t)$ is run through a single-pole filter. This simulates the optical time constant of our TES bolometers.

Parameters:

- $f_{3dB} = 5$ Hz

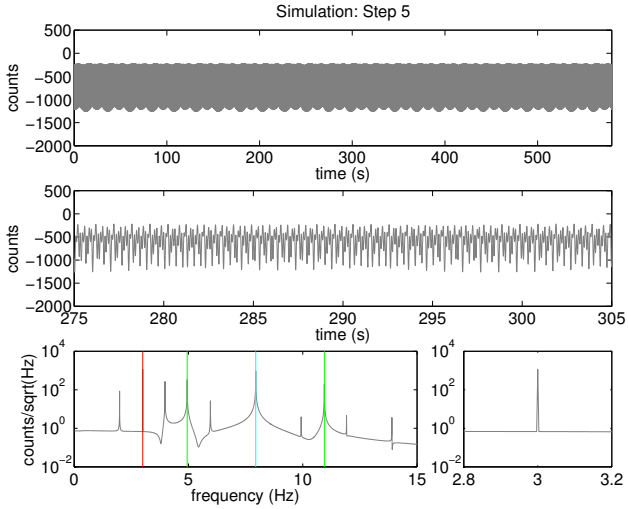

6. White noise is added to simulate the intrinsic bolometer noise. The level is adjusted to match a specific target detector to simulate in the frequency domain. Noise can also be added before step 5.

Parameters:

- I_{noise} =50 counts or 5 % (measured as one standard deviation in the time domain) of amplitude of polarized signal I_p

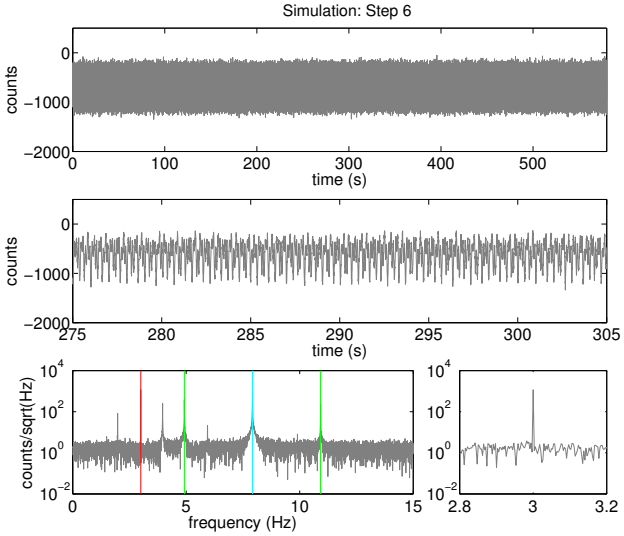

Figure 3.5 shows a typical set of simulated data and the actual bolometer data it was modeled after in the frequency domain.

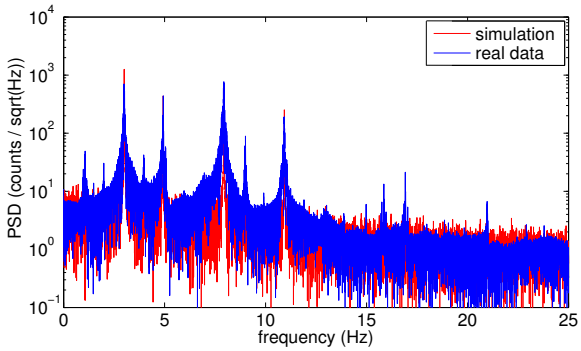

Figure 3.5: Power spectra of simulated data and actual calibration data in the simulation example. Tuning of the simulation time constant, noise levels, and template allow us to make a good approximation of a real time stream.

3.1.5 Real data in the angle domain

To check whether all of the characteristics of our calibration data are captured by our simulation, we compare a real detector from the "big grid" test and a simulated detector in the angle domain. The real detector in the top panel in Figure 3.6 shows features not captured in our simple model in section 3.1.2. However, by modifying the polarization efficiency P, and adding a template and adjusting its size and phase, we create a simulation that has these features (Figure 3.6, bottom). We investigate the template in greater detail in section 3.5.

3.2 Data analysis pipeline

We developed a data analysis pipeline to handle general calibration data. Various calibration tests were done on EBEX, and typical calibration data for these tests will look somewhat different; data analysis notes specific to certain calibration tests are handled in their respective sections. However, all optical, polarization-related calibration data taken for EBEX has certain similarities, and the first steps of the analysis pipeline are the same. All data has the following parts:

1. Data from one or more of the ∼1500 TES bolometers in EBEX, recorded in integer counts at 190.7 Hz. One file exists for each bolometer.

2. Data from the HWP, decoded in the manner described in section 2.5.2 and resampled to 190.7 Hz.

3. AZ and EL attitude data, recorded at 100 Hz, or in the case of frequency dependent

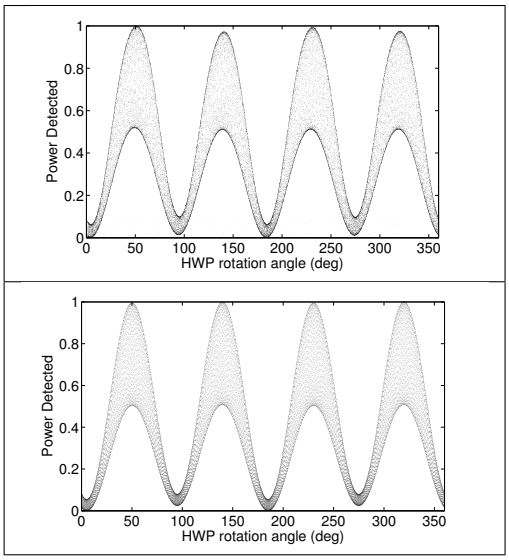

Figure 3.6: Simulated data (bottom) vs. actual calibration data (top) in the angle domain. We have added template with an amplitude of 1.8 times the input signal level and reduced the polarization fraction to 0.8. These changes to our simple simulation (Figure 3.3) better approximate our real calibration data.

polarization rotation, a 5 Hz channel recording the frequency of the incident light from the Ebert-Fastie monochrometer.

The following process is used to convert the raw data into a time stream of detected polarization angle for each bolometer.

For this example we use data taken from the center of a band during Ebert-Fastie calibration test (section 3.6.2) The simulation pipeline detailed in section 3.1.4 is used to create a set of similar data for comparison. To demonstrate this process, the simulated data and real data are run through the pipeline side by side, showing the condition of the data at each step. We reference numerically the steps as shown in the schematic in Figure 3.7.

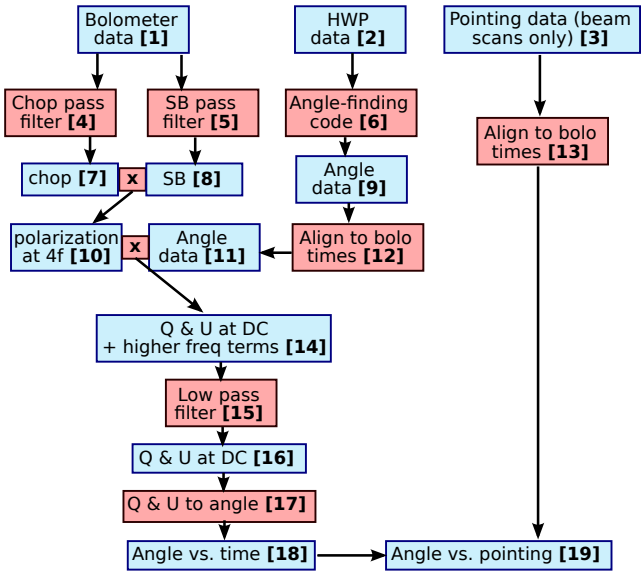

Figure 3.7: Schematic overview of the polarized chopped-source calibration data analysis procedure

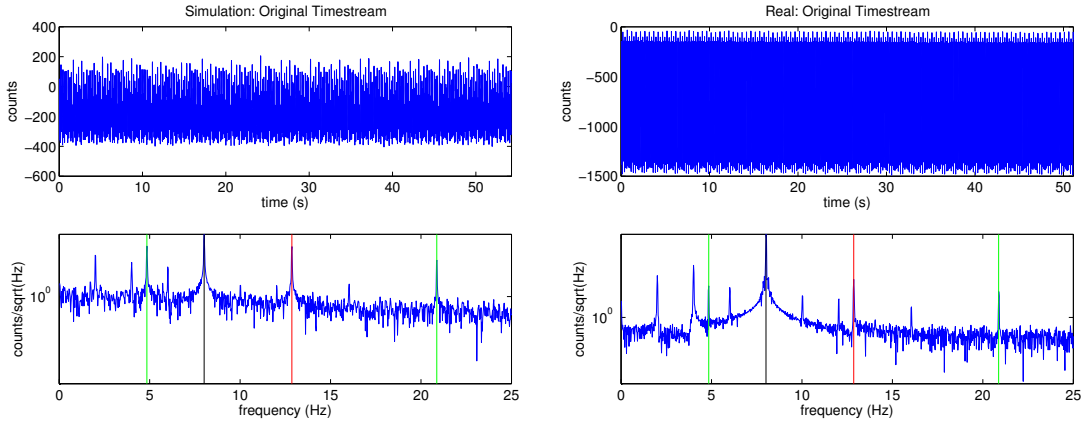

The original time streams ([**1**]) before manipulation by the analysis pipeline are shown above. The simulation parameters are not identical to the ones used in section 3.1.4 so as to better approximate the frequency dependent polarization data from this particular detector. Relevant modified parameters are as follows:

- $f_{HWP} = 2.003$ Hz
- $f_{chop} = 12.86$ Hz
- $I_{in} = 70$ counts

- $I_{4Hz} = 400$ counts
- $I_{noise} = 4$ %
- Scan length is 500 seconds

A comparison of the simulated and real calibration data in the frequency domain is shown in Figure 3.5. Before the process begins, a time-constant removal procedure (section 3.3) may be applied to the data.

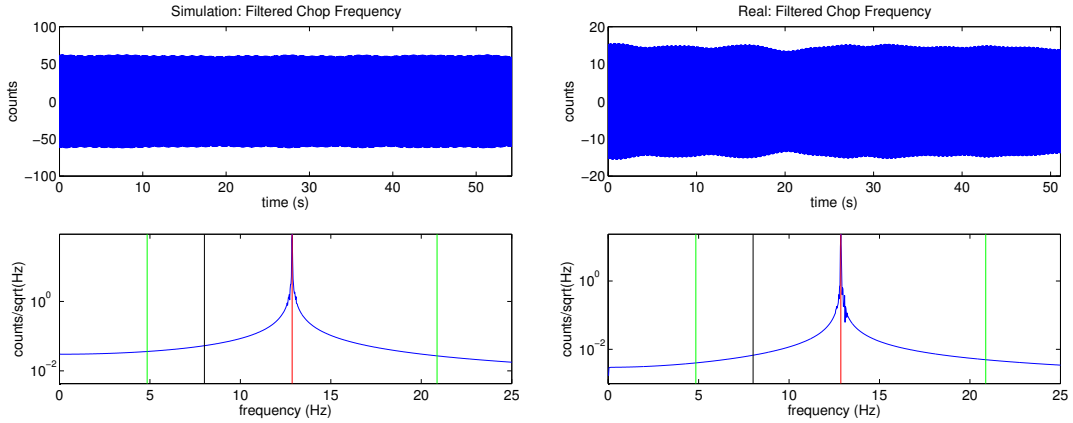

A bandpass filter is run around the chop frequency f_{chop} ([**4**]) All bandpass filters used in this example are phase-preserving 2000 stage FIR filters with a total 3dB width of 0.2 Hz. The optimization of these filters is described in sections 3.7.2, 3.8.2, and 3.9.6.

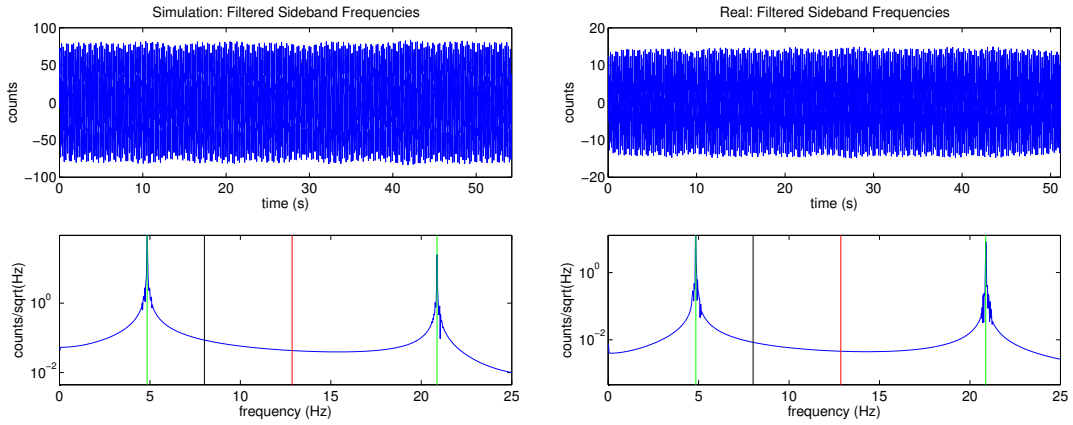

Bandpass filters are run around the sideband frequencies $4f_{HWP} \pm f_{chop}$([**8**]).

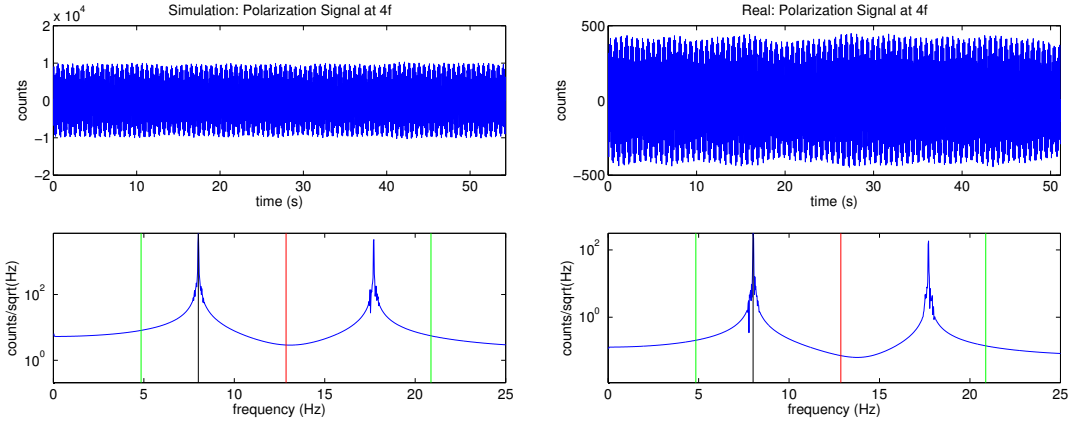

Following the procedure described in section 3.1.3, the filtered f_{chop}data is multiplied by the filtered sideband data $4f_{HWP} \pm f_{chop}$. This moves the data containing the polarization signal we are interested in to $4f_{HWP}$ and $8f_{HWP}$ ([**10**]).

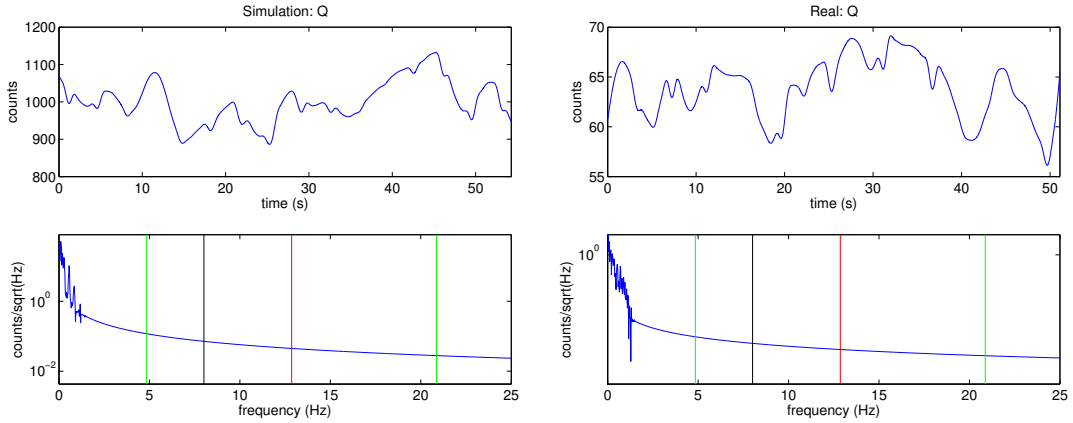

Q and U are obtained by multiplying the now $4f_{HWP}$ data by the cosine and sine of the angle of the HWP at the time of each bolometer data point ([**16**]). The HWP angles are decoded as described in section 2.5.2 and then linearly interpolated to match sampling times of the bolometer data ([**12**]). This moves the polarization signal we are looking for to low frequencies. We assume that any fluctuations of the incident polarization angle α_{in} faster than 0.2 Hz are not physical and filter out higher-frequency peaks with a low-pass filter.

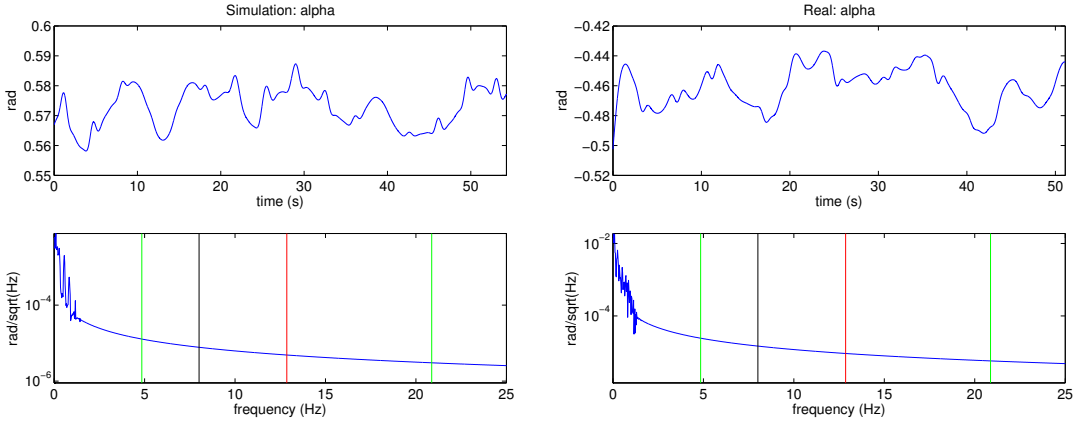

$\alpha_{in}$is obtained from Q and U as described in section 3.1.2 ([**17**]).

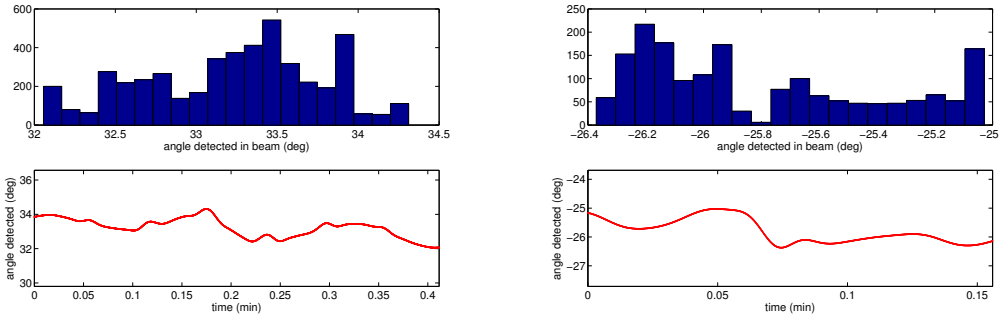

The results of the analysis of one Ebert-Fastie data segment are shown above, and several segments combined are shown below.

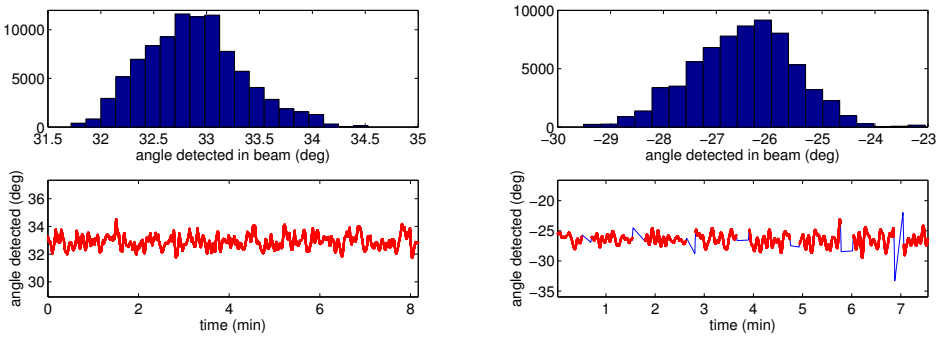

We have obtained polarization angles from our data set, and shown the process appears to work both for real and simulated data. We also obtain a standard deviation σ_α, which we find

is related to our noise level but doesn't necessarily encode the error on the mean; we investigate this in detail in section 3.10. We will occasionally reference this value for a specific detector, or the average of this value for a set of detectors, which is not to be confused with the standard deviation of the mean values of α_{in} measured for a set of detectors.

3.3 Bolometer optical time constants

3.3.1 Introduction

The TES bolometers used in EBEX have a characteristic optical time constant. This time constant is set by geometry of the detectors, which are designed to have specific values of thermal conductance and saturation power. Optimization of these detectors for EBEX yields a designed time constant of 3 ms or 53 Hz. Lower time constant frequencies are observed. It is predicted that the associated time constant rolloff behaves like a simple one-pole RC-filter [31]; we find that this model is only an approximation for some detectors but do not find a physical model that better fits the data.

Because an RC filter has an associated phase shift, the phase of sideband frequencies $4f_{HWP} \pm f_{chop}$ is modified by this optical filter. Since this phase is extracted as the incident polarization angle as shown in section 3.1.3, it is essential to understand this effect. Figure 3.8 shows an example of one-pole RC-filters at typical observed frequencies. Since $I_{out} \sim \cos(4\omega_{HWP}t - 2\alpha_{in}))$, the first order modification to the otherwise expected measurement of a (non-chopped) angleα_{in} will be one half of the filter phase at the relevant sideband frequency. It is clear that for typical sideband frequencies of 3 – 20 Hz and typical observed rolloff frequencies of $\sim$ 10 Hz – lower than the design value – this is a very large effect for an experiment with a desired polarization sensitivity of 0.3°.

For a single pole filter, the rolloffs in magnitude and phase shown in Figure 3.8 are:

$$Y_{out} = Y_{in}\left(\frac{1}{1 + (\frac{f_{in}}{f_{3DB}})^2}\right)^{1/2} \tag{3.21}$$

$$\phi_{out} = \arctan\left(-\frac{f_{in}}{f_{3DB}}\right) \tag{3.22}$$

3.3.2 Effect of optical time constant on the reported value of α_{in}

We derive the reported value of the input polarization angle α_{in} we expect our analysis pipeline to produce given data with some cutoff frequency f_{3DB}. Consider the case where the sidebands of the input signal into the bolometric detectors, as derived in section 3.1.3, now have a phase shift caused by the finite time constant of the detector:

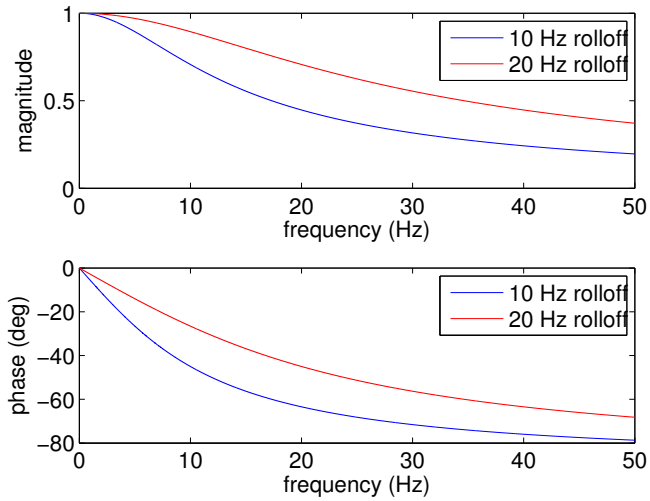

Figure 3.8: Example one-pole RC filters in fractional magnitude (top) and phase angle (bottom) for two typical observed rolloff frequencies.

$$I_{out}(t) = \frac{I_0}{16}(\cos(4\omega_{HWP}t - \omega_{chop}t - 2\alpha_{in} + \phi_{low}) + \cos(4\omega_{HWP}t + \omega_{chop}t - 2\alpha_{in} + \phi_{high})) \quad (3.23)$$

for $P_{in} = 1$ and $4\omega_{HWP} > \omega_{chop}$. The signal at the frequency ω_{chop}will be use for demodulation, but it now also has a phase shift:

$$I_{chop}(t) = \cos(\omega_{chop}t + \phi_{chop}) \quad (3.24)$$

Demodulating and ignoring terms at frequencies other than DC gives

$$I_{out}(t) \times I_{chop}(t) \times \cos(4\theta_{HWP}(t)) = \frac{I_0}{16}(\cos(-2\alpha_{in} + \phi_{low} + \phi_{chop}) + \cos(\omega_{chop}t - 2\alpha_{in} + \phi_{high} - \phi_{chop})) = Q(t) \quad (3.25)$$

$$I_{out}(t) \times I_{chop}(t) \times \sin(4\theta_{HWP}(t)) = -\frac{I_0}{16}(\sin(-2\alpha_{in} + \phi_{low} + \phi_{chop}) + \sin(\omega_{chop}t - 2\alpha_{in} + \phi_{high} - \phi_{chop})) = U(t) \quad (3.26)$$

The high and low frequency terms can be separated before demodulation. Taking only the

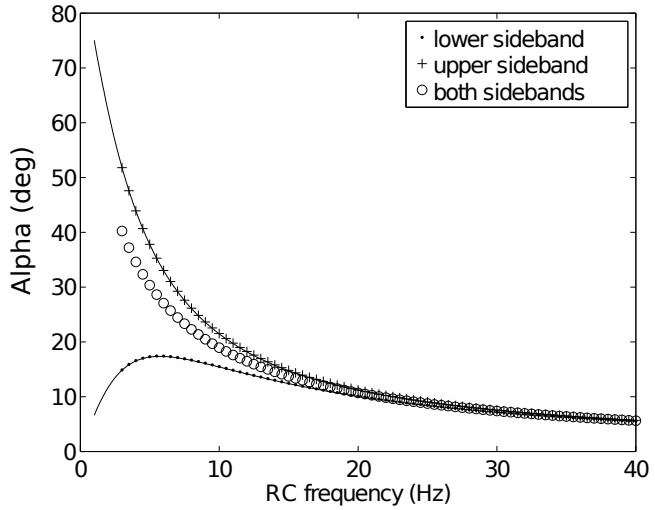

Figure 3.9: Simulation of effect of one-pole RC filter on measured value of α_{in}, when doing the analysis process using only the upper, only the lower, and both sidebands for values of $\omega_{HWP} = 2$ Hz and $\omega_{chop} = 3$ Hz. Solid lines are analytic predictions.

low frequency sideband terms,

$$(\frac{U}{Q})_{low} = -\tan(-2\alpha_{in} + \phi_{low} + \phi_{chop}) = \tan(2\alpha_{in} - \phi_{low} - \phi_{chop}) \tag{3.27}$$

$$\arctan(\frac{U}{Q})_{low} = 2\alpha_{low} = 2\alpha_{in} - \phi_{low} - \phi_{chop} \tag{3.28}$$

Similarly,

$$\arctan(\frac{U}{Q})_{high} = 2\alpha_{high} = 2\alpha_{in} - \phi_{high} + \phi_{chop} \tag{3.29}$$

Hence, the expected reported values of α_{low} and α_{high} to come out of the analysis for an input polarization of α_{in} for each the lower and upper sidebands is

$$\alpha_{low} = -\frac{1}{2}(\phi_{low} + \phi_{chop}) + \alpha_{in} \tag{3.30}$$

$$\alpha_{high} = -\frac{1}{2}(\phi_{high} - \phi_{chop}) + \alpha_{in} \tag{3.31}$$

Noting equation 3.12 for the case where $4\omega_{HWP} < \omega_{chop}$ and repeating the argument it can be seen that in this case

$$\alpha_{low} = -\frac{1}{2}(-\phi_{low} + \phi_{chop}) + \alpha_{in} \tag{3.32}$$

The simulation detailed in section 3.1.4 includes the option to filter the time stream with a one-pole RC filter. This filtered simulated data can then be run through the analysis pipeline. The polarization analysis software can be set to choose one or the other of the sidebands (or both). These analytical models can be seen plotted with data points derived from the use of the simulation and analysis software in Figure 3.9 with $\alpha_{in} = 0$.

3.3.3 Real time measurement of time constant assuming single-pole rolloff using sideband magnitude

Because of the systematic effects on the reported value of the incoming polarization angle α_{in}, we developed a technique for rolloff removal. We assume detectors are well-approximated by a single-pole phase response. This technique has the advantage of being applicable to any data that includes a chopped source, and can be used on the exact data that is being analyzed. All of the time constant removal techniques we discuss are applied to the raw data timestreams before they are subjected to our data analysis pipeline (section 3.2).

The method starts with a mathematical consequence of chopped continuously rotating HWP polarization data described in section 3.1.2: that in the case of no rolloff, the magnitude of the $4f_{HWP} \pm f_{chop}$ sidebands will be the same. The bolometer's optical filtration causes the higher-frequency sideband to have a lower magnitude than the lower-frequency sideband. The magnitudes of these two sidebands constrain the rolloff frequency f_{3dB} of the bolometer's optical filter. The magnitudes imply a value of f_{3dB} via equation 3.21. Once f_{3dB} is measured, the data can be convolved with an inverted complex single-pole RC filter with the same rolloff frequency f_{3dB} to remove the effect of the optical time constant. Noise in the signal will cause error in the measurement of f_{3dB}.

The problem is then one of making a good measurement of the power in each sideband. Two methods were tried:

1. The simplest method is to choose a reasonable bandwidth around the peaks, and integrate the power in the band. A simulation run with typical noise and rolloff values of 5% and 5 Hz respectively suggests that 0.6 Hz is a good choice (red lines in Figure 3.10).

2. We can bandpass filter the peaks and measure the power in the time domain by taking the standard deviation. Simulations suggest this method achieves the best results with a sharp 1.5 Hz wide filter. In the case of a beam scan using this method, we use only data that falls within our nominal beam of 0.04°.

We compare these methods in section 3.3.5.

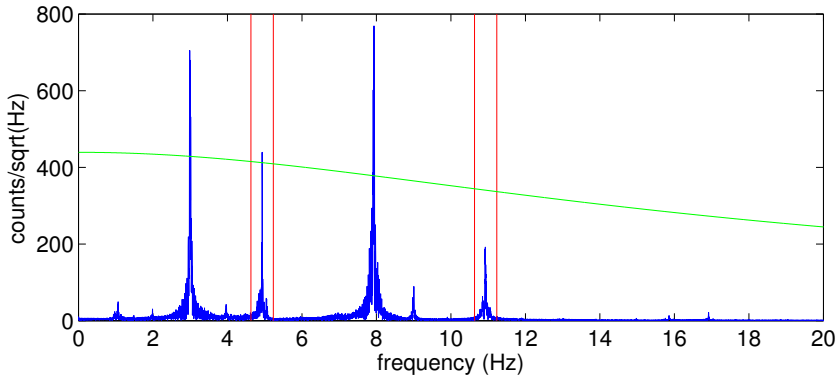

Figure 3.10: Example of "power"-based RC removal process using real calibration data. Red lines show bands used for power integration; green curve shows the single-pole rolloff calculated from the power integration (13.4 Hz in this example).

3.3.4 Real time measurement of time constant assuming single-pole rolloff using sideband phase

We describe a second, independent technique for real time measurement of detector time constants. Because a single-pole rolloff causes an error in the value α_{in} in a predictable manner (Figure 3.9), one has the option of simply running the analysis (specifically, following the process outlined in Figure 3.7 twice) using each the lower and upper sidebands and then solving the system of equations that governs their relationship. As in section 3.3.3, we finish the analysis process by convolving the data with an inverted complex single-pole RC filter with the rolloff frequency f_{3dB} to remove the effect of the optical time constant and run the analysis a third time to determine our final value of α_{in}. It will be shown in section 3.3.5 that this technique produces the most accurate results; consequently it is examined in the most detail and is used by default in the data analysis in remainder of this work.

We denote the *reported* value of α_{in} for these cases as α_{low} and α_{high}, and the "correct" value – that is, the value that would be obtained from a time constant-free detector, which is the true physical value of the input polarization that we are seeking – as α_{in}. The first three equations needed are the assumption of single-pole rolloff in phase:

$$\arctan(\frac{-f_{high}}{f_{3DB}}) = \phi_{high}$$

$$\arctan(\frac{-f_{low}}{f_{3DB}}) = \phi_{low}$$

$$\arctan(\frac{-f_{chop}}{f_{3DB}}) = \phi_{chop} \tag{3.33}$$

where f_{high} and f_{low} are the frequencies of the high and low sidebands, f_{chop} is the frequency of the chopped source, and ϕ_{high}, ϕ_{low}, and ϕ_{chop} are their respective phase delays from the bolometer time constant.

The final two equations can be derived from adding and subtracting equations 3.30 and 3.31 from section 3.3.2, for the case where $4\omega_{HWP} > \omega_{chop}$.

$$\begin{aligned} -\phi_{low} + \phi_{high} - 2\phi_{chop} &= 2\alpha_{low} - 2\alpha_{high} \\ 4\alpha_{in} - \phi_{low} - \phi_{high} &= 2\alpha_{low} + 2\alpha_{high} \end{aligned} \tag{3.34}$$

Or, in the case where $4\omega_{HWP} < \omega_{chop}$, we instead use equations 3.32 and 3.31 and get:

$$\begin{aligned} \phi_{low} + \phi_{high} - 2\phi_{chop} &= 2\alpha_{low} - 2\alpha_{high} \\ 4\alpha_{in} + \phi_{low} - \phi_{high} &= 2\alpha_{low} + 2\alpha_{high} \end{aligned} \tag{3.35}$$

This method will be referred to as "phase" time-constant removal. While it is computationally efficient, it is not terribly transparent. It is useful to examine what is happening in more detail, since a better intuitive understanding will help explain analysis results. Consider the difference between α_{low} and α_{high} (Figure 3.11) for two different cases, one in which $4\omega_{HWP} > \omega_{chop}$ (left) and one where $4\omega_{HWP} < \omega_{chop}$ (right). Each occur in EBEX calibration measurements, the former for cryostat-only calibration using a large fixed grid covering the cryostat window (the "big grid" method detailed in section 3.8), and the latter for full experiment beam scans (section 3.9). We focus on the difference $\alpha_{low} - \alpha_{high}$ because we don't know α_{in} a priori; α_{low} and α_{high} contain what we view at this point an arbitrary offset. Our technique can only map the difference to the time constant.

It can be seen in Figure 3.11 in the left panel that if the two sidebands produce different values of α by more than 90°, it can be said with certainty that the detector cannot be accurately described by a single-pole RC-like filter.

The right panel of Figure 3.11 shows a degeneracy in the value $\alpha_{low} - \alpha_{high}$. Unfortunately, for values of $4f_{HWP} < f_{chop}$, one is forced to choose between two different possible values of f_{3dB} and consequently α_{in}. In these cases we will need to use other information to attempt to break the degeneracy; unless noted we choose the results of the power measurement.

Taking a look at the phase shifts in the time domain can also help in understanding this method. It is impossible to compare the high and low sidebands in the time domain until after first demodulating by multiplying by the chop frequency component $\cos\omega_{chop}t$. At this point

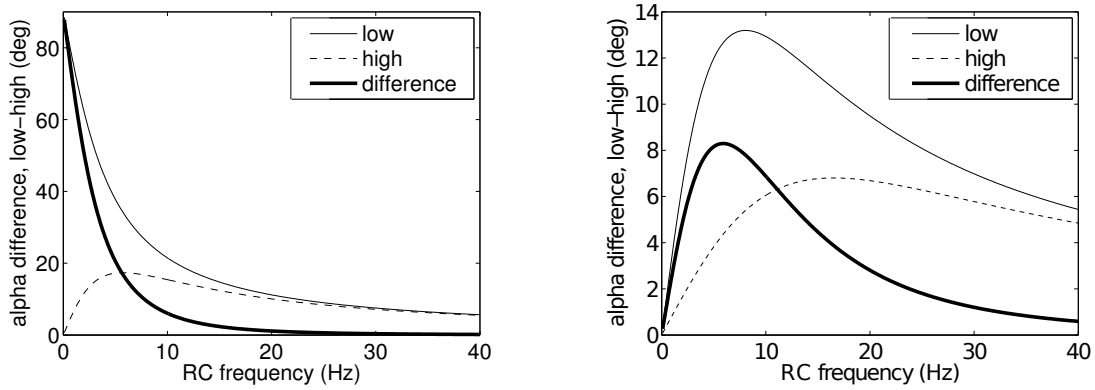

Figure 3.11: Analytical calculation of the difference between observed values of α_{in} using analysis of the low frequency sideband (α_{low}) and high frequency sideband (α_{high}), vs. f_{3dB}. Left shows case where $4f_{HWP} > f_{chop}$; values are $f_{HWP} = 2$ Hz and $f_{chop} = 3$ Hz. Right is case where $4f_{HWP} < f_{chop}$; values are $f_{HWP} = 2$ Hz and $f_{chop} = 13$ Hz. Thick curve is difference $\alpha_{low} - \alpha_{high}$.

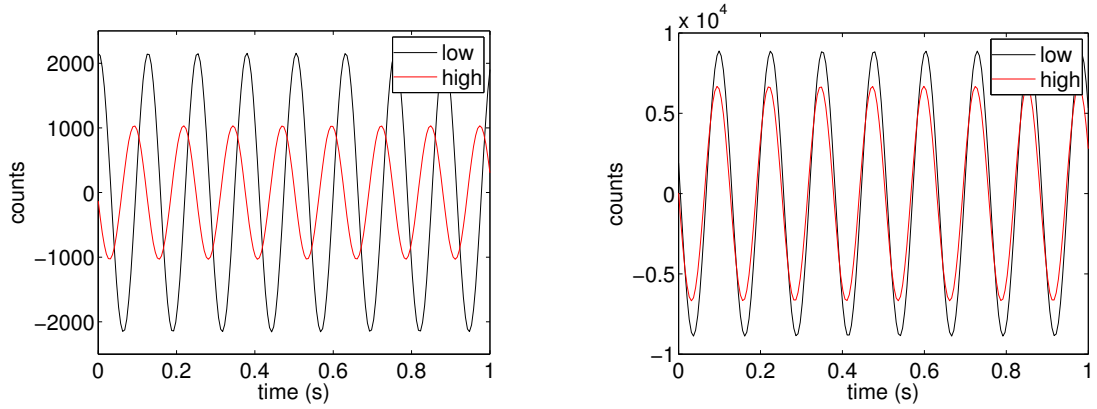

Figure 3.12: Sidebands of $4f_{HWP}$ in the time domain after the first demodulation step of the analysis pipeline, multiplication by $\cos\omega_c t$ (see step 10 in Figure 3.7). Left panel shows data that was simulated using an value $f_{3DB}$of 2 Hz, right panel shows a value of $f_{3DB}$of 10 Hz.

f_{3DB}	no removal	freq domain	time domain	phase
no rolloff	0.001°	–	–	–
20 Hz	11.208°	−0.043°	0.002°	0.002°
10 Hz	21.503°	0.041°	0.002°	0.001°
5 Hz	37.819°	0.247°	0.007°	0.000°

Table 3.1: The simulation is used to show the result of using the data analysis pipeline with different RC removal processes on an input polarization of $\alpha_{in} = 0°$, with $f_{HWP} = 2$ Hz and $f_{chop} = 3$ Hz.

both sidebands have been moved to the carrier frequency $4f_{HWP}$ and can be compared. This was done using the simulation in Figure 3.12. With a lower frequency f_{3dB} of 2 Hz compared to 10 Hz, the left panel shows a greater phase shift and a smaller amplitude. Note that in this time domain a phase shift of up to 180° can occur, the addition of two RC-like filters of up to 90°.

To double check our nominal analysis process we fit these curves to find the phase and make use of the relationships developed in section 3.3.4 to compare.

f_{3dB}	$\Delta\alpha$, nominal	$\Delta\alpha$, phase fit	error
2 Hz	50.452°	50.446°	−0.006°
10 Hz	6.055°	6.049°	0.006°

These methods produce effectively identical results, but the nominal method presented above is used in actual analysis due to it being more computationally efficient.

3.3.5 Testing of time constant removal methods with simulation

We compare the accuracy of the time constant measurement and removal methods developed in the previous sections. We use our simulation pipeline to measure the efficacy of this mode of time constant removal, with the continued assumption of single-pole rolloff. To begin with, the simulation is run with no noise added. As described in section 3.1.4, step 5, once the simulation created a time domain signal, we convolve it with a single-pole filter.

Having created a simulated detector, we then run our full analysis pipeline (section 3.2) on the data, using the three different time constant removal methods discussed in sections 3.3.3 and 3.3.4. We compare the resultant observed value of α_{in} with the known value of α_{in} input into our simulation. In this noise-free with configuration, the phase RC removal procedure is able to recover original input polarization within ~ 0.002 degrees (Table 3.1). We find that our frequency domain method is a rougher approximation than the other two methods. While it may be feasible to better optimize this method, we consider it mostly for pedagogical value and focus on the other two methods from this point on.

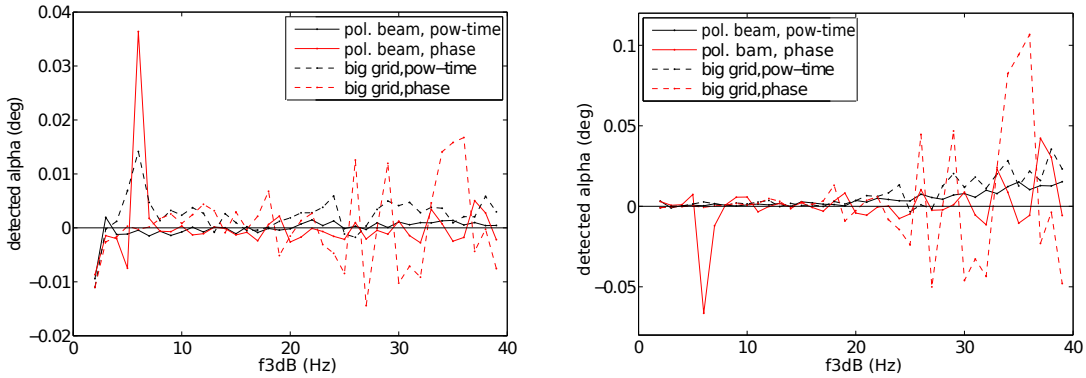

Figure 3.13: Error in α_{in}vs. f_{3dB} (left) and error in α_{in}vs. f_{3dB} (right) for a zero-noise simulation and data analysis process. "Pol. beam" case uses $f_{chop} = 13$ Hz, "big grid" case uses $f_{chop} = 3$ Hz, and all cases use $f_{HWP} = 2$ Hz; we show the "power" removal method in black and the "phase" removal method in red.

We repeat this process – a noise-free simulation and data analysis – for a broad range of detector time constants; we compare the methods and look for systematic errors.

In Figure 3.13 we show the resultant errors in reconstruction of α_{in} and f_{3dB} in the left and right panels respectively. We consider two removal methods, power and phase (black and red) and two configurations: that like our polarized beam scan setup and that like the "big grid" stare test (solid and dashed). The polarized beam setup has a value $f_{chop} = 13$ Hz and the "big Grid" a value $f_{chop} = 3$ Hz; $f_{HWP} = 2$ Hz in all cases. Without noise, angle can be reconstructed within $\sim 0.04°$ (Figure 2.11). Errors in detected frequency increase with increasing rolloff frequency, especially in the "big grid"-like case; its chop frequencies of 5 Hz and 11 Hz have a relatively weak lever arm on a rolloff frequency of >20 Hz. However, this error is mitigated by the fact that higher frequencies create a smaller systematic effect in the measurement of the polarization angle α_{in}. We also see a small deviation near 6 Hz in the polarized beam configuration; this is the inflection point in figure 3.11.

Before introducing noise to the simulation, we consider the nature of our noise: an understanding of our bolometers and readout system suggests that noise will be split between that which is affected by the time constant – optical noise – and that which is not – electrical noise. Each affects our models differently: in the case where optical signal rolls off but noise does not, the higher sideband signal is quickly buried.

We turn to our data sets to attempt to assign the appropriate amount of noise pre- and post-time constant in our simulation. We consider the ratios of the amplitudes of each sideband in the case of signal and in the case of no signal. We take no-signal cases to be before we turn on

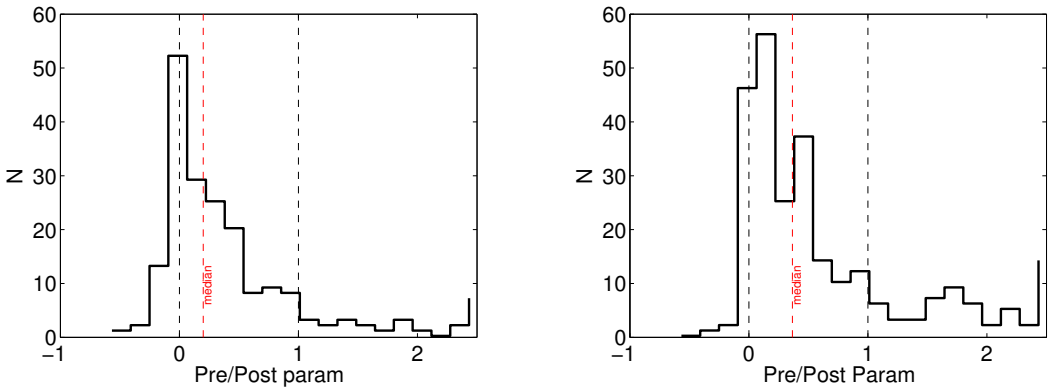

Figure 3.14: The parameter pre- vs. post- noise parameter F encodes the fraction of noise that is unaffected (value 0) and entirely affected (value 1) by the time constant in our "big grid" (left) and polarized beam map (right) data sets.

the chopper in the "big grid" test, and outside the beam in the polarized beam test.

$$A_{signal} = \frac{P_{low-signal}}{P_{high-signla}} \tag{3.36}$$

$$A_{noise} = \frac{P_{low-noise}}{P_{high-noise}} \tag{3.37}$$

We assign a parameter

$$F = \frac{A_{noise} - 1}{A_{signal} - 1} \tag{3.38}$$

that takes on the value of 0 if the noise is entirely unaffected by the time constant and 1 if it is entirely affected by the time constant and P is found using the methodology described in section 3.3.3. We use our data sets for the "big grid" and polarized beam map measurements described later in this work, and find median values of F of 0.37 and 0.20 respectively, which we use in the following simulations. Our simulation code is detailed in section 3.1.4, and we multiply the noise added before step 5 by F and that after step 5 by $1 - F$.

We run 20 realizations at each noise level, values of which are taken to be representative of the range we observe in our data, and find that increasing the noise level linearly increases the error on the mean of the recovery (Figure 3.15). In this case we define the noise not by the amount we input into the simulation but by the value of the standard deviation $\sigma_{\alpha-high}$ we observe on α_{high} after analysis. We do this because this value is our limiting factor in finding time constants; its signal to noise level is reduced by the time constant more than that of α_{low}. We also run realizations with no time constant, taken to be a baseline (black, Figure 3.15). We

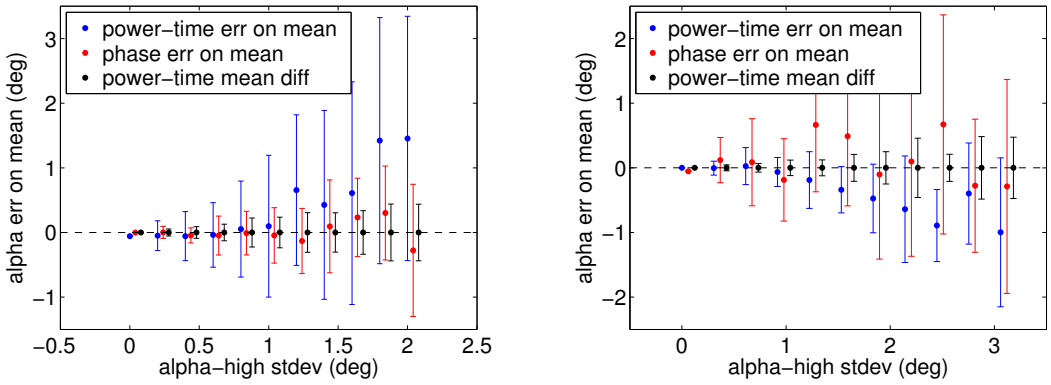

Figure 3.15: Recovery of α_{in} as a function of noise level in the case of "big grid" frequencies $f_{chop} = 3$ Hz and polarized beam frequencies $f_{chop} = 13$ Hz, for a simulated data set with $f_{3dB}$is 5 Hz and data analysis pipeline with time constant correction. We show the no time constant case in black, and the power and phase methods in blue and red. Each data point is the average of twenty simulations with 1σ error bars.

find that for a typical rolloff frequency of 5 Hz, the phase time constant removal method roughly doubles the error on the mean in the "big grid" configuration and is a factor of 2 – 4 larger in the polarized beam scan configuration. The power method shows a systematic effect at high noise levels in both configurations. It is possible this is due to the difficult nature defining how much power in our frequency band is noise at high noise levels; we consider that this method could be better optimized but focus our effort mostly on the phase method.

We fix the noise input and vary the frequency (Figure 3.16). We find that in the "big grid" configuration, the phase method shows 1-2 times the amount of error on the mean as the baseline and no discernible systematic error above 1 Hz. In the polarized beam configuration, both methods begin to see errors on the mean of a factor of 5-10 higher than the baseline once f_{3DB} gets below 4 Hz. This is because the polarized beam configuration has a value f_{high} of 21 Hz and suffers greater losses in signal to noise than in the big grid configuration.

Considering this information, we decide to make cuts of detectors with large values of $\sigma_{\alpha-high}$. The choice is a balance between reducing the overall error on the mean and losing many detectors, particularly slow ones. We decide to cut detectors with $\sigma_{\alpha-high} > 5°$for both tests, and detectors with time constants < 1.5 Hz for the polarized beam tests to avoid systematic errors.

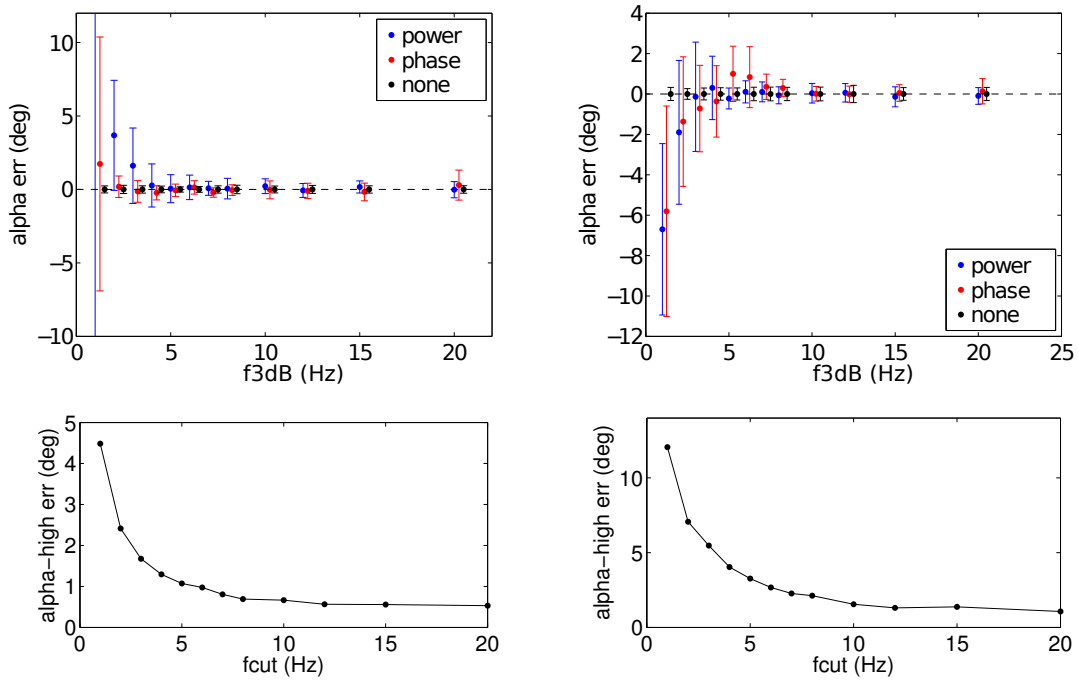

Figure 3.16: Recovery of α_{in} as a function of f_{3dB} in the case of "big grid" frequencies $f_{chop} =$ 3Hz (left) and polarized beam frequencies $f_{chop} = 13$Hz (right). We show the no time constant case in black, and the power and phase methods in blue and red. Noise level input is fixed, but effective noise level measured at f_{high}, shown as the standard deviation of α_{in} analyzed for the high sideband, is shown in the bottom two panels. Each data point is the average of twenty simulations with 1σ error bars.

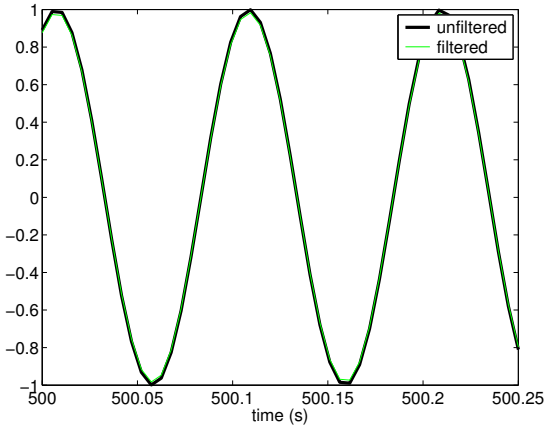

Figure 3.17: Typical application of a phase-preserving filter for chopped polarization data analysis. The signal to be filtered is 0.1 Hz below the filter center frequency of 10 Hz; total filter width is 0.5 Hz.

3.4 Use of filters in data analysis

Much of the data analysis that follows will make heavy use of bandpass filters to separate out various components of the chopped polarization signal. It is essential that these filters are phase-preserving, since polarization angle information – the signal that we are attempting to measure in most of the calibration tests detailed in Chapter 3 of this work – is encoded as the phase of specific components. We verify that filters are sufficiently phase-preserving for our use.

All filters used are implemented with the MATLAB FIR digital filter package, specifically using the function `fir1()`. This function creates a linear-phase digital filter. These filters are applied to our data using the `filtfilt()` function, which applies the filter in both forward and reverse directions, resulting in claimed "zero-phase distortion".

Filters used typically have a length of 2000, which is long enough to create sharp cutoffs but short enough to allow for reasonable code running times. Frequency components involved are well-understood and we have no reason to expect that a filter center would ever be more than 0.1 Hz from the signal being filtered. We create a sine-wave signal with a known phase and apply band-pass filters to it in several configurations; we fit a sine wave to the filtered signal to find its new phase and compare it to the unfiltered phase. Figure 3.17 shows the result of one such test.

Exploring phase space and tending towards worst-case scenarios (Table 3.2) reveals that the filters preserve phase well enough for their errors to play a small role in our calibration measurements.

test frequency (Hz)	filter width (Hz)	test phase (deg)	phase difference (deg)
9.9	0.5	0	-1.04×10^{-10}
9.9	0.5	63	0.0372
10	0.5	63	0.0238
10.2	0.5	63	0.0228
10.4	1.25	63	0.0162

Table 3.2: Verification of phase-preserving filters. Filter width is 10 Hz and filter length is 2000. The "phase difference" column shows the difference in the phase of the test signal before and after filtration.

3.5 Effects of HWP template signal and its removal

The description of the polarization data analysis pipeline in section 3.2 includes several filters whose purpose is not immediately obvious. In this section, we explain the necessity of these filters.

In section 3.1.3, it can be seen by following the mathematical steps to extract polarization signal from a chopped polarized source, the desired time-dependent polarization is shifted to DC and a small band around it. Thus, only one filter should be necessary, a low-pass run as the last step of the process. However, 3.1.3 does not take into account another effect, namely, HWP "template". This is a signal that appears at integer multiples of the HWP rotation frequency f_{HWP}, most notably at $2f_{HWP}$ and $4f_{HWP}$. The $2f_{HWP}$ signal can be due to any imperfection in or polarized emission from the HWP itself, which is then moved from f_{HWP} to $2f_{HWP}$ by the polarizing grid. The $4f_{HWP}$ signal is the result of any unchopped polarized light that enters the cryostat or is emitted from any optical element above the HWP. This template can be quite strong – for example, in the case of the Ebert-Fastie measurements it is typically about an order of magnitude above the chopped signal that we are investigating. As a result, power from it leaks into other frequencies during the multiplication steps described in 3.2. By initially filtering to remove everything but the chop frequency and the sidebands, systematic effects due to the template are prevented.

We use our simulation pipeline to demonstrate the necessity of filtering (or another template removal technique). In the simulation we inject sine wave signals at multiples of f_{HWP} (Figure 3.4, step 4). This yields angle-domain data shown in bottom panels of Figure 3.18. The analysis pipeline is then run on this simulated data. A "large template" and "small template" mode are used, with the former intended to reflect the case of the relatively low-signal Ebert-Fastie calibration tests, using a template the same size in amplitude of the input polarization signal at f_{chop} and the latter typical of a relatively high-signal calibration test such as a "big grid" setup, where the template is in some cases only 6% as large as the signal.

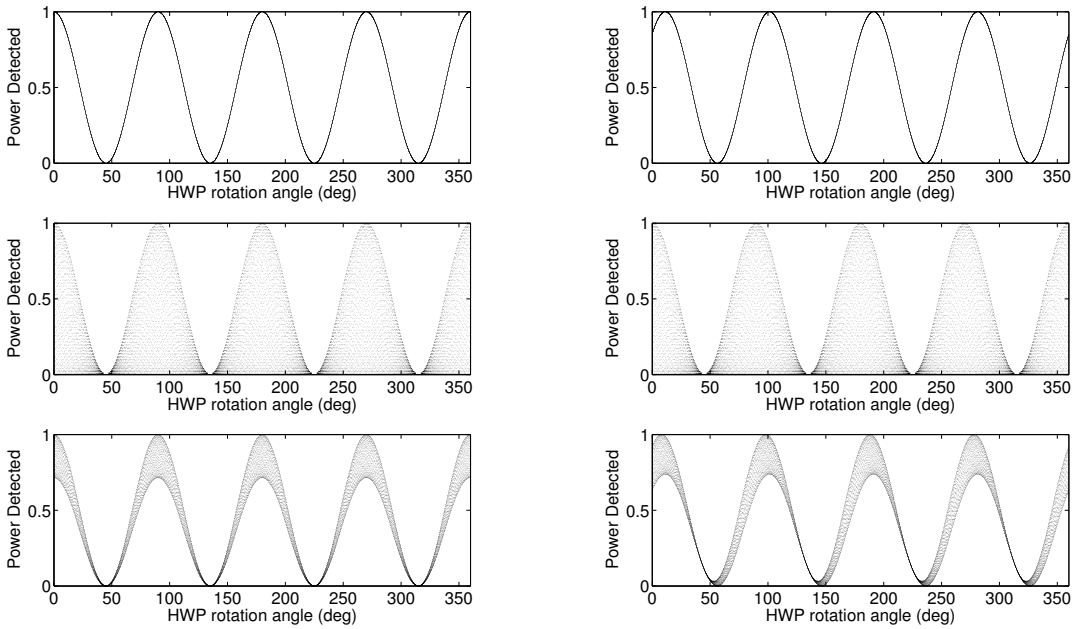

Figure 3.18: The template can be clearly seen by plotting detected power vs. HWP rotation angle θ_{HWP}. We use a zero-noise simulation. We plot the template only on the top panel, the no-template simulation in the middle, and the simulation with template on the bottom. Left: template phase is in phase with α_{in}. Right: template phase has been shifted by 22.5°.

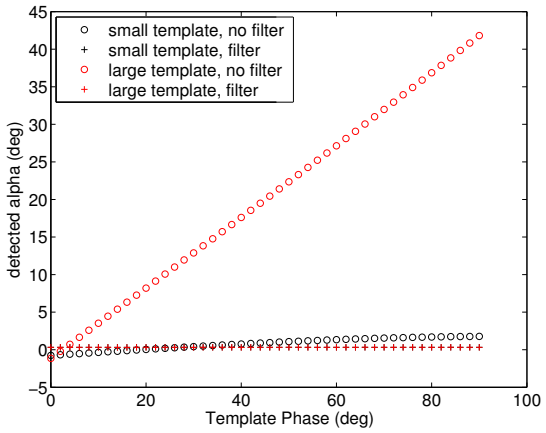

Figure 3.19: We run a simulation with a value of α_{in} of 0° and with a template sizes of 100% and 6% of the input polarization signal power. In the "no filter" case, we do not use the sideband bandpass filter (step [5] in Figure 3.7), which exists to remove the template. When the template is not removed, the measured value of α_{in} is systematically proportional to the phase of the template (the filter cases overlap).

The measured value of α_{in} should be 0° in the case of this simulation, and in particular, it should not be affected by the phase of the template. However, it can be seen in Figure 3.19 that when the template is not removed, the recovered value of α_{in} is partially a measure of the template phase instead of the actual signal. By removing the the template via bandpass filters early in the analysis process, this systematic effect is avoided.

An alternate method of handling template is available, and is used for EBEX LDB flight data. This method fits the template harmonics using sine waves in the HWP angle domain, and subtracts it. It is necessary for sky data where signal data is not as cleanly separated in frequency space from the template as in our chopped-source calibration measurements. While we find that this method is not well optimized for beam scans (see section 3.9.7), we do investigate using it in a stare configuration, specifically the "big grid" test; we find that we measure smaller standard deviations in measured angle α_{in} when using this technique but it does not reduce our overall error on the mean when evaluating real calibration data (section 3.8.5); with no notable reduction in error, we choose to focus mostly on the filtering technique for consistency between calibration tests.

3.6 Making absolute predictions of calibration results

In the following calibration tests, we want to know what value of the angle α_{in}we expect our analysis to report based on the geometry of the test and the instrument. Here we cover the process and data needed to make these predictions. Predictions specific to each calibration test are detailed in their respective sections.

3.6.1 Handling of time delays in readout systems

Because of differences in hardware and firmware versions, the dfMUX boards that are configured for HWP readout have a time delay relative to those configured for bolometer readout. Specifically, the digital FIR filtering which reduces the original sample rate of 25 MHz to the sample rate that is ultimately written to disk shifts the signal backwards in time. On the bolometer-configured boards, a newer firmware version automatically undoes this effect. The time shift of the HWP boards relative to the bolometers is of particular importance since the HWP rotates a full degree in just 1.4 ms. Analysis of the firmware sets this value at 10.69 ms, or 7.7° for 2 Hz HWP rotation.

150 GHz	6.6°
250 GHz	21.8°
410 GHz	5.8°

Table 3.3: Offsets between marked HWP axis and effective axes in each band in units of polarization angle (these units are larger by a factor of two than those show in Figure 3.20).

3.6.2 Frequency dependent polarization rotation prediction and marking of HWP axes

A five-HWP stack designed for broad-band use such as the one in EBEX has a unique phase delay – that is, the HWP rotation angle that coincides with the peak of the IVA curve – at every frequency. Since EBEX is a multi-color instrument operating at three frequency bands, each with a non-negligible width, we expect to see an absolute rotation between the three frequencies as well as a relative rotation across each band.

A measurement was taken of the the HWP alone at room temperature using a Fourier Transform Spectrometer (FTS) using the methodology described in [32]. The results of the data analysis are shown in Figure 3.20 (black curve). The light red and blue curves ("complex model") are models based on the best-fit parameters extracted from the FTS measurement. The thick curves ("simple model") are a model based only on the known or physically measured values in the table below the figure. We find that the two models agree well, but both deviate from the directly measured curve.

To predict the absolute rotation angles we expect to observe during calibration tests, we must measure the HWP extraordinary or ordinary axis at a known frequency relative to the "zero" slot on our HWP encoder. During the HWP FTS measurement, a mark (three black arrows in Figure 3.21) was made on the wave plate at the maximum of the IVA curve in the case where all frequencies from 0-600 GHz were allowed to pass through the FTS. Assuming a constant frequency response of the FTS and a black-body source, we use the simple model to calculate the effective phase angle of this configuration as it would be observed on the y-axis of the figure. The difference between this value and the blue (cold) curve at each frequency (Table 3.3) sets our effective axes, which are multiplied by 2 to convert from HWP angle to polarization angle units, and which we use in the next section (3.6.3) in the "achromatic effects" part of our absolute prediction. Because the model deviates from the FTS data, there is a large error on our ability to calculate these effective axes. We estimate the error in absolute offset of the numbers in Table 3.3 is on the order of 5°; this value dominates our ability to match our absolute calibration with a predicted value in section 3.12.1.

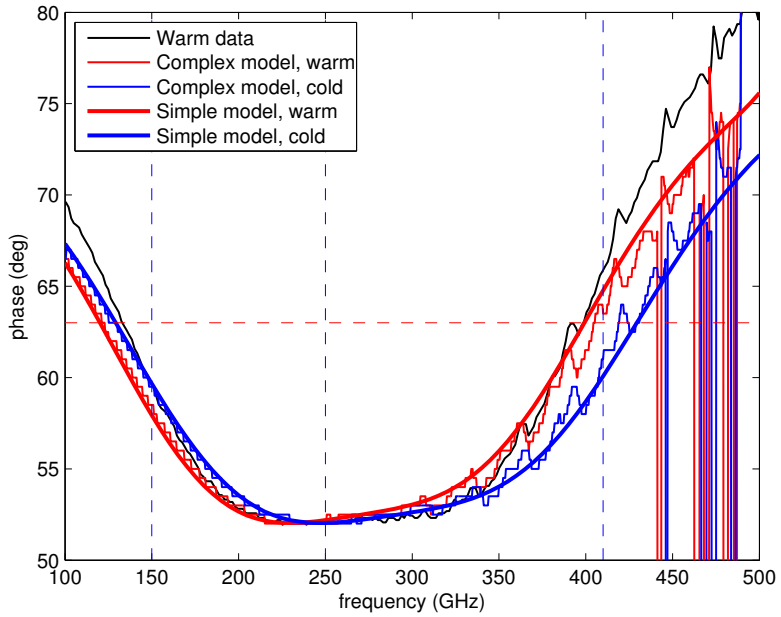

parameter	value	units
index, ordinary, 300 K (n_o)	3.068	
index, extraordinary, 300 K (n_e)	3.048	
index, ordinary, 4 K (n_o)	3.356	
index, extraordinary, 4 K (n_e)	3.048	
plate thickness (d)	1.665, 1.667, 1.648, 1.675, 1.640	mm
relative plate angles	0, 26.5, 94.8, 28.1, -2.6	°

Figure 3.20: Phase delay vs. frequency of EBEX five-stack HWP. Black curve is data measured by an FTS at room temperature. Red and blue curves are 300 K and 4 K models. The red dashed line shows the effective phase in the configuration where the HWP was marked; blue dashes show band centers. The adjustments used in section 3.6 is the differences between the red dashed line and the 4 K simple model shown in Table 3.3.

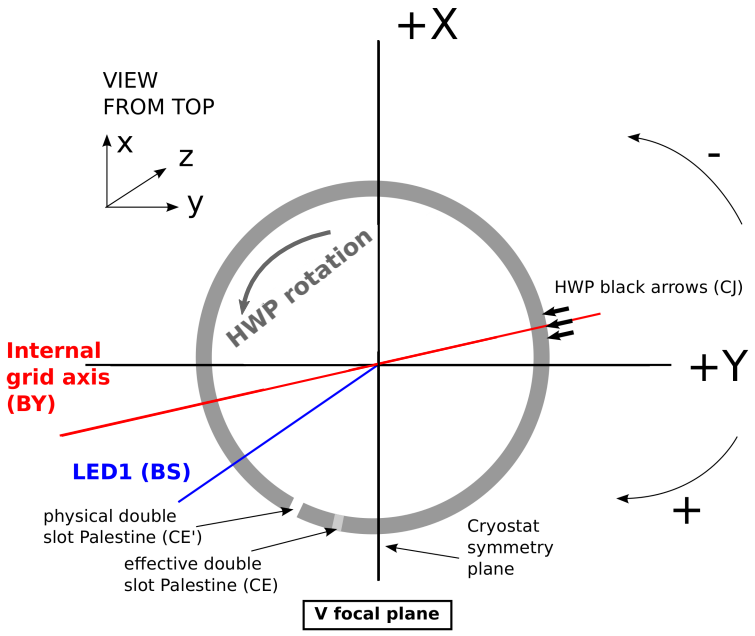

Figure 3.21: Diagram of calculation of absolute angle prediction

3.6.3 Conversion from observed polarization angle to physical incident polarization angle

3.6.3.1 Cryostat geometry

We choose to approach the absolute polarization calibration question by seeking the angle we expect from our analysis output given a known incident polarization in our cryostat coordinate system.

We define the cryostat coordinate system as having an x-axis parallel to the symmetry plane of the cryostat with a positive sign indicating a clockwise rotation when the system is viewed from the sky side. We note this system is reversed vertically from the system in Figure 3.1. Our analysis code is consistent with Figure 3.1 and the model discussed in section 3.1.2; when we finish our analysis, we multiply the output by -1 to compare it to our physical system and prediction.

We begin the process of forming a prediction by looking at the geometry of our system. The following angles were measured during cryostat assembly with a digital Coordinate Measuring Machine (CMM). Each number is the sum of several transformations. We consider the following angles, illustrated in Figure 3.21:

1. The orientation of the internal grid: $-6.7°$

1	A	LED in cryostat coordinate system	-125.4°
2	B	EBEX grid in cryostat coordinate system	83.2°
3	C	HWP mark to double-wide slot	128.8°
4	D	time delay (HWP is ahead by)	-7.70°

Table 3.4: Summary of geometry that sets the HWP offset

2. The orientation of the LED/photo diode combination that reads out HWP angle: $-125.4°$

3. The location of the double-wide "zero" slot relative to a mark on the HWP. Our HWP angle code considers the center of this slot zero. The mark on the HWP is an approximate 150 GHz axis; we discuss an adjustment to account for this approximation later.

4. The HWP angle adjustment due to timing delay discussed in section 3.6.1: the HWP is ahead of the bolometers by 10.69 ms $\rightarrow$7.70°@ 2 Hz; analysis is done in the bolometer time base.

5. The direction of HWP rotation, counter-clockwise as viewed from the top (-$\hat{z}$ in the physical coordinate system, but +$\hat{z}$ in the model system).

Table 3.4 summarizes these values in the case of the our Palestine 2012 calibration setup. We then pedagogically align the HWP axis with the internal grid axis, a configuration that would result in a measured polarization angle α_{in} of 0° in the configuration shown in Figure 3.21. We find the "HWP offset" θ_{offset} which we define as the angle value reported by our readout and angle-decoding system when the (approximate) HWP axis is aligned with the grid, a configuration which would be 0° in our model system.

$$\theta_{offset} = 360 - (B + C - A + D) \tag{3.39}$$

In the Palestine 2012 calibration,

$$\theta_{offset} = 30.6°$$

3.6.3.2 Conversion of offset in HWP angle to offset in measured polarization

We evaluate how this value will affect the polarization angle α_{in} that we measure. We consider our demodulation of Q and U, this time with an offset added to the HWP angle θ:

$$\begin{aligned} Q(t) &= I_{out}(t) \times \cos(\omega_{chop} t) \times \cos(4\theta_{HWP}(t)) \\ &= \frac{I_0 P_{in}}{16} \cos(4\theta_{HWP}(t) - 2\alpha_{in} + 4\theta_{offset}) \cos(4\theta_{HWP}(t)) \end{aligned}$$

$$\begin{aligned} U(t) &= I_{out}(t) \times \cos(\omega_{chop} t) \times \sin(4\theta_{HWP}(t)) \\ &= \frac{I_0 P_{in}}{16} \cos(4\theta_{HWP}(t) - 2\alpha_{in} + 4\theta_{offset}) \sin(\theta_{HWP}(t)) \end{aligned} \tag{3.40}$$

Evaluating, we find that

$$Q = \cos(-2\alpha_{in} + 4\theta_{offset})$$

$$U = -\sin(-2\alpha_{in} + 4\theta_{offset})$$

$$\frac{U}{Q} = \tan(2\alpha_{in} - 4\theta_{offset})$$

and that we measured the angle $\alpha_{in-reported}$

$$2\alpha_{in} - 4\theta_{offset} = \arctan\frac{U}{Q} = 2\alpha_{in-reported}$$

such that

$$\alpha_{in-reported} = \alpha_{in} - 2\theta_{offset} \tag{3.41}$$

We apply the coordinate system sign flip discussed earlier in this section:

$$\alpha_{in-reported} = -\alpha_{in} + 2\theta_{offset} \tag{3.42}$$

As previously mentioned, we flip the sign on our reported value of α_{in} after the analysis to put it in terms of our physical coordinate system. We also find that the offset in α_{in} due to the offset in θ is

$$\alpha_{offset} = 2\theta_{offset}$$

3.6.3.3 Non-geometry instrument effects

In finding our predicted polarization value, we consider two other effects. One is the offset between our marked HWP axis and the effective axes in each band which we discussed in section 3.6.2. The second is a bias found from our time constant removal technique, discussed in detail in section 3.11.3.

"big grid", orientation 1, 150 GHz	-83.7°
"big grid", orientation 1, 250 GHz	-70.7°
"big grid", orientation 1, 410 GHz	-86.3°
polarized beam maps, 150 GHz	-22.7°
polarized beam maps, 250 GHz	-4.0°
polarized beam maps, 410 GHz	-21.5°

Table 3.5: Expected values of observed polarization in two calibration tests

3.6.3.4 Calibration input polarization

We obtain an absolute measurement of the input polarization α_{in} in our cryostat coordinate system for two of our calibration tests: the broad-band, cryostat only test (the "big grid" test), and our polarized beam scan test.

In the former case, we polarize the light coming into the cryostat by placing a grid on top of the cryostat window. We measure this grid and reference it to our cryostat coordinate system with a CMM in the same manner as we made the measurements of the cryostat geometry (section 3.6.3.1). More information can be found in section 3.8. We find the input polarization of this configuration is 25.3° in the original orientation.

In the case of polarized beam scans, we measure the orientation of the cryostat and the source with inclinometers, the process for which is detailed in section 3.9.2. Our cryostat inclinometer is aligned to our cryostat coordinate system within 0.1°, and this coordinate system is aligned approximately parallel to the gravity vector $\vec{g}$. The source was aligned approximately perpendicular to $\vec{g}$. Using these measurements, we adjust our observed angles ($\alpha_{in-reported}$) such that the effective input polarization is 90°. Measurements of θ_{offset} and input polarization are entirely geometric and repeatable to better than 0.1°.

3.6.3.5 Calculation of expected instrument output and calibration

We can now calculate the value of the polarization we expect to measure in the calibration tests detailed in later sections of this work. We use the following equation:

$$\alpha_{expected} = 2\theta_{offset} + \alpha_{in} + \alpha_{achromatic} + \alpha_{bias}$$

Alternately, we can define a calibration: the angle our instrument measures at the focal plane center when the input polarization is 0° with respect to our cryostat system. We obtain this value by subtracting the input polarization angle α_{in} from the observed angle $\alpha_{observed}$, after adjusting the observed angle to account for the time constant bias α_{bias} (section 3.11.3) and an adjustment to account for the fact that our narrow-band source was not always set exactly at

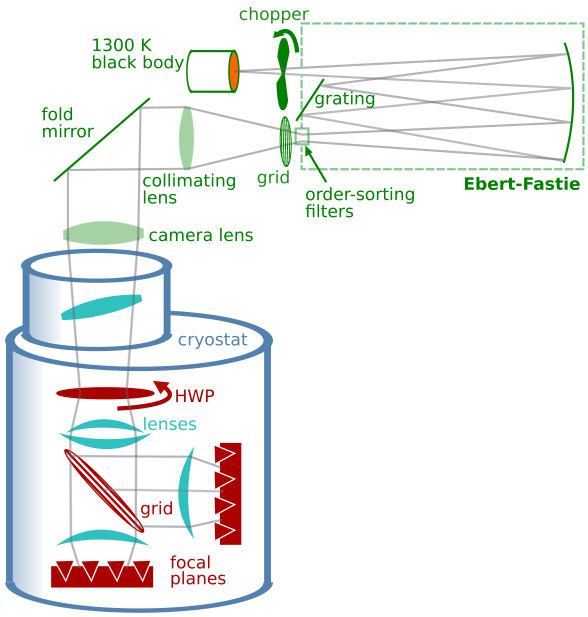

Figure 3.22: Setup of frequency dependent polarization rotation calibration measurement. Cryostat is shown in blue with optics in maroon and cyan; calibration setup is shown in green.

our band center. We use both techniques in our summary absolute calibration section 3.12.1 at the conclusion of this work.

3.7 Frequency dependent polarization rotation

We seek to experimentally verify the curve introduced in section 3.6.2 with the EBEX cryostat (Figure 3.20). We expect to see a variation in recovered angle α_{in} due to an expected variation in HWP phase delay as a function of the frequency of the incident light; this is a consequence of the use of a broad-band 5-stack HWP. In this section, we discuss only the relative shape of the curve; the absolute values on the y-axis have no physical meaning. We establish that calibration in later sections.

3.7.1 Experimental setup

We measure frequency dependent polarization rotation using an Ebert-Fastie monochrometer ([34, 33]). This data was taken in conjunction with spectral response measurements. The Ebert-Fastie takes as an input a 1300 K broad-band block body source and outputs light at a single

Figure 3.23: Photograph of Ebert-Fastie monochrometer being used to measure frequency dependent polarization rotation

frequency band, the bandwidth of which is made small compared to the designed band sizes of EBEX via order-sorting filters at the Ebert-Fastie exit aperture. The frequency output bandwidths are ±0.4, 0.7, and 1.0 GHz for the 150, 250 and 410 GHz bands respectively. The frequency center of the output is controlled by varying the diffraction grating angle, which is controlled by a stepper motor and an automated software scan program. The program will scan in frequency across a band given a set of desired frequencies and integration times. Only one detector can be measured at a time, though an automated x-y mounting stage for the Ebert-Fastie facilitates easy transitions between detectors.

The Ebert-Fastie is coupled to the EBEX cryostat via two lenses and a mirror (Figure 3.22). The signal is passed through a polarizing grid and mechanically chopped. Due to the relatively small signal strength observed in this setup, we eventually used a stepper motor to operate the chopper blade to achieve perfect frequency stability. Bolometer and HWP angular position data was taken while the Ebert-Fastie completed a scan. The frequency output of the Ebert-Fastie was also automatically recorded in an EBEX dirfile channel. This data was analyzed using the pipeline described in section 3.2 with the optimizations described in the following section (3.7.2).

3.7.2 Optimization of filter width and sideband choice for Ebert-Fastie analysis

The analysis pipeline outlined in the previous section relies on appropriate choices for several parameters. Most notable is the width of the bandpass filters that are used to select various

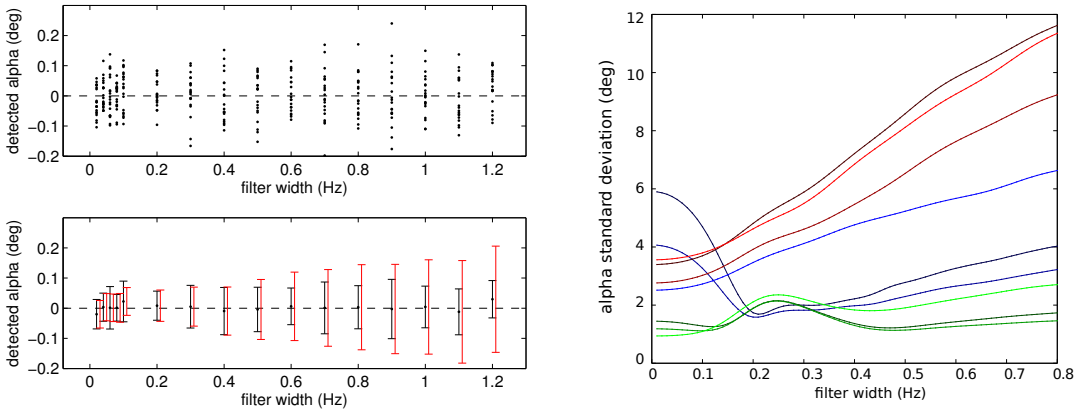

Figure 3.24: Left: Optimization of bandpass filter width. Left, top: detected α_{in} for twenty realizations at each filter width. Left, bottom, black: Standard deviation error bars of each set of realizations. Left, bottom, red: average of standard deviation error within each realization divided by ten. Right: standard deviation in α_{in} for 250 s of data as a function of filter width for three real detectors. 150 GHz is blue, 250 GHz green, and 410 GHz red; the lightest shade is high sideband only, darkest shade low sideband only, middle shade both sidebands.

frequencies from the time stream, and the final low pass filter in the analysis pipeline (see Figure3.7). We use a combination of our simulation and real data to decide on values for these parameters.

Filter width must be large enough that the filter edges do not interfere with the signals and cause spurious effects, but narrow enough that all frequencies but the chosen one are fully excluded. We use our simulation (section 3.1.4) in conjunction with our data analysis pipeline (section 3.2) to explore this filter width. We vary the width of all filters – that is, the bandpass filters at f_{chop} and $f_{sidebands}$ (Figure 3.7 items [4] and [5]) and the final low pass filter (Figure 3.7 item [15]). A value of $\alpha_{in} = 0$ degrees was used as the input to the simulation. We create twenty realizations each for a range of filter widths from 0.1 Hz to 1.2 Hz; after analysis each realization has a single mean observed α_{in}, but since we take 250 s of data and we obtain a unique result for every time sample, each realization also has its own standard deviation.

Figure 3.24 shows the result of this analysis. The top panel shows detected value of α_{in} from the analysis process for each of the twenty realizations for each filter width. The bottom panel contains one standard deviation error bars for the means of each set of realizations in black. Shown in red is the average of the one standard deviation errors for each realization, reduced by a factor of ten. These errors increase for increasing filter size, even though the analysis returns as accurate a result.

The simulation tells us little about how to set our filter widths; since it assumes the signal is perfectly constrained to its frequency, the indication is either that we should make the filter width as small as possible as to minimize the observed standard deviation, or that any width is appropriate since we get the same error on the mean regardless (Figure 3.24, left). We thus turn to a real data set and optimize the width by choosing that which minimizes the observed standard deviation.

We analyze a segment of data in the middle of the scan for three real detector data sets. The observed standard deviation in α_{in} as a function of filter width for a detector at each wafer frequency detectors is shown in Figure 3.24. No single value for filter width is the best for all detectors; we see 0.2 Hz is the value that produces the lowest noise overall. Additionally, we find no major difference between using only the lower sideband or using both (recalling that both sideband peaks contain polarization signal but the higher is rolled off by the detector time constant); we choose the lower only. These observations set the values of the analysis parameters used in the Ebert-Fastie calibration analysis.

3.7.3 Results and comparison to prediction

We obtain analyzable data from 7 150 GHz detectors, 4 250 GHz detectors, and 2 410 GHz detectors. An example of each is shown in Figure 3.25. In each case, the top panel shows the reconstructed angle α_{in} for every bolometer data point (191 Hz) during the Ebert-Fastie scan, frequencies of which are shown in the middle panels. As the scan leaves our bands, noise increases until no signal remains. We bin the data in the bottom panels, and show standard deviation error bars. These plots are meant to show the shape of the spectra and the absolute value of the angle here (y-axis on the top and bottom panels) does not have a physical meaning.

We compare these results to the model described in section 3.6.2 (Figure 3.26). We originally did not set out to compare separate scans to each other; however, we position the 250 and 410 bands vertically by using noted information regarding the position of the polarizing grid on the E-F exit aperture. This information was not recorded reliably for the 150s, but we find alignment of 150s to 250s is possible using polarization modulation efficiency data taken with the Ebert-Fastie setup [34]. It is not possible to use a similar method as a consistency check for the 250 to 410 alignment, since the PME test data suggests an alignment that is not well-motivated by our models; we assume an unintentional rotation of the HWP occurred during this measurement but have no way to verify this assumption. We also take into account the unexpected cryostat-only azimuthal rotation measured in the "big grid" test (Section 3.8.3). Because of these caveats, we do not use E-F data for absolute band-to-band calibration, but we find it instructive to consider the overall fit to the model; we find consistency between the model and the Ebert-Fastie data, and do not find significant differences between detectors of the same frequency.

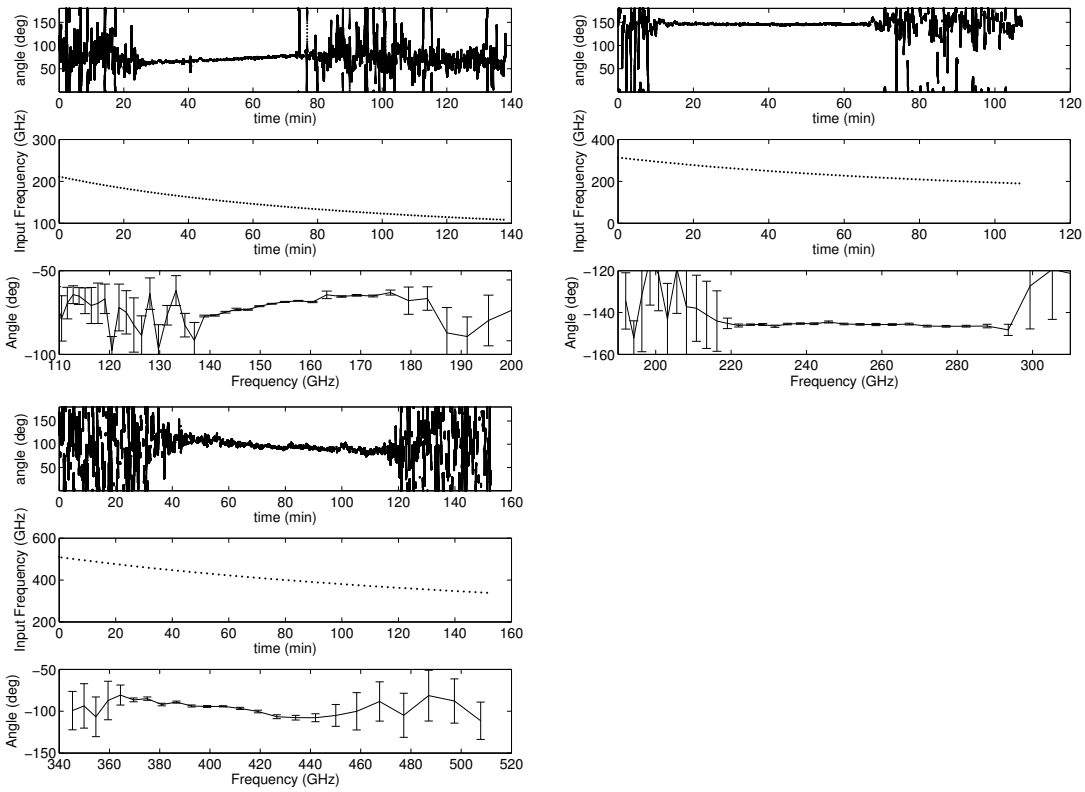

Figure 3.25: Ebert-Fastie results for one detector from each frequency; Upper-left: 150 GHz; upper-right: 250 GHz; lower-left: 410 GHz. For each, the top panel is raw detection of α_{in} as a function of time; middle panel is the input frequency as a function of time; bottom panel is binned α_{in} as a function of input frequency.

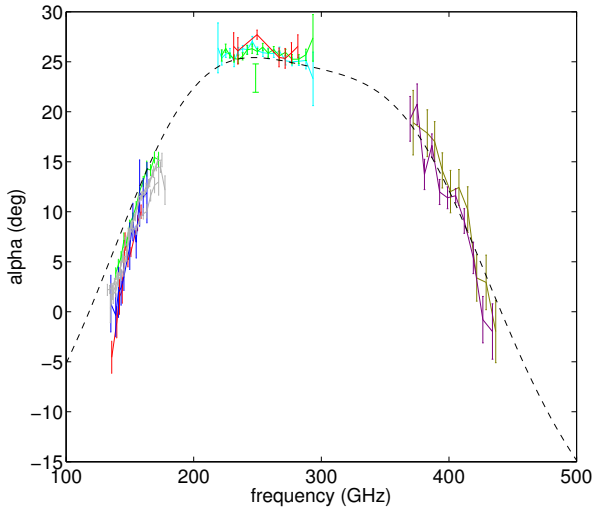

Figure 3.26: EBEX band spectra measured in the Ebert-Fastie setup compared to model. Gray curves have no absolute angle information and are adjusted to match those which do. All other curves are positioned absolutely with respect to each other based on known input polarizations for each curve. Error bars are 1σ of the measured values of α_{in} for each input frequency. The dashed line shows the cold-temperature model discussed in section 3.6.2, which is adjusted vertically to best fit the data.

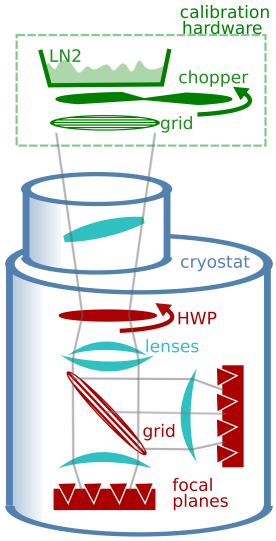

Figure 3.27: Setup of calibration test with fixed polarization signal incident on all detectors simultaneously, with cryostat shown in blue and calibration hardware in green.

3.8 EBEX cryostat with fixed polarization signal incident on all detectors simultaneously

We investigate what polarization angle various EBEX detectors report when exposed a single polarized source simultaneously. The measured polarization angle may vary due to different detector time constants, or unexpected optical effects. We created a calibration test that would expose all detectors to light with the same incident polarization angle simultaneously, taking the cryostat alone without any mirror optics or scanning.

3.8.1 Experimental setup

With the EBEX cryostat mounted in position on the gondola, we placed a large grid – the spare for the grid inside of the cryostat – on the cryostat window and its position measured relative to known cryostat coordinates; this grid covered the window entirely although a small gap of approximately 1/2" was left between the grid and the window frame (we will sometimes refer to this as the "big grid" test for brevity). A LN2-filled cooler was placed above the window in such a position as to fill the majority of the beam. A suitably large chopper wheel was installed below the cooler so the blade covered the bottom of the cooler (Figure 3.27). The chopper wheel was turned on to a set frequency f_{chop} of 3 Hz and 5 Hz and the HWP rotated continuously at a frequency of $f_{HWP} = 2$ Hz.

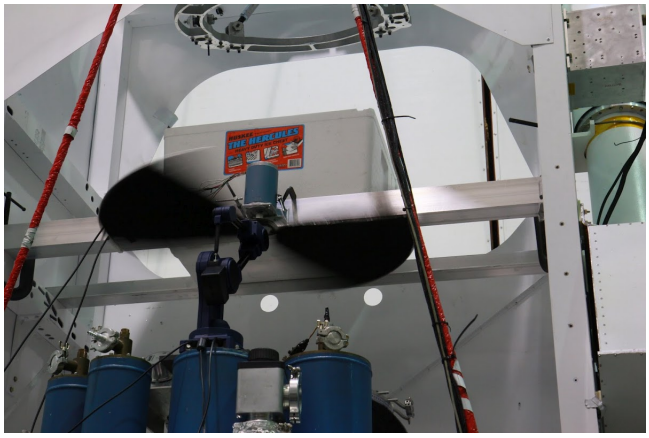

Figure 3.28: Photograph of setup of calibration test with signal incident on all detectors simultaneously

We measure the position of the window grid with a CMM and reference it to our base cryostat coordinate system to obtain overall calibration. Additionally, we can use the results of 3.6.3 to predict the value of the polarization angle $\alpha_{observed}$ that should be produced by our analysis given the information we know about the physical orientation of the source; we compare the absolute calibration of all tests in section 3.12.1.

Bolometer and HWP angular position data was taken for several hours at two different grid angular positions (Figure 3.29). With the external grid in its initial position, about two hours of data was taken. The grid was then rotated and its new position measured. After 15 minutes of data, the chop frequency f_{chop} was increased from 3 Hz to 5 Hz, and then reduced back to 3 Hz 25 minutes later. Another two hours of data was taken in this final configuration, though the bolometers began to warm slowing during the last hour due to an expired fridge. The data was analyzed using the established chopped polarization data analysis pipeline (section 3.2) in segments over the entire course of the calibration measurement, with separate time constant removal for each section. We use the filter widths from the optimization process discussed in the next section.

Some detectors show some variation in amplitude and DC offset. We find this is likely a consequence of varying and relatively high wafer temperatures, and investigate the effect further in section 3.11.1.

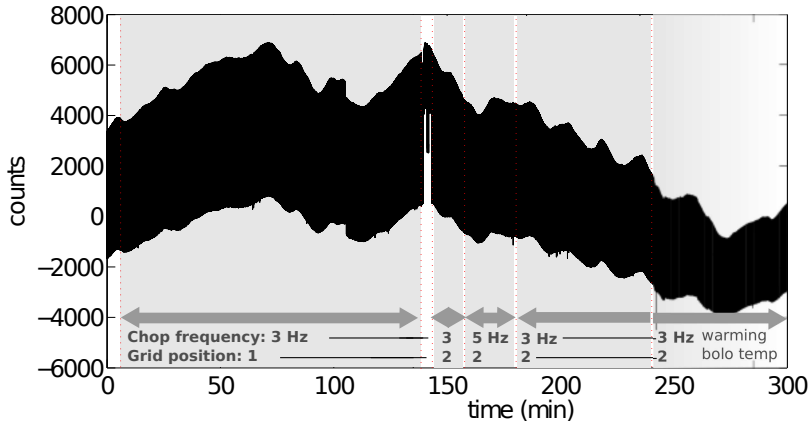

Figure 3.29: A typical raw time series from one detector over the course of the "big grid" calibration, showing different chop frequencies and grid positions.

3.8.2 Optimization of filter width, sideband choice, and handling of missing data

We optimize various parameters in the analysis process before proceeding. We choose a random sample of 12 detectors and analyze a 250 s segment with varying filter widths (we refer the two bandpass and final low pass filters detailed in section 3.2) and we make all three the same total width (3dB points low to high for the bandpass and 0 Hz to the 3dB point for the low pass) . The same process is done with a simulation. For each 250 sample, we take a standard deviation of measured α_{in} (Figure 3.30, left). It is clear that at very narrow filter widths, some of the signal is cut and higher errors are realized; at very large filter widths, unnecessary noise is allowed to remain. This sample of detectors, and the simulation, suggest that a filter width in the range of 0.4 – 0.8 degrees is reasonable.

However, measuring α_{in} for the entire data set indicates that the reported standard deviation is not a good indicator of optimization in the case of filter width. In the right panel of Figure 3.30, we show the measured α_{in} for all detectors for a single 250 s segment in time, adjusting for focal plane position and wafer frequency (see full analysis in section 3.2), for three different filter widths. We also take a standard deviation of α_{in} for each detector's data points. Despite that for each filter width the average standard deviation measured for each detector is less than 2.5° (Table 3.6), we find that our error on the mean blows up quickly for filter sizes $> 0.4°$. An investigation of detectors highly sensitive to this filter size reveals large template signals at $2f_{HWP}$. We take 0.4° as our optimized filter size for the rest of this measurement.

We evaluate all detectors using the configurations of low sideband, both sidebands, and high sideband for the analysis (Figure 3.31, right). We find that using either only the low sideband or

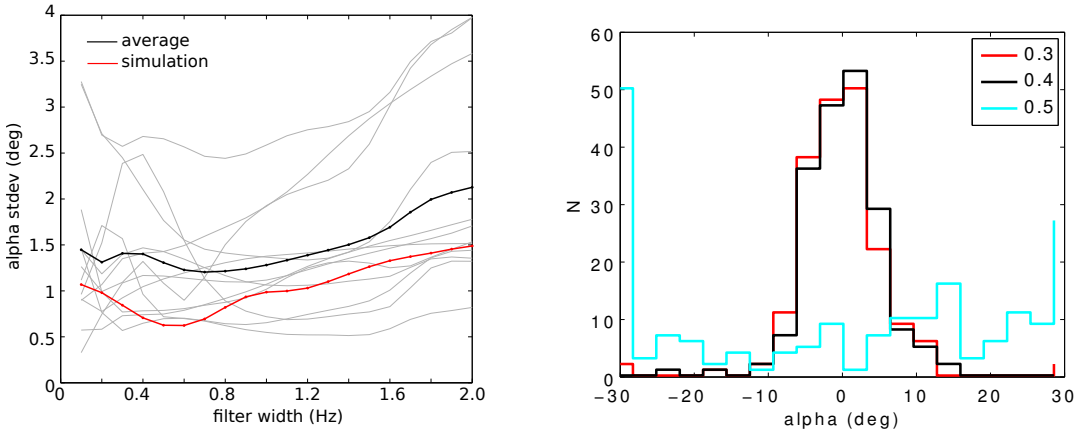

Figure 3.30: Left: 1σ standard deviations in measured value of α_{in} for a dozen real detectors (gray) and a simulation (red) from the stare calibration setup analyzed with different filter widths. Right: difference observed from the average detected value of α_{in} for all detectors in the stare calibration setup, using three different filter widths of 0.3°, 0.4°and 0.5°

both sidebands gives equivalent results, while using the higher sideband results in an increased noise level. This is expected due to the lower amount of power present in the higher sideband due to the detector optical time constant. We opt to use the low sideband only.

3.8.3 Results and comparison to prediction

The analysis produces values α_{low} and α_{high} for the low and high sidebands respectively for all bolometer data points, that is, at 191 Hz. For each segment of 250 s in length values of α_{in} and f_{3dB} are calculated by using the phase RC removal process detailed in section 3.3.4.

We show results of two detectors in Figure 3.32. The top panel of each figure shows a raw

filter width (Hz)	error on mean (°)	mean std. dev.(°)
0.2	7.41	2.90
0.3	10.15	2.87
0.35	11.77	2.24
0.4	4.94	1.08
0.45	31.75	1.11
0.5	33.86	0.86
0.8	53.38	0.76

Table 3.6: Optimization of filter size for the "big grid calibration" measurement. Error on mean is the standard deviation of the observed input polarization value α_{in} for all detectors; mean std. dev. indicates the average of the all standard deviations for each detector individually.

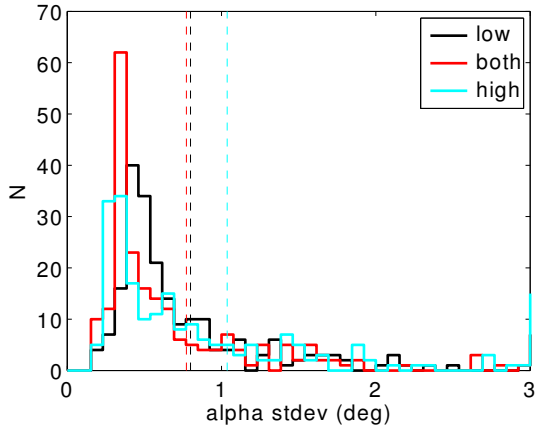

Figure 3.31: Standard deviations in α_{in} for all detectors in the stare calibration setup, using the lower, higher, and both sideband peaks for analysis.

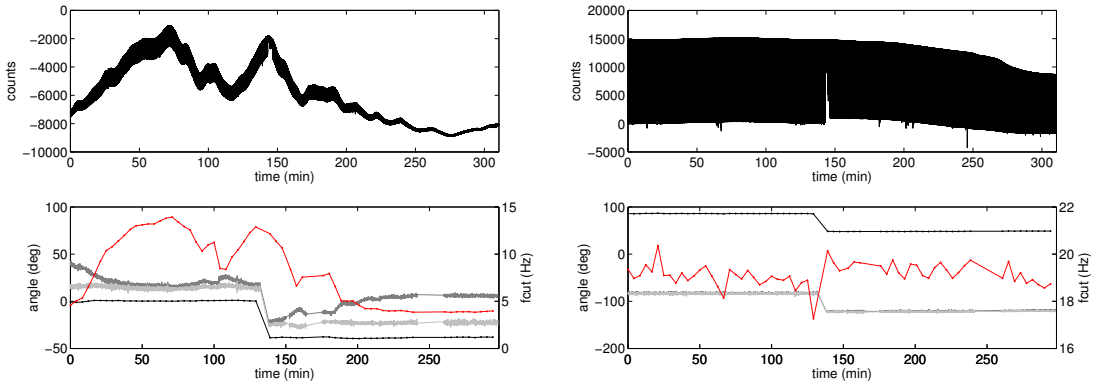

Figure 3.32: Results from two detectors over the duration of the calibration measurement. The top panels show the raw detector time streams. The bottom panel shows detected polarization for lower and upper sidebands in dark and light gray. The black line is the calculated value of $\alpha_{observed}$, with time constant correction, calculated in 250 s segments. The red line is the bolometer time constant (right ordinate).

time stream over the course of the entire calibration measurement. The bottom panel shows in dark gray and light gray the detected angle for every bolometer data point using each the lower and upper sidebands respectively. As described in section 3.3.2, these angles are not the same due to the detector time constant. For each 250 s segment, we use the process described in section 3.2 to back out the angle with time constant effects removed (black) and the time constant itself (red).

The detector on the left is on focal plane V and is subject to changes in wafer temperature, discussed in more detail in section 3.11.1. The time constant changes over the course of the test and is clearly correlated to the DC level, peak to peak level, and temperature. However, after the time constant removal process, the recovered angle α_{in} (black) is quite stable. The transition that occurs at t=200 min is expected and is the result of a change in the source.

The detector on the right is on focal plane H and is not subject to warm wafer temperatures. Consequently it exhibits both a stable time constant and a stable recovered value of α_{in}.

Those detectors not subject to the cuts in the next section can be compared to each other with a plot showing their measured polarization immediately before and immediately after the rotation of incident polarization that occurs at t=200 min.

In Figure 3.33, the left-hand panels compare the polarization measured before and after the change in incident polarization occurs. The right-hand panels plot the two measured polarizations against each other. All detectors that showed any signal (S:N ¿ 5, where signal is taken as the mean of a 0.5 Hz band around f_{chop} in the frequency domain, and noise the mean 0.3 Hz bands on either side of that) are shown in black; red detectors are those that survive the cuts. Black dotted lines show the average measured values, and red dotted lines show the expected values based on knowledge of the geometry of the change in grid position discussed in section 3.8.1.

In figure 3.34, we collect the differences between the two grid positions for each frequency. We see an agreement between detectors with a one-sigma standard deviation of 1.88°, but also a systematic error in our ability to capture this relative rotation by 1.75°.

The applied cuts are very effective at eliminating detectors that are clearly outliers. However, there is still significant deviation in the absolute angles measured by the various detectors; in particular we see two populations in the 250 GHz detectors. This is a consequence of the detectors' position on the focal plane, and the observation that the measured polarization varies linearly across the focal plane in azimuth.

In Figure 3.35 we show the measured polarization for each detector against each detector's position on the focal plane. The difference between the points that are not corrected for time constant (black) and those that are (red) makes clear the importance of making this correction. A clear linear pattern is seen as we move across the focal plane, so we make a linear fit. The

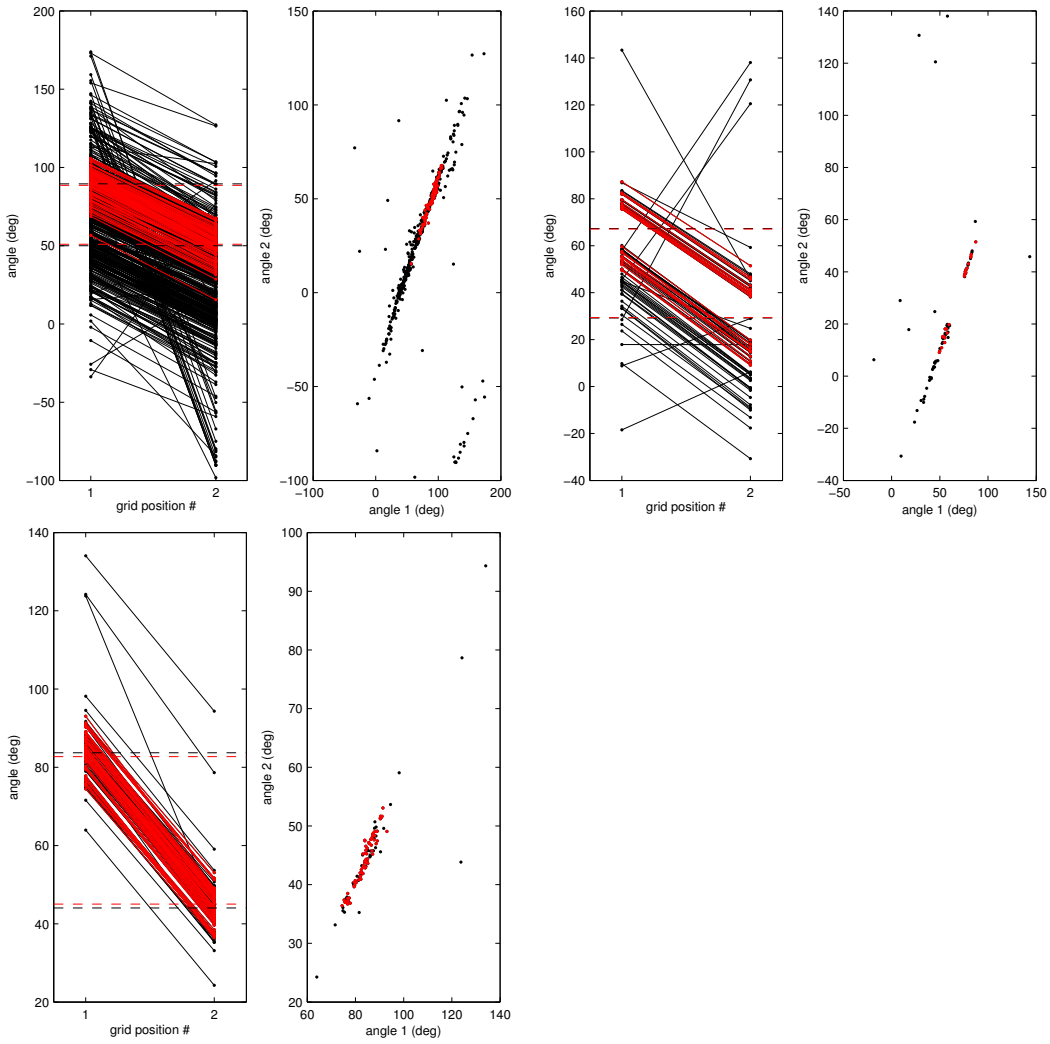

Figure 3.33: Plots for each of the detector frequencies 150 GHz, 250 GHz, and 410 GHz showing the value of the measured polarization before and after a change in the source polarization (left) and before vs. after the change (right). Averages are shown in dashed lines; detectors passing the final data cut (section 3.8.4) are shown in red.

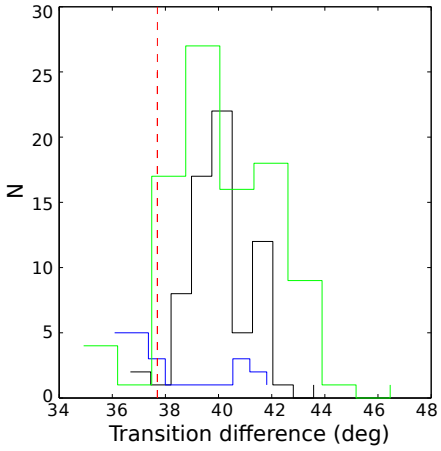

Figure 3.34: Difference between measured polarization for two external grid positions that differ by 37.7°. 410 GHz is shown in black, 250 GHz in blue and 150 GHz in green. The expected value is indicated by the dashed red line.

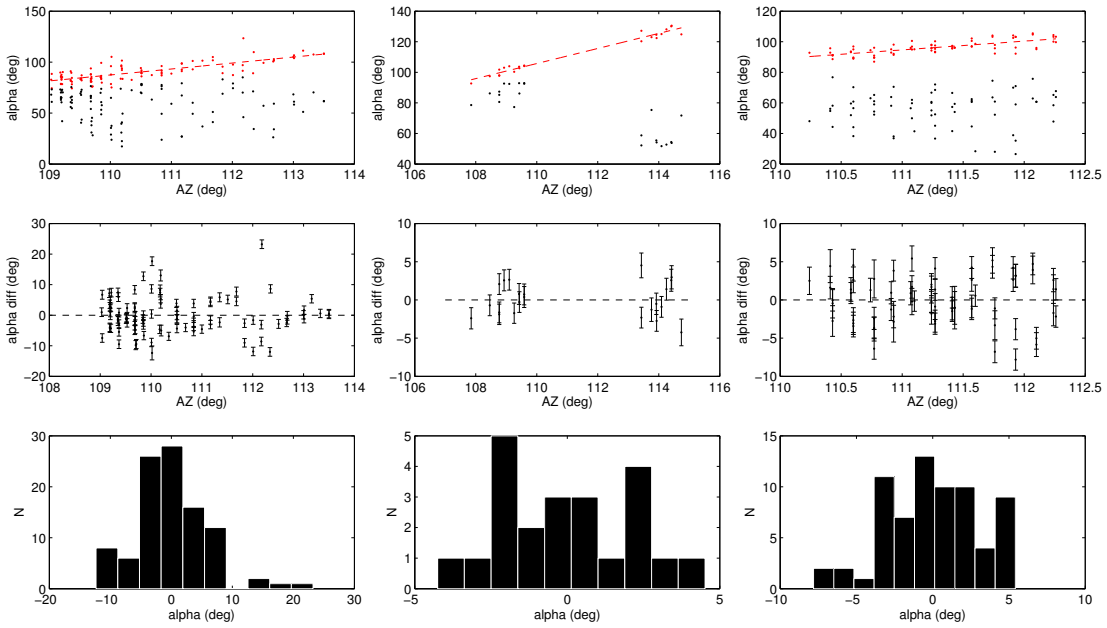

Figure 3.35: Plots for each of the detector frequencies 150 GHz (top, left), 250 GHz (top, right), and 410 GHz (bottom) showing the polarization measurement α_{in} for each detector vs. the detector's position on the focal plane in azimuth. Top panels shows measurements corrected for time constant in red with a linear fit and uncorrected points in black. Middle panels show differentials from the fit with error bars showing the standard deviation of the measurement over the entirety of the test. Bottom panels are histograms of the differentials from the fit.

	α_{in}	α_{in} stdev	slope (alpha/az)
150	-82.0°	6.0°	5.9
250	-65.3°	2.2°	4.9
410	-80.6°	3.1°	5.7

Table 3.7: Summary of results from calibration with fixed polarization signal incident on all detectors simultaneously for an input polarization angle of -58.0° in the cryostat symmetry coordinate system.

differentials from this fit are shown in the middle and bottom panels.

Error bars in Figure 3.35 are shown as a simple standard deviation of all of the values of α_{in} measured during each 250 s segment. We note the spread in means is greater than the standard deviation error bars suggest it would be purely from statistics; we find in section 3.10.3 that these error bars are actually over-estimates already, and that simulation suggests errors on the mean are actually significantly smaller than these error bars. We conclude that in this calibration test the errors on the mean are not due to detector noise but to some other systematic effect; we propose that the most likely is our single-pole time constant assumption, which we investigate in section 3.11.3. We consider the signal to noise in greater detail in section 3.10, and summarize the errors from all sources in section 3.14.

We summarize the results in Table 3.7. The left-hand column represents the output of our polarization angle analysis for a time-constant corrected detector at the focal plane center for an input polarization angle of -58.0° in the cryostat symmetry coordinate system. The standard deviation of the measured detectors is given in the center column. We also note the observed slope of the line fit to the azimuth position of the detectors. Overall, our results from this calibration test result in higher errors than desired. We believe this to be a consequence of an overly bright source that resulted in many detectors with apparently saturated, non-linear behavior, as well as relatively warm detector temperatures; we suggest these situations lead to departures from the single-pole time constant assumption (investigated in sections 3.11.3 and 3.11.1). We conclude there is a rotation in our measured angle as a function of detector azimuth position, and we compare the absolute results of this test to our absolute predictions and polarized beam map results in section 3.12.1.

3.8.4 Cut detectors

We examine which detectors were not included in the preceding analysis and why they were omitted.

Not all detectors produced results that were consistent with the applied polarization signal. Figure 3.36 shows a detector for which during some periods of time, in this example near $t = 60$

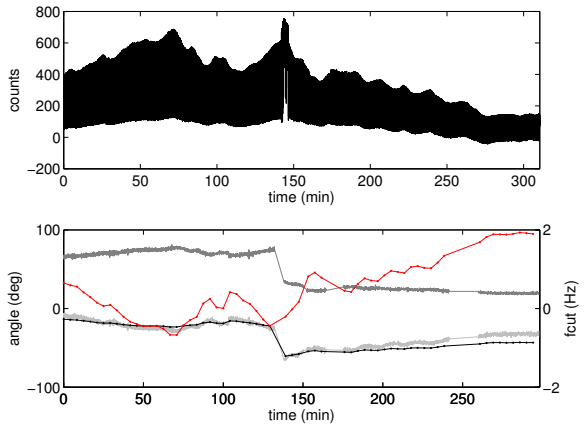

Figure 3.36: Results from a detector over the duration of the scan that fails to make our cut due to a non-physical value of f_{3dB}.

min, the polarization measured in the high sideband was more than ninety degrees behind the polarization measured in the low. This observation is not consistent with a detector whose time constant can be modeled as a single-pole RC-like filter. Since our removal method depends on this assumption, detectors that exhibited this behavior were cut. We exclude in this cut the last hour of data, during which drifting focal plane temperatures caused anomalous results for otherwise well-behaved detectors.

We found signal to noise for each detector by taking the power spectra of the detector data during a one-minute section during the middle of the calibration test. Signal is defined as the average value in a 0.3 Hz band around f_{chop}. Noise is defined by the average value of the next 0.1 Hz bands on each side of the signal band. While all detectors with discernible signal in the time domain, with a signal to noise level of 5, were initially included, those with a signal to noise level of 5 – 10 were strongly associated with the nonsensical results described in section 3.8.3 – detectors that could not be well modeled by a single pole, or detectors that did not show a rotation consistent with that applied by the source. Detectors in this signal to noise range were subsequently cut. These detectors may have fallen into a number of categories including those that were not well-coupled to the source optically, not properly tuned, or over the transition temperature.

Due to an inadequate early focal plane to refrigerator heat sinking design that was later corrected, the "v" focal plane was quite warm during this test. The "h" focal plane was ~ 280 mK while the "v" focal plane was ~ 400 mK. Despite this high operating temperature, after applying our cuts, we found approximately the same number of passing detectors on each focal plane. (Table 3.8). Regardless of their focal plane, wafers with a higher T_c fared better, with

wafer	focal plane	remaining (%)	N
150-03	v	62.5	5
150-09	v	77.8	7
150-15	h	60.0	6
150-20	h	57.1	8
150-24	v	60.0	3
150-41	v	66.7	28
150-43	h	76.9	30
150-48	h	53.8	7
250-12	v	78.6	11
250-23	h	52.2	12
410-13	h	71.7	33
410-18	v	80.0	36
	v all	73.2	90
	h all	66.2	96
150 all		75.8	94
250 all		62.2	23
410 all		67.1	69

Table 3.8: Number of passing detectors on each wafer. The percentage remaining is only for the cut due to non-single pole behavior. Detectors had already been cut such that S:N ¿ 5 as detailed above.

those wafers having more than 10 passing detectors averaging a T_c of 505 mK to the 428 mK value of those with fewer than 10 passing detectors.

3.8.5 Template in stare tests

We examine an alternate method of removing HWP "template" signal in our time streams as a check on our nominal method. The necessity of handling the existence of HWP template, a spurious signal in our data sets, was introduced in section 3.5.

Typically, it is removed by sideband band-pass filters in the data analysis process described in section 3.2, Figure 3.7, step [5]. However, we can forgo those filters also remove it using a fitting algorithm similar to that used on EBEX LDB data. In this method, data segments of 100 seconds are fit to sine waves of harmonics of f_{HWP} up to 16 f_{HWP}, and this fit is then subtracted from the original time stream. We analyze a single segment of data from the "big grid" data set twice, using the filter template removal process and the fitting template removal process, and compare the results.

We find that either method gives similar results in the measurement of α_{in} (Figure 3.37, left). For most detectors, the method does not have a strong effect on the measured α_{in}, but the filter method results in fewer outliers (Figure 3.37, right), resulting in errors on the mean of

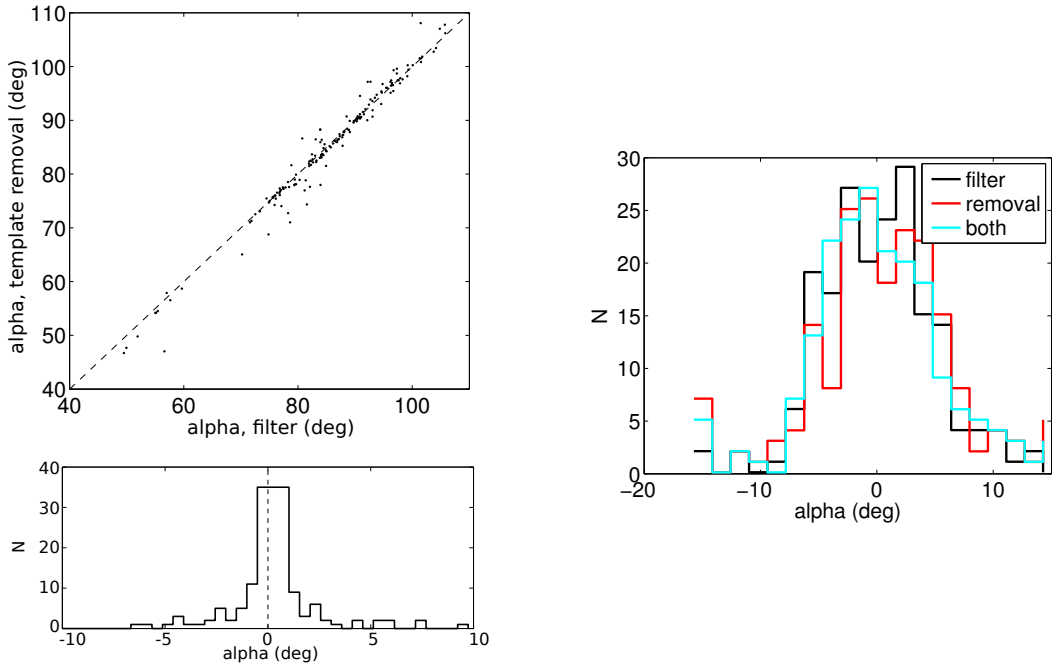

Figure 3.37: Left, top: Comparison of α_{in} measured with filter and template removal methods. Left, bottom: histogram of difference between measurement of α_{in} with filter and template removal methods. For most detectors, the method does not have a strong effect on the measured α_{in}, but the filter method results in fewer outliers (right).

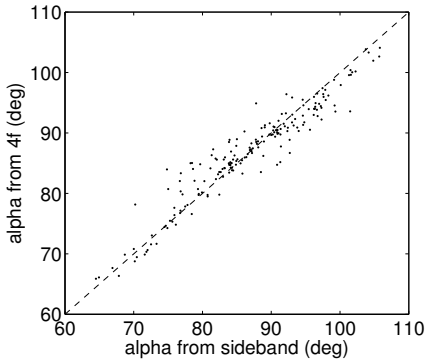

Figure 3.38: Comparison of measurement of polarization angle using data from the $4f_{HWP}$ peak to vs. the $4f_{HWP}$ sidebands

4.94°, 11.19°, and 11.77° for the filter method, the template removal method, and both methods respectively. For this reason we presented the results from the filter method in section 3.8.3.

This calibration test affords us an interesting opportunity to check our understanding of our chopped, rotating HWP calibration data sets. We show mathematically in section 3.1.3 that one could obtain the correct value of α_{in} from the $4f_{HWP}$ term alone if not for the possibility of unchopped polarized light entering the window. In this test, all of the light that enters the window is polarized at a known angle since the grid covers the entire window; thus, we should get the same answer using the $4f_{HWP}$ term. We can find α_{in} this way by bypassing the first demodulation multiplication step in Figure 3.7). Figure 3.38 indicates that the $4f_{HWP}$ term is largely equivalent in this calibration test.

3.9 Polarized Beam Scans

The Polarized Beam Scan calibration measurements represent the most fully integrated end-to-end test of the EBEX instrument. Beam scans of a distant point source are used to check the instrument's beam shape – detailed investigation of the beam shapes can be found in Zilic [34]. By rotating the HWP and using a polarized source, we simultaneously checked our ability to correctly measure the polarization of our calibration source. We seek to find our absolute calibration; we compare it to a predicted value in section 3.12.1.

By scanning the source, we measure the polarization of a point source with a moving gondola and all EBEX systems working in a flight-like mode of operation. We examine the differences in the measured value of polarization by different detectors, as well as variations in measured polarization across each individual beam.

To obtain an absolute calibration, we find an absolute reference between the source and the

cryostat. Consequently, when EBEX is used to measure the sky, a calibration will exist for what value α_{in} is reported, post-analysis, for a given physical input polarization. The absolute reference used is the gravity vector $\mathbf{g}$. By making measurements of the orientation of the source and cryostat relative to $\mathbf{g}$, we performed a calibration of absolute polarization rotation. Measurements of the EBEX hardware taken during its assembly and a theoretical understanding of the behavior of our optics allowed us to make a predicted mapping between a polarization orientation on the sky and the measurement of polarization produced by our instrument.

3.9.1 Experimental setup

EBEX far-field measurements are limited by the inability of the telescope to point lower than 18°. The point source used in EBEX beam scans was placed at the top of a nearby water tower visible by opening the high bay doors at the CSBF facility in Palestine, TX (Figure 3.39). This allowed us to place the source as far into the EBEX far field as possible. The source used was a Karlstrom source producing a narrow-band output at known frequencies in our observation bands.

During beam scanning measurements, the EBEX instrument was fully assembled with the exception of baffling meant to shield the instrument from the sun at float. Gondola pointing was fully operational. To assist in pointing, flood lights were installed near the source to act as targets for EBEX's star cameras. The STARS software used by EBEX for star camera pointing ([35]) allowed us to create a sky catalog featuring only the flood lights as "stars". Consequently, pointing with accuracy better than $1.5'$ was available during these scans.

We performed approximately 55 roughly rectangular scans over the course of 19 days, moving continuously in azimuth and stepping in elevation. We use software to find all of the beams that appeared to have signal and used the analysis pipeline detailed in section 3.9.5 to analyze each beam; we then performed the cuts detailed in section 3.9.9. Numbers of detectors observed during any individual scan ranged from one to 70, for a total of 134, 73, and 234 beams observed for 150 GHz, 250 GHz, and 410 GHz detectors respectively with some overlaps discussed in section 3.10.6 (we choose to keep these overlaps in the results in section 3.9.10 as they are independent measurements, but average them when comparing time constants across different calibration tests as in section 3.11.4).

3.9.2 Absolute Polarization Calibration

We used the following procedure to reference the source and instrument to the common reference of the gravity vector to achieve absolute polarization calibration.

The polarizing grid was glued to a mount with four high-precision machined dowel pin holes.

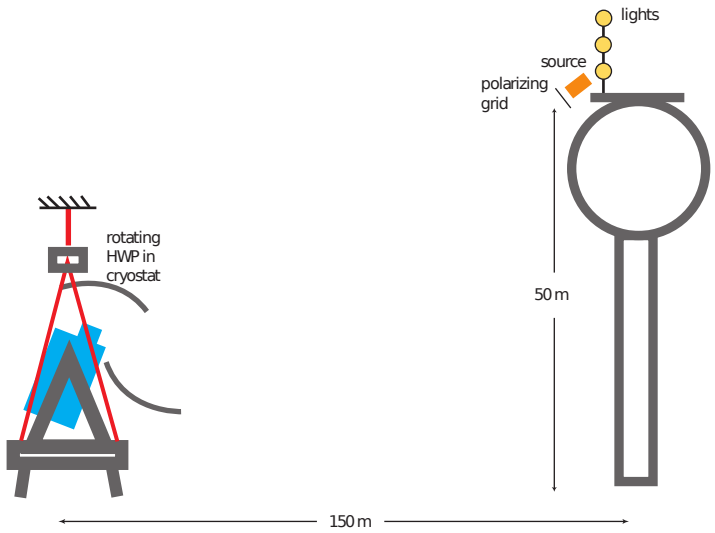

Figure 3.39: Setup of polarized beam scans calibration measurement.

Photographs taken with an SLR camera allowed us to reference the angle of the grid lines relative to the holes. The mounted grid was then affixed to a machined bracket that referenced to high accuracy the grid to a two-axis Measurement Specialties D-series inclinometer. The two angles registered by this inclinometer allowed us to measure the angle of the polarizing grid relative to **g**. An understanding of the geometry of the mount reveals that the angle of the grid's pass axis relative to **g** $\alpha_{\mathbf{g}-source}$ is related to the inclinometer outputs I_x and I_y by the equation

$$\alpha_{\mathbf{g}-source} = \arccos(-\sin I_x \cos I_y). \tag{3.43}$$

An identical inclinometer and a similar process are used to reference the cryostat to **g**. We measure to tooling balls at the top of the optics stack whose coordinates are known relative to the internal cryostat optics. The geometry of the cryostat inclinometer mount gives the following relationship:

$$\alpha_{\mathbf{g}-cryostat} = -\arctan\left(\frac{\cos(\frac{\pi}{2} - I_x)}{\cos(I_y + \frac{3\pi}{4})}\right) \tag{3.44}$$

By using these relationships, we reference the input polarization to the cryostat coordinate system used in section 3.9.2, allowing us to make an absolute calibration measurement, and further, predict what we should expect based on the workings of the instrument. We discuss the absolute calibration results in section 3.12.1.

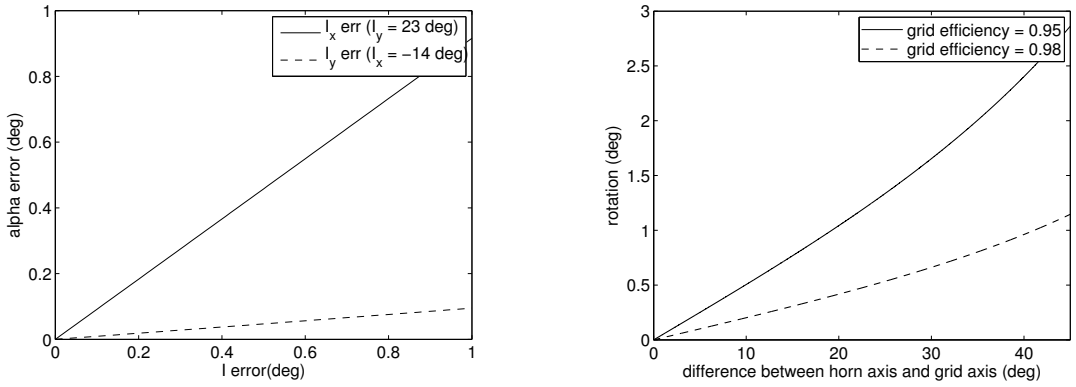

Figure 3.40: Propagation of errors in alignment of source for polarized beam scan calibration measurement. Left: error in polarization orientation $\alpha_{\mathbf{g}-source}$ vs. error in measuring inclinometer angles, in the largest-error configuration observed. Right: rotation in polarization orientation $\alpha_{\mathbf{g}-source}$ in the case of a grid efficiency of $< 100\%$ in the largest-error configuration.

3.9.3 Analysis of errors in measurement of source and cryostat orientation

We investigate the amount of error in the absolute measurements of the source and cryostat relative to the gravity vector $\mathbf{g}$ – the angles $\alpha_{\mathbf{g}-source}$ and $\alpha_{\mathbf{g}-cryostat}$ defined in section 3.9.2

The inclinometers used have an absolute accuracy of 0.04°. Using the relationship between I_x, I_y and $\alpha_{\mathbf{g}-source}$, we propagate this error. In Figure 3.40, values of I_x, I_y used are referenced from observed nominal values of 14° and 22° respectively. It can be seen that error in I_x dominates, causing an uncertainty in the value $\alpha_{\mathbf{g}-source}$ of 0.04°.

A source grid that is not 100% efficient is another source of error. This is a consequence of the fact that the source has a rectangular feed horn and therefore outputs nearly 100% polarized light even before that light encounters the source's polarizing grid. In the case where the two are aligned there is no error. However, as one rotates the grid relative to the feed horn, error is induced (Figure 3.40, right). Scans were made with the grid set at 0° and 11.25° ; however, since the geometry of the horn is only accurate within 2° based on an analysis of the accuracy of the horn fabrication, it is prudent to use this as the lower number. Taking a conservative 95% for the grid efficiency, errors of 0.1° and 0.57° are expected respectively.

In addition to the error from the accuracy of the inclinometer and the error from a grid with less than 100% transmission, there is an estimated 0.06° due to machining tolerances. The total error on the value of $\alpha_{\mathbf{g}-source}$ in the 0° configuration is 0.12°.

A similar investigation can be made for errors in $\alpha_{\mathbf{g}-cryostat}$ (Figure 3.41, left). Nominal

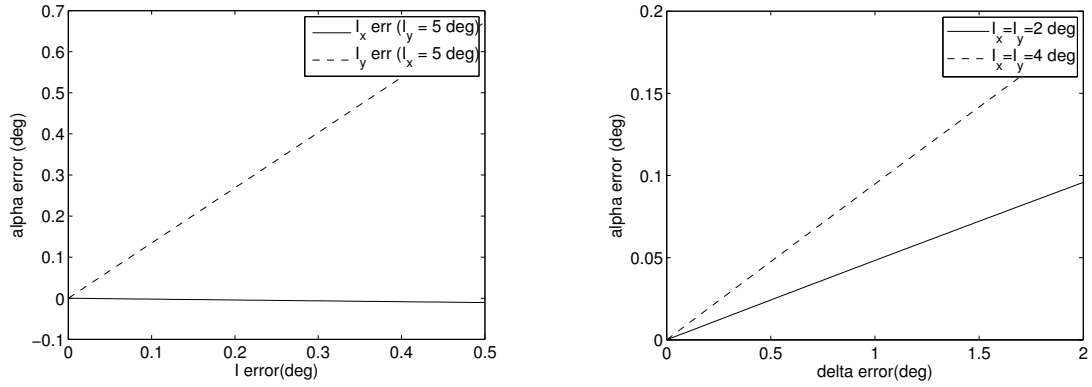

Figure 3.41: Propagation of errors in alignment of cryostat for polarized beam scan calibration measurement. Left: error in polarization orientation $\alpha_{\mathbf{g}-cryostat}$ vs. error in measuring inclinometer angles, in the largest-error configuration observed. Right: rotation in polarization orientation $\alpha_{\mathbf{g}-source}$ in the case of an unknown rotation ("δ") in the installation of the inclinometer relative to the cryostat.

values are taken as worst-case observed values of $I_x = 3°$and $I_y = 1°$. In this case, errors in I_y dominate, causing an overall uncertainty of $0.05°$ in $\alpha_{\mathbf{g}-cryostat}$. The cryostat inclinometer offers another source of possible error, an unknown rotation of the inclinometer around $\mathbf{g}$, such that its x-axis no longer aligns with the elevation axis of the cryostat. This angle is demarcated δ, and the propagation of error for this angle necessitates a more thorough examination of the geometry surrounding the mounting of the inclinometer (Appendix). While a perfect measure of the error is not possible, it is worth noting that a conservative estimate of $1°$ causes an uncertainty of $0.1°$in $\alpha_{\mathbf{g}-cryostat}$.

Adding in an error due to machining tolerance of $0.03°$, the total error associated with the measurement of the cryostat orientation relative to $\mathbf{g}$ is $0.12°$. We will find in section 3.12.1 that the values of errors discussed in this section are small compared to other sources of error.

3.9.4 Modifications to simulation

We explain the extensions to the simulation developed in section 3.1.4 (see Figure **3.4**) to make it suitable for simulation of polarized beam scans. The simulation includes scanning functionality that is turned off for use in simulating non-scanning calibration tests. Step 2 details the creation of Q and U time streams. In that section, they are functions of α_{in} that have the same value for the duration of the scan. In the more general model, they will change as the simulation scans over a high-resolution map. Thus, Step 2 of the simulation process is expanded as follows:

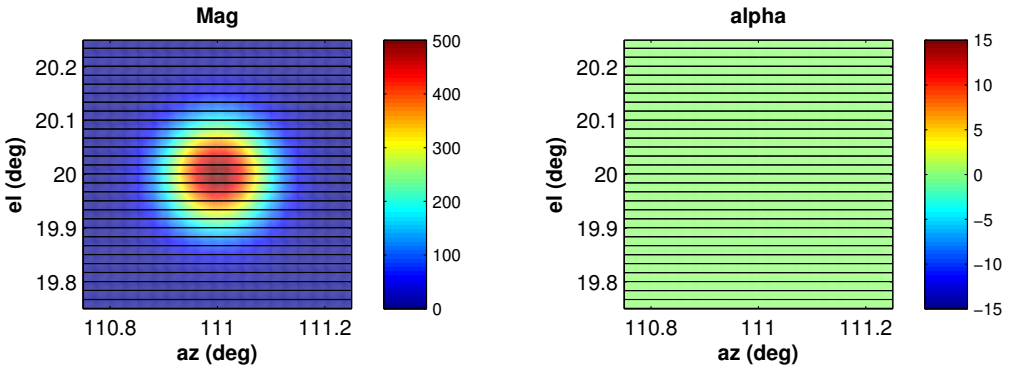

Figure 3.42: Maps produced by the polarized beam scanning simulation software. The left panel shows magnitude and the right panel shows polarization α_{in}. Black lines show the path of the scan across the beam; from this scan we produce a time stream for later analysis using the polarization analysis pipeline.

- A simulated pointing time stream is created. A function creates a roughly rectangular scan consisting of slow azimuth motion with intermittent steps in elevation, as is done in the beam scans. The function takes as arguments scan speeds and step sizes, which are chosen to be roughly equivalent to those used in the real scans. The result is two vectors: azimuth and elevation, each as a function of time.

- A simulated sky is created. This is a high-resolution two-dimensional map containing a Gaussian source at its center and a constant polarization α_{in} (Figure 3.42).

- The values of Q and U are evaluated using the simulated sky for each point in the azimuth and elevation time series.

- The simulation process then continues with Step 3 of section 3.1.4.

In the time domain, the course of the scan is shown in Figure 3.43. It can be seen that the scan moves across the beam in azimuth at each elevation, with increasing signal strength as the elevation moves to the center of the beam.

3.9.5 Data Analysis Pipeline

We follow the process detailed in section 3.2, with some differences to handle the moving from a "stare" configuration to a "scan" configuration. All filters used in this analysis are phase-preserving 2000 stage FIR filters with a total 3dB width of 1.125 Hz, a value chosen from the optimization procedure described in the next section.

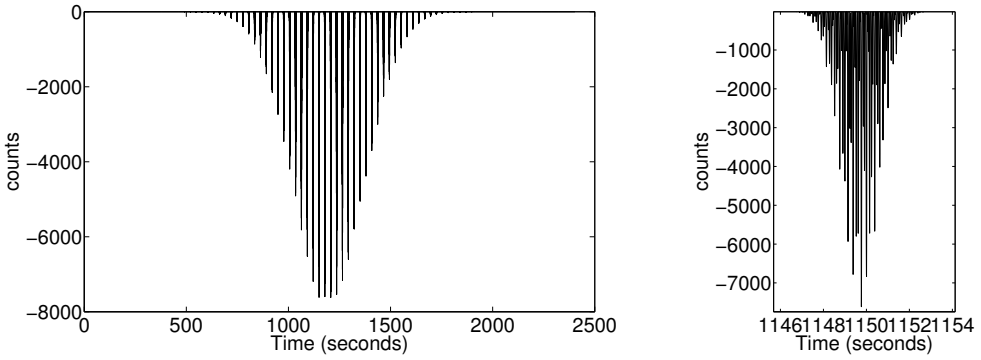

Figure 3.43: A simulated beam scan in the time domain; the entire scan is shown in the left panel, and a single pass in the right.

1. We filter the signal around the chop frequency f_{chop}.
2. We normalize this filtered signal to have a maximum value of 1.
3. We multiply the normalized, filtered signal by the original time series.
4. We low-pass this result. This is a power-only measurement.
5. We note azimuth and elevation pointing data for each bolometer data point by linearly interpolating the 100 Hz attitude data to the 191 Hz bolometer frequency. We use the power-only measurement from (4) to find the beam center by finding a 2-D Gaussian fit that allows for ellipticity. We note this beam center, as we will need it for time constant removal.
6. We now start over and follow the series of steps detailed in section 3.2 to obtain a value α_{low} and α_{high}. We take these values to be the magnitude-weighted average of α_{in} found in a radius of 0.04° from the beam center for demodulation of the low and high sidebands respectively.
7. We follow the time constant removal processes detailed in section 3.3.4, first doing the power-time methodology and then the phase methodology, using the power-time method to break the degeneracy in the phase method.
8. After deconvolving the data with a single-pole filter with the measured time constant, we restart the process again, following the steps detailed in section 3.2 to find α_{in}, again taken as the weighted average found in a radius of 0.04°. Since we use Q and U to find α_{in}, we now have I_p as well as the directly measured power I_{chop}, the standard deviation of the data points inside the nominal radius σ_α, and the beam center in Az and El, x and y.

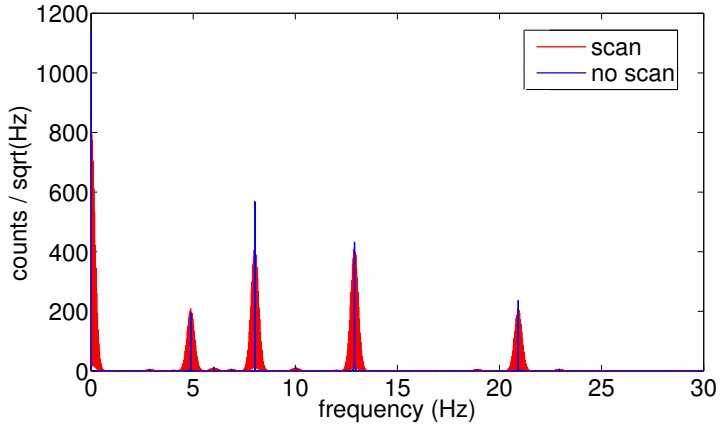

Figure 3.44: Spectra of scan vs. no scan simulated chopped polarization measurements

3.9.6 Optimization of filter width and sideband choice for scanning polarization tests

We choose filter widths for use in polarized beam scan data analysis. A look at simulated scan data in the Fourier domain illuminates one major difference between data taken during a gondola scan and data taken with a stationary gondola: the scanning motion makes peak widths greater in the Fourier domain (Figure 3.44).

Leaving the original filter width of 0.5 Hz that was chosen for non-scanning calibration tests clips the edges of these peaks. This results in striping in the final result, due to a small, opposite shift in phase for right-going and left-going scans (Figure 3.45).

It is also notable in that in the magnitude plot, the too-narrow filter stretches the beam in azimuth. Simulation verifies that a 1.25 Hz wide filter is adequately wide to avoid these unwanted effects.

The original intent of the filter was to avoid contamination by the template signal. A simulation, run with no noise or time constant but including a typical beam-scan sized template at various phase shifts, was run to ensure that the wider filter is still adequate in the elimination of this contamination (Figure 3.45, right).

We investigate the effect on the standard deviation in α_{in} when varying the filter width using a set of real detectors (Figure 3.46, left), and a simulation. The relationship is not strong, but choosing a filter width of 1.25 Hz allows us to avoid spurious effects seen at very low and very high widths in some detectors, and also avoid the striping issue mentioned above.

As in all calibration tests with a chopped source, we are free to choose which sideband, low, high, or both, to use for analysis. We predict that for sufficiently high levels of noise and

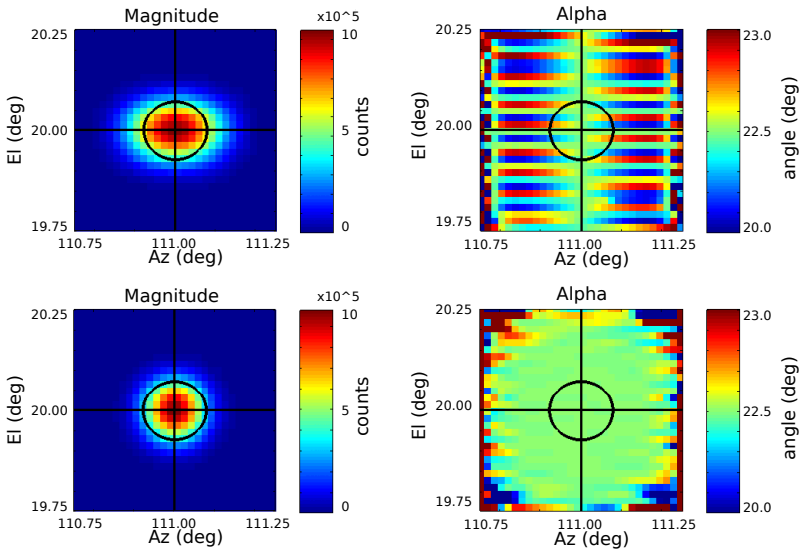

Figure 3.45: Left: Striping and beam ellipticity are evident when using too narrow of a filter (0.5 Hz) for beam scan analysis (top). Adequate filter width (1.125 Hz) removes these effects.

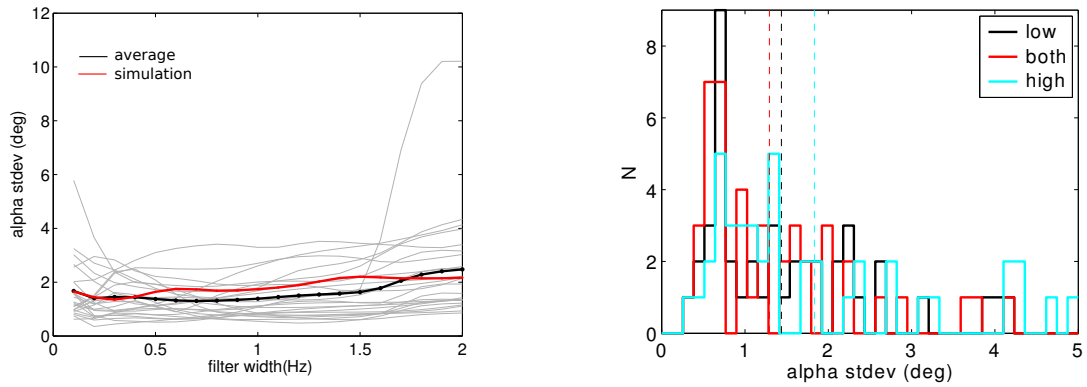

Figure 3.46: Left: 1σ standard deviations in measured value of α_{in} for a dozen real detectors (gray) and a simulation (red) from the stare calibration setup analyzed with different filter widths. Right: Standard deviations in α_{in} for selection of detectors in the stare calibration setup, using the lower, higher, and both sideband peaks for analysis.

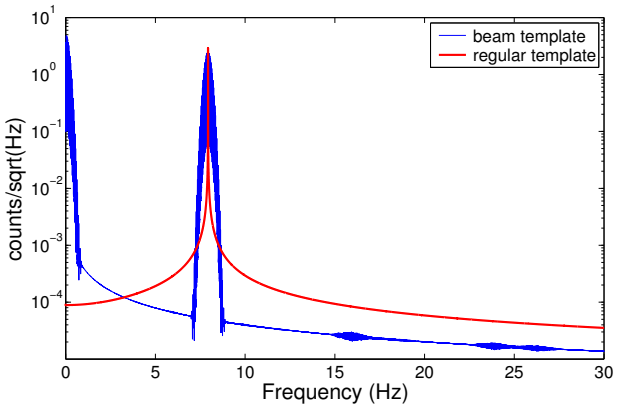

Figure 3.47: Comparison of template types with differing physical motivations.

sufficiently low values of optical time constant cutoff frequency, the value of using the higher sideband will be diminished. As in the "big grid" test, we find that using either the low sideband or both sidebands is not significantly different; the noise for the high sideband is slightly greater. (Figure 3.46, right). We stay with using the low sideband only to be consistent with the other calibration measurements.

3.9.7 Template in polarized beam scans

In section 3.1.4, HWP "template" signal is added as a set of sine waves at integer multiples of f_{HWP}. This mimics the behavior seen in the real detector time streams, and further is explainable by a physical model. Specifically, template observed at $4f_{HWP}$ is caused by unchopped polarized light that enters the cryostat, or is emitted by the cryostat from anything on the sky side of the HWP in the light path. This model still holds true for the case of scanning, but now another model is possible: light emitted by or near the source that is partially polarized but unchopped will be scanned and thus will exhibit a broader peak in the Fourier domain like the chopped signal served in Figure 3.44. We simulate this effect to check that it does not cause systematic errors in angle reconstruction (Figure 3.47). In each case the value of α_{in} is set to 22.5° while the phase of the template is set to 60° to ensure a contaminated result for α_{in} should the template leak into the reconstruction.

It can been seen in Table 3.9 that neither type of template reduced the ability to reconstruct the original value of α_{in}. Further, we stay with the filtering method rather than the template removal method discussed in sections 3.8.5 and 3.5, because the speed of change in the signal in time as we scan past the source is considerably less than the time length used for fitting in the template removal algorithm.

configuration	detected $\alpha_{in} - \alpha_{in}$ (°)
no template	-0.053
regular template	0.012
beam template	-0.003

Table 3.9: Error in observed value of α_{in} with various types of template

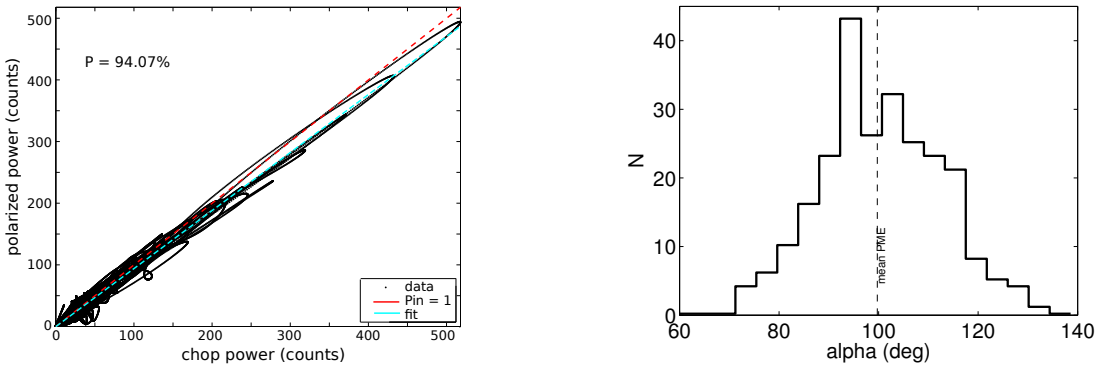

Figure 3.48: Left: example of PME for a single scan, which we take to the the slope of the power measured in the sidebands vs. the power measured at the chop frequency (cyan) over the entire scan. Right: PME measured for all polarized beam scans

3.9.8 Polarization Modulation Efficiency

We find that the polarized beam measurement gives us information about Polarization Modulation Efficiency (PME). We define PME as the fraction of 100% polarized input light that is detected as polarized by the instrument; it is a measure of EBEX's conversion of polarized light to unpolarized light.

For all data points during a scan, we measure the total power at the chop frequency I_{chop}. All input light falls into this band, regardless of whether or not it is polarized. We also measure I_p, the power of polarized light we detect. This signal originates from the sidebands and is simply the magnitude part of the angle α_{in}; $I_p = \sqrt{Q^2 + U^2}$ (we account for the multiplicative factors discussed in section 3.1.2). We can now calculate PME as:

$$PME = \frac{I_p}{I_{chop}}$$

Specifically, we plot all values of I_p vs. I_{chop} for the scan and take PME to the be slope of a linear fit. We show an example in Figure 3.48. For an ideal polarimeter this value would be 100%. We repeat the process on all scans, and cut 19 detectors that have a PME of >130% and clearly lie outside our distribution (while it is physically impossible for an individual detector to

have a PME value $> 100\%$, we consider the population as a whole). We suggest those detectors were cases in which the time constant was not found correctly, for example, cases in which the degeneracy discussed in section 3.3.4 was broken incorrectly. The remaining population of 247 scans is consistent with a PME of 100%; we find a value of 99.8% $\pm 0.8\%$. A more direct measure of PME can be found in Zilic [34].

3.9.9 Detector cuts

Beams are found by scanning through calibration data looking for chopped signal. All potential candidates are subjected to the full beam analysis pipeline. The following cuts are then made:

- Beams with an in-beam standard deviation of $> 5^\circ$ of the high sideband are cut, as are beams with a time constant of less then 1.5 Hz, for reasons detailed in section 3.3.5.
- Two scans with indications of timing problems are removed entirely.
- Scans that are shown to be saturated by the analysis process discussed in section 3.11.2 are removed.
- Scans with a PME outside the distribution, detailed in section 3.9.8, are removed.

During the time constant removal process, we calculate the amplitudes A_L and A_H of the low and high chopped sidebands respectively. We define their ratio $A = (\frac{A_L}{A_H})^2$. Since

$$B = f_{3dB}^2 = \frac{f_H^2 - A f_L^2}{A - 1}$$

we find two cases where $B < 0$, resulting in an imaginary value of f_{3dB} that we interpret as an indication the detector is a poor fit to our single pole model, namely

$$A > \frac{f_H}{f_L}$$

the case in which a detector is very slow, and

$$A < 1$$

the case in which the detector is very fast. With this observation, we make a final cut:

- Scans whose time constant is either so slow or so fast it does not fit the single-pole model are removed

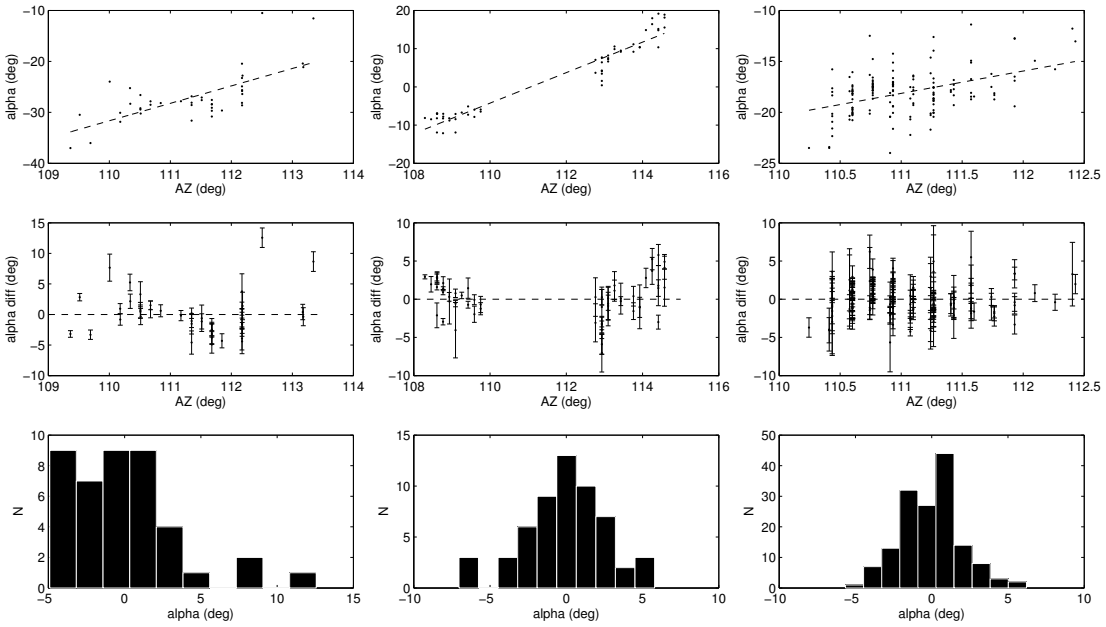

Figure 3.49: Plots for each of the detector frequencies 150 GHz (top, left), 250 GHz (top, right), and 410 GHz (bottom) showing the polarization measurement across the focal plane in azimuth for water tower scans. Top panels shows measurements corrected for time constant with a linear fit, with data points adjusted in the case of differences in the orientation of the source or the cryostat. Middle panels show differentials from the fit with error bars showing the standard deviation of the measurement for points inside a 0.04° radius from the beam center. Bottom panels are histograms of the differentials from the fit.

3.9.10 Results of polarized beam scan calibration

We show results for the polarized beams scans in Figure 3.49. For each frequency we show a plot of observed mean angle α_{in} vs. detector azimuth (top) for every detector scan, and perform a linear fit to this curve. We show the differential values from the fitted line in the middle panels, and a histogram of the differentials in the bottom panels. Error bars in the middle panels are a simple standard deviation of the values of α_{in} inside our nominal 0.04°beam; we discuss how this propogates to error on the mean using simulations in section 3.10.3 and summarize all sources of error on all measurements in section 3.12.2.

We summarize these results in Table 3.10. The first column shows the value of α_{in} observed at the center of the focal plane when the source and cryostat orientation are adjusted such that the effective incoming value of polarization is 90° with respect to the gravity vector, representing an input polarization angle of -6.8° in the cryostat symmetry coordinate system. The middle column is the observed standard deviation on the scans; this is the standard deviation for all

	α_{in}	α_{in} stdev	slope (alpha/az)
150	-25.4°	2.0°	2.2
250	3.00°	2.7°	4.0
410	-16.3°	3.6°	3.4

Table 3.10: Summary of results of polarized beam scan calibration test for an input polarization angle of -6.8° in the cryostat symmetry coordinate system (see text for explanation of columns).

scans in that frequency, correcting for their focal plane position using the linear fit. We show the observed slope of the linear fit for each detector frequency.

We achieve an absolute calibration for EBEX in its full configuration with a standard deviation among the detector scans on the order of 3.0°; we compare this to other calibration tests and to our absolute predictions in section 3.12.1.

3.10 Noise in calibration measurements

We seek to determine what statistical noise level to expect on our measurement of the polarization angle α_{in} given noise in our raw bolometer time streams, and to verify our analysis pipeline does not affect this noise in an unexpected way. Noise exists in our bolometer time streams during all calibration tests. This noise is a combination of detector readout electronics and optical noise, and is effectively white at relevant frequencies in the absence of large optical power ([36]). When analysis is run on EBEX calibration data, a value of the input polarization angle α_{in} is produced for each data point in the original bolometer time stream. These data points have a characteristic standard deviation and observed distribution. We trace the noise through the analysis pipeline using a combination of analytical calculation, simulated and actual calibration data.

3.10.1 Propagation of noise in time stream to noise in Q and U

We seek to understand the propagation of noise from the time stream to noise in Q and U after data undergoes analysis; specifically, we want to investigate whether the result matches a simple, unchopped model, where the noise observed in Q and U is simply a factor of $\sqrt{2}$ larger than noise incoming I_p. Even with a white noise input, it is difficult to work out the expected propagation of noise in the time domain to noise in Q and U analytically, due to the signal undergoing several multiplications and band-pass filters during the analysis (section 3.2).

We use our simulation to compare the noise input in the time domain to the noise in Q and U at the end of using our analysis pipeline (Figure 3.50). We assume this noise is not affected

by the bolometer's characteristic time constant (an approximation, as we find in section 3.3.5), and so we forgo the use of a time constant in this simulation. We define the noise magnitude by its standard deviation in counts; its value in counts is chosen to be similar to that of some real detectors, but for comparison to Q and U we multiply its value by 4 to account for the factors in equation 3.11. In this simulation, we fix the widths of our band-pass filters used in the analysis process at values of 0.4 Hz and 1.25 Hz for stare and scan cases respectively, but we allow the width of our final low-pass filter to vary. This final filter is the filter that separates our Q and U signals, which are near DC, from other higher-frequency components left over from demodulations during our data analysis process.

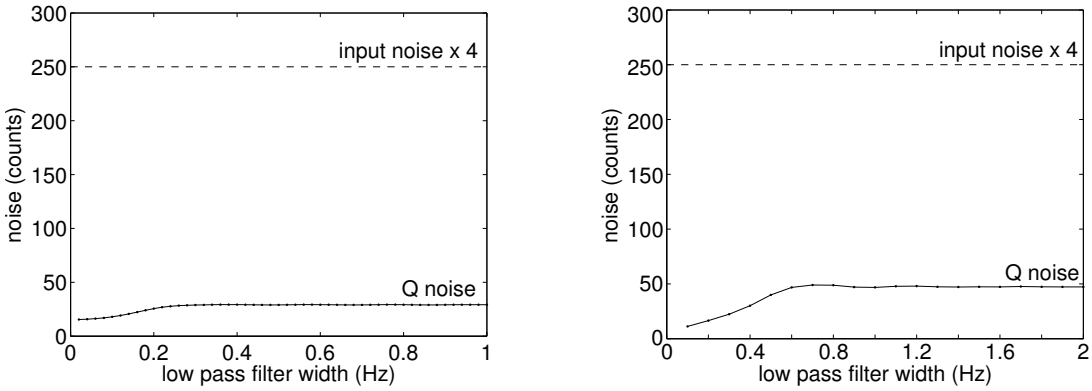

Figure 3.50: Noise in Q compared vs. low pass filter width compared to noise injected into original time stream (black dashed) for stare (left) and scan (right) cases. Input noise level is taken to be a typical observed value, in counts, and then multiplied by 4 to allow one-to-one comparison with Q (see equation 3.11). We fix all band-pass filter widths described in section 3.2 at values of 0.4 Hz and 1.25 Hz for stare and scan cases respectively.

We find that the noise measured in Q and U is considerably lower than that which was injected, since the latter was white noise and the lock-in technique used in the calibration measurements should only include noise in-band. The value varies with filter width, and it level levels off at higher frequencies due to the noise having already been cut down by band-pass filters earlier in the analysis process.

3.10.2 Propagation of noise in Q and U to noise in α_{in}

We consider the propagation of noise from Q and U to the polarization input angle α_{in} analytically.

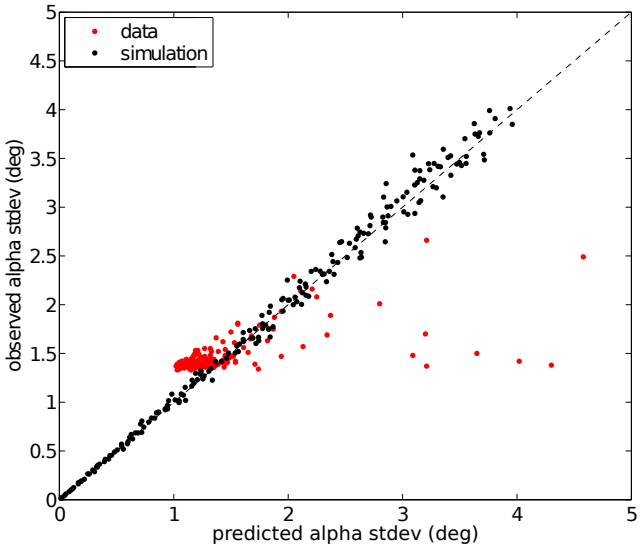

Figure 3.51: Error observed in alpha for a set of simulated stares and a set of real stares vs. error in alpha propagated from Q and U using equation 3.47. Data points that obey equation 3.47 exactly will fall on the black dashed line.

We use a general error propagation technique. Starting with the relation

$$\alpha(t) = \frac{1}{2}\arctan(\frac{U(t)}{Q(t)}) \tag{3.45}$$

and evaluating the error propagation formula

$$\sigma_\alpha^2 = |\frac{\partial\alpha}{\partial Q}|\sigma_Q^2 + |\frac{\partial\alpha}{\partial U}|\sigma_U^2 \tag{3.46}$$

it can be shown that the error in α with respect to noise in counts on Q and U is

$$\sigma_\alpha^2 = \frac{1}{4}\frac{Q^2U^2}{(Q^2+U^2)^2}\left(\frac{\sigma_Q^2}{Q^2} + \frac{\sigma_U^2}{U^2}\right) \tag{3.47}$$

This formula is demonstrated in Figure 3.51. We run a simulation with a 250 s segment of "stare" data at various noise levels. After running the analysis process, we compare the Q, U predicted value of σ_α^2 via equation 3.47 with the observed value of the standard deviation on α_{in} . We find that the simulation is consistent with the analytic noise propagation. We also plot values from real data observed during the "big grid" calibration test (section 3.8). This real data is also consistent, with two exceptions: an effective noise floor observed and discussed in section 3.10.4, and an over-estimation for some detectors that have drifts in the observed power,

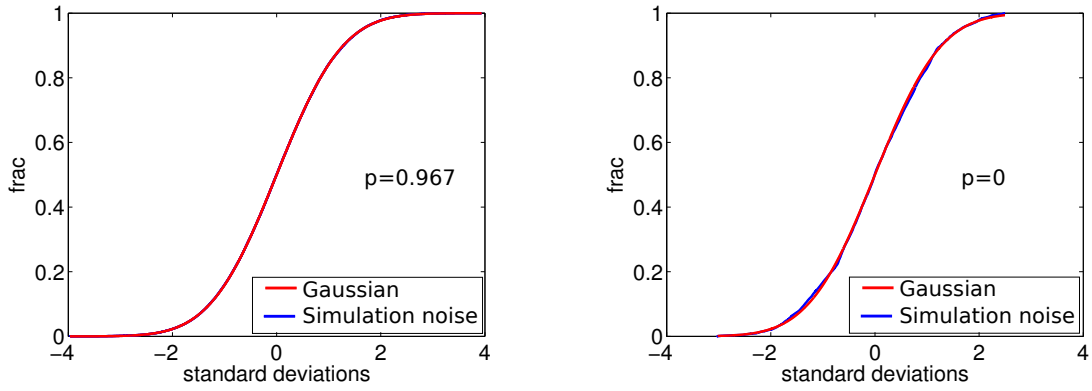

Figure 3.52: Left: the raw noise injected into the data during simulation is Gaussian as verified by a Kolmogorov–Smirnov test ($p = 0.97$). Right: the noise on Q after data analysis is no longer Gaussian ($p = 0$).

resulting in changing values of Q and U over the course of the scan.

3.10.3 Error on the mean and averaging

For the initial results of the "big grid" configuration test, in which the cryostat stares at a single polarized source, we produce results in 250 s segments; each segment is comprised of a reported value of α_{in} for every bolometer sample. In the case of beam scans, we collect points that fall within 0.04° of the center of the beam. In both cases we are left with many thousands of samples of α_{in}, the mean of which we take as our answer. We seek to find the statistical error on our mean based on these samples.

If one assumes the samples are perfectly Gaussian, after 250 s of data, a detector with a standard deviation of 1°would have its error on the mean reduced to $1/\sqrt{250sec \times 191samp/s} = 0.005°$.

Due to the analysis process, this is not the case. The Gaussian noise in Figure 3.52 is affected by the demodulation and analysis process, which requires several filters and multiplications (see section 3.1.3). When Q and U are recovered, the data is correlated and no longer passes a Kolmogorov–Smirnov test. Consequently, the error on the mean is not simply reduced by the square root of the number of data points.

We use the simulation to examine how the error on the mean behaves as the number of data points increases. For two noise levels and two configurations, a stare simulation and full scan simulation, we created 1000 realizations. In both cases the standard deviations on a single simulation are 0.92° and 1.84°. We then analyze segments of varying length from all realizations

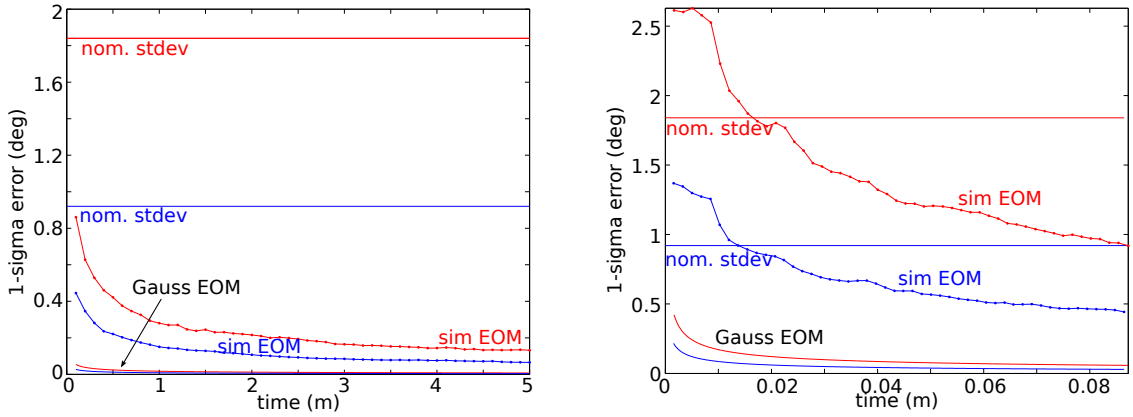

Figure 3.53: The reduction on the statistical error on the mean in the measurement of polarization angle α_{in} with increasing integration time. Lines are the values below which the error on the mean of 68% of 1000 simulation realizations fall for increasing analyzed integration time (see text). Shown are two levels of noise, where the observed standard deviations for a single realization are 0.92°(blue) and 1.84°(red). For each case, we also show the result with the assumption of Gaussian noise.

and find their means, up to 5 minutes in the stare case and 5 seconds in the scan case. 5 seconds is the typical time accrued by a detector inside our 0.04° nominal beam radius. Since we know our input value of α_{in}, we find an error for each realization by subtracting it from the reported value. In Figure 3.53 we plot the curves below which the error of 68% of the realizations fell. We also show the nominal standard deviation for a single detector, as this is the only value we have in the case of real data. We also show the Gaussian assumption for comparison.

We find that the error on the mean in both cases is below the nominal standard deviation but greater than the Gaussian assumption. In the stare case, we find that once 250 s have elapsed our error has fallen to about 10% of the standard deviation; with reported standard deviations on the order of $\sim 0.5°$, a value of 0.05° is insignificant with respect to our other sources of error. In the case of beam scans, we find that the error on the mean is almost exactly a factor of two below the standard deviation. We use these results when discussing all of the errors on our calibration measurements in section 3.14. We make a final note that our errors always scale linearly; no matter how the error is assessed, it increases by a factor two if the error input into the beginning of our simulation is increased by a factor of two.

3.10.4 Comparison of noise in stares and scans with simulation

In the previous section (3.10.3) we discussed how to map an observed value of the variation on α_{in} $-\sigma_\alpha-$ to an expected error on the mean. We now discuss what value of σ_α we should

expect to observe given the observed noise in a detector time stream, and the observed signal I_p. We assume in this section that our source is 100% polarized and our instrument's polarization modulation efficiency is 1.

In the case of polarized beam scans, σ_α is taken as the standard deviation of data points within a radius of 0.04° of the beam center. The noise level is defined by the standard deviation of the bolometer time stream that exists well outside the beam (>1°) after removal of the template. The signal level is defined by the fit to $I_p = \sqrt{Q^2 + U^2}$. In the case of non-scanning stare calibration configuration, the noise level is defined by the standard deviation of the bolometer time stream before the source and HWP rotation are turned on. The signal level is defined by the value $I_p = \sqrt{Q^2 + U^2}$recovered by the analysis.

We collapse these values of signal and noise into a single ratio, and create a simulation with various values of s:n. We analyze them and find the value of σ_α. We also analyze a set of real detectors from the "big grid" and polarized beam scan calibration tests.

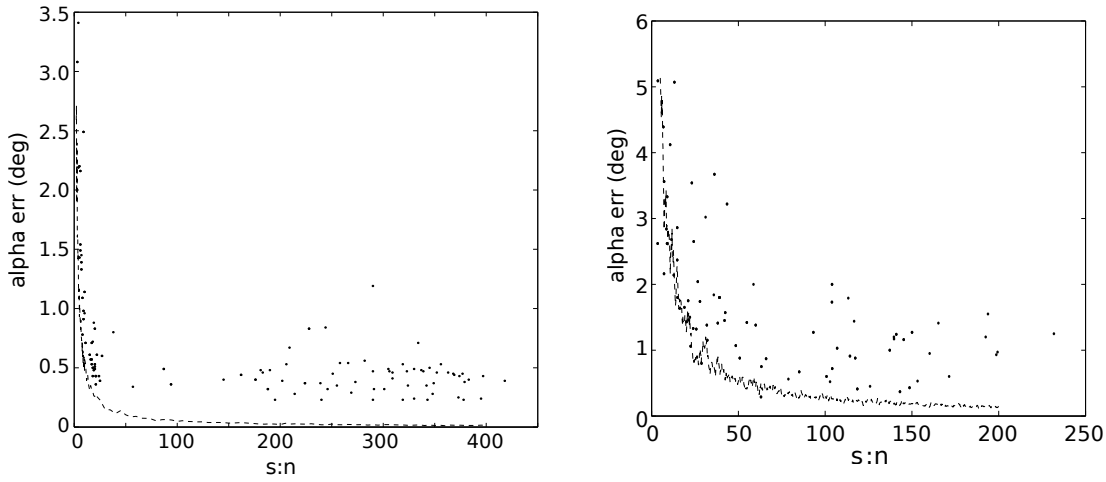

Figure 3.54: Standard deviation of α_{in} vs. signal to noise ratio for "big grid" stare configuration (left) and polarized tower scans (right). Dashed lines show results using the simulation.

Figure 3.54 shows the results of σ_α vs. signal to noise ratio, with real data shown as points and the simulation result as a dashed line. The data roughly fits the simulation: the error goes down as the s:n ratio goes up, and we find that the simulation is the minimum value of σ_α observed in the real data. The observed error is generally high compared to the simulation, especially at large values of s:n, which typically correspond to large signal levels.

An examination of power spectra gives a qualitative story about what is happening. Figure 3.55 shows examples of spectra from two detectors in the stare configuration. In the detector on the left, the noise floor from the data taken prior to operation of the source is close to that of

data taken during operation of the source. This detector shows a value of error on α_{in} close to the simulated prediction. The detector on the right has a considerably higher noise floor; in the case of detectors with very large signals, the noise floor is also raised. Our method of measuring noise thus underestimates the noise when the chopped source is on and the HWP is rotating.

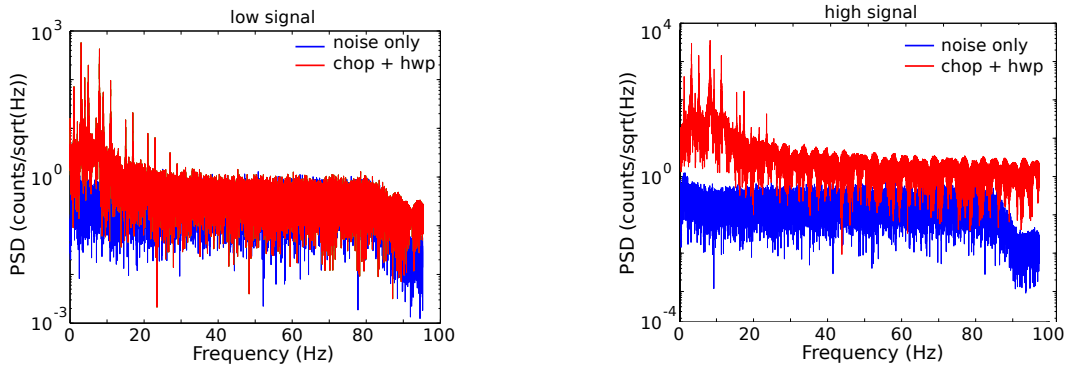

Figure 3.55: Left: spectra from a detector whose measured error in α_{in} is close to the predicted value during a "big grid" calibration test. Right: spectra from a detector whose measured error is an order of magnitude above the predicted value. In the blue curves, we show the section of data from before the HWP and chopped source were turned on; in red we show the data with the chopped source on and the HWP rotating.

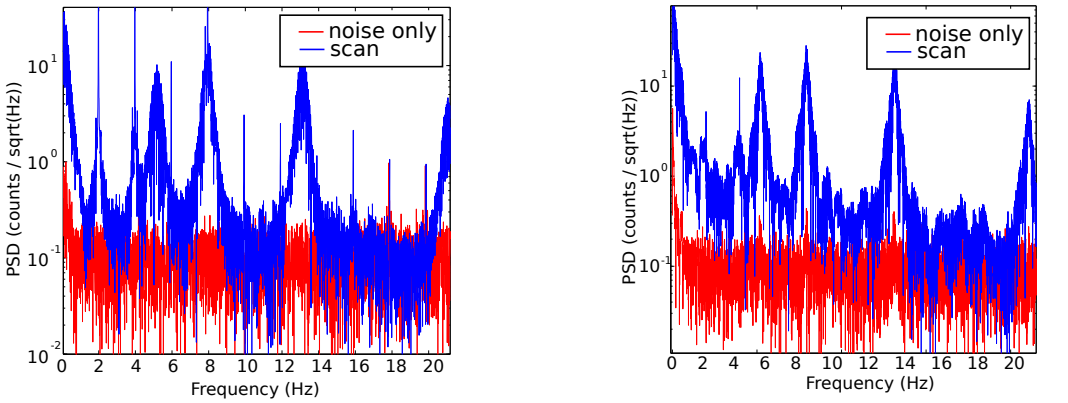

Figure 3.56: Left: spectra from a detector whose measured error in α_{in} is close to the predicted value during a polarized beam scan. Right: spectra from a detector whose measured error is an order of magnitude above the predicted value. In red we show a section of data taken far from the beam center; in blue we show a section of data taken near the beam center.

A similar though more subtle effect is observed during scanning tests (Figure 3.56). In

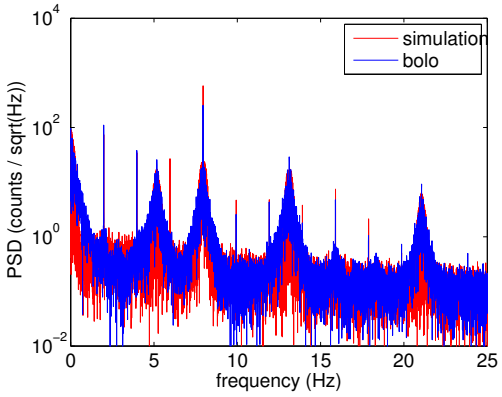

Figure 3.57: Comparison of simulation and real detector for a polarized beam scan calibration test.

particular, in the detector that has noise close to prediction, the noise between peaks is close to the noise floor. In the high-noise detector, there is enough power in the peaks that the noise between them never reaches the noise floor. Once again, in this case the noise is underestimated. Due to this effect, we find there is an effective floor to the value of σ_α in both cases of about 0.5° in the "big grid" case and about 1.0° in the scan case, regardless of how large the calibration signal is.

3.10.5 Noise in polarized beam scan maps

We illustrate the above sections with an example, by comparing a simulation created with the parameters from a real-life detector to that detector.

We measure the noise level in the real detector time stream away from the beam after removing the template, measure the size of the signal by running the analysis and fitting the beam, and measuring the bolometer's characteristic optical time constant f_{3DB} using our "phase" time-constant removal technique (section 3.3.4). These parameters are put into the simulation to create a model of the real detector.

We compare the spectra of the real and simulated detector time streams before analysis in Figure 3.57. After running the analysis pipeline on the data, we produce the maps in Figure 3.58. Two different methods are used here to visualize the result: on each line, the left two maps represent binned data, magnitude on the far left, and polarization angle in the middle left. The right two maps show measured angle for each individual hit, with the rightmost being a zoom-in of the entire scan shown in the center-right. All averages and errors are calculated by using a magnitude-weighted average of data in an 8 arc-minute ring surrounding the beam center. In this example, the real detector noise (σ_α) and the simulated noise are 0.42° and 0.43°

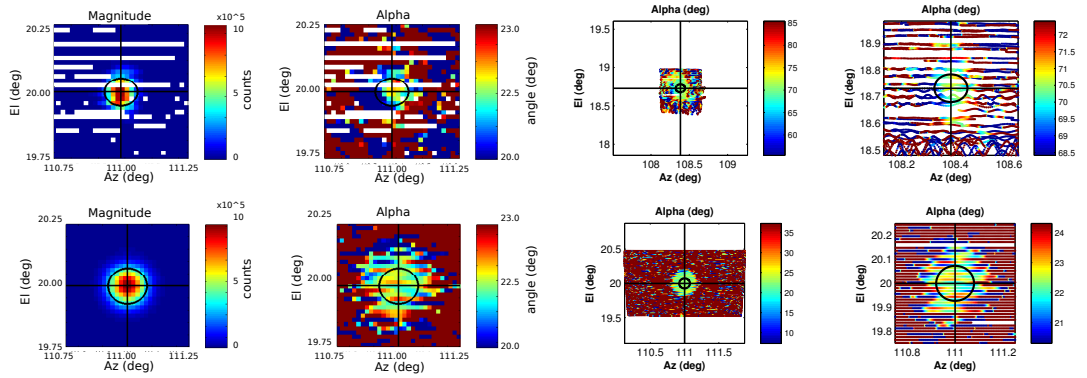

Figure 3.58: Resultant maps from water tower scans from a real detector (top) and its simulated model (bottom). Figures on the left are binned; on the right we show individual data points to show the scan pattern more clearly.

respectively. We conclude that it is possible characterize and simulate a detector using its signal, noise, and time constant.

3.10.6 Testing reproducibility using detectors with multiple scans

We use comparisons between the measured polarization angle results of detectors that were scanned multiple times ("revisits") to characterize the repeatability of our calibration measurements, and compare this repeatability to the assessments of standard deviation σ_α and error on the mean for individual detectors discussed in the previous sections.

Scan data was taken over a period of 19 days in July and August of 2012. Scans of different lengths were performed, from those taking only a few minutes and observing one detector to some lasting up to two hours and observing up to 65 detectors. We will sometimes separate revisits by day; the significance of this is that each day began with a new bolometer tuning and wafer temperatures that varied by up to 20 mK due to small changes in the fridge cycle and loading; the exact power of the source can also vary on different days. In 251 cases we observe the same detector scanned twice, 74% of the time on the same day. These observations are broken down by frequency as 9, 31, and 211 for 150 GHz, 250 GHz, and 410 GHz respectively (the relatively lower number of 410s led to more duplicate observations).

We first look at the revisit pairs taken all together (Figure 3.59.) We measure a mean value of α_{in} for every scan for every detector; we plot the difference between these values for two scans of the same detector. We observe a standard deviation in the difference in observed α_{in} of 1.8°. We consider standard deviation of the differences we expect to see by looking at the standard deviation measured within each beam scan σ_α (as in section 3.9.5, the deviation of the recovered

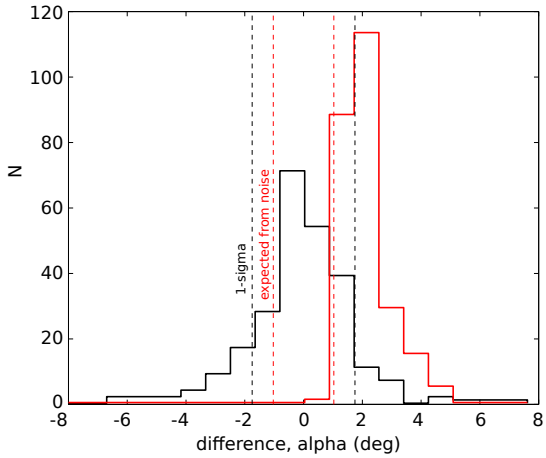

Figure 3.59: Difference in angle measured between revisit pairs (black) and observed standard deviations, added in quadrature, for each pair (red). The latter allows us to predict the level of difference in angle in revisit pairs (red dashed line) and compare it to the level observed (black dashed line).

angle α_{in} is taken for data points within a radius of 0.04° of the beam center). For the pairs, we add in quadrature the value σ_α from each scan. The result is over-plotted in red in Figure 3.59. Using the observation from simulation (section 3.10.3) that there is a factor of 2.0 between observed error on the mean of multiple scans and the observed standard deviation within the beam, we predict to see a standard deviation of 0.9° during revisits. We observe about half of our revisit difference in observed α_{in} can be predicted by noise in the angle measured in the beams. We suggest the remainder is systematic effects such as the error introduced by our approximate model of bolometer time constant (section 3.11.3). When we remove scans taken on different days (Figure 3.60), the standard deviation of the difference between revisit pairs drops to 1.4°.

We consider the observed time constants on each of the visits. Figure 3.61 shows time constant for the 410 GHz detectors, for which we have the most revisits. The revisits are correlated, even on different days, so long as the scans are taken from days the base temperatures are different by less than 5 mK.

Finding detector time constants depends on measuring the angle α_{in} for each the low and high sidebands (α_{low} and α_{high}; see section 3.3.4). Using the same-day, no-time constant removal scatter observed and referencing the curves in Figure 3.11 , we conclude that a large fraction of the same-day scatter observed in detected time constant is a predictable consequence of error in measurement of α_{low} and α_{high} (Figure 3.61, right).

Comparing detectors on days which a different temperature was observed (260 mK in visit

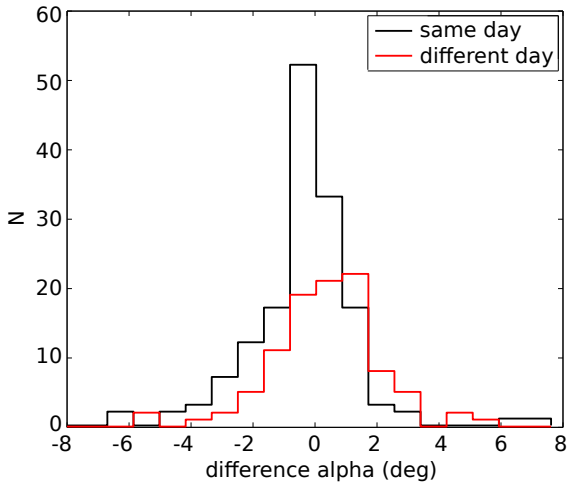

Figure 3.60: Difference in angle measured between revisit pairs broken down by day. Black is revisits that were taken on the same day, red on different days.

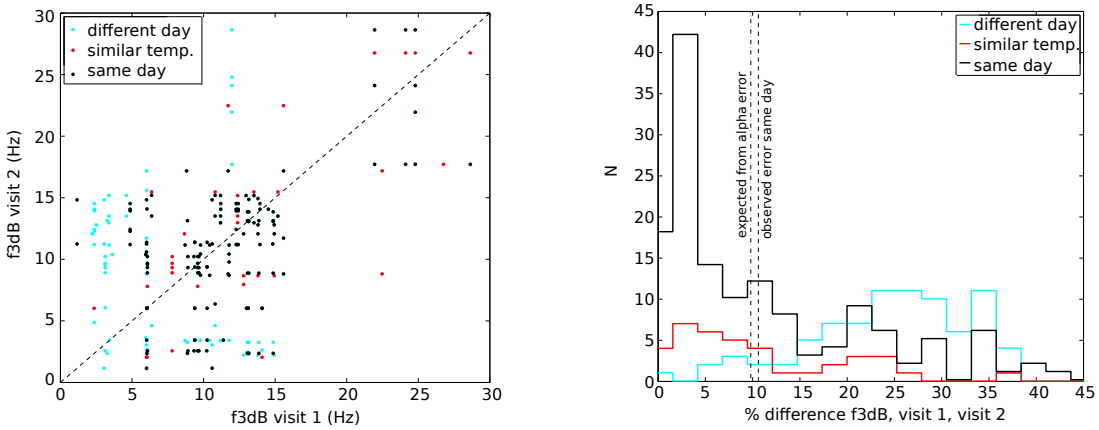

Figure 3.61: Time constants on revisits for 410 GHz detectors. Left: Time constant for first visit plotted against second. Right: Percent difference in measured time constant between revisits. Dashed lines show the same day observed mean percent difference, and the value predicted from considering how the observed error in α_{low} and α_{high} propagate to error in time constant.

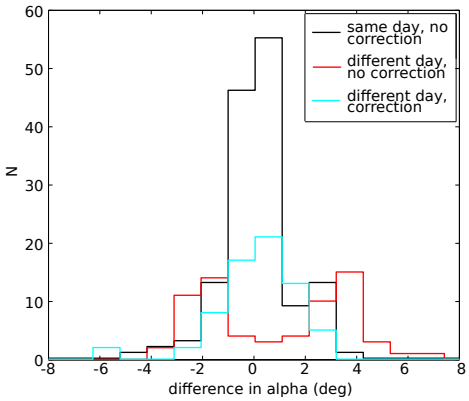

Figure 3.62: Difference in angle measured between revisit pairs for 410 GHz detectors in the cases of same day revisits, revisits from different days with no time constant removal, and revisits from different days with time constant removal.

1 vs. 245 mK in visit 2) we observe inconsistency between the measured time constants (Figure 3.61, cyan); specifically, detectors are slower on the warmer day. Applying time constant removal allows us to observe consistent angles between these visits (Figure 3.62).

We compare revisits for 150 GHz and 250 GHz detectors (Figure 3.63) and find consistency between revisits when comparing detectors taken on days with < 5 mK difference in wafer temperature.

We also compare results for "overlapping" detectors, which are defined to be detectors with the same pointing on the sky but on opposite focal planes (Figure 3.64). All but two of these cases are 410 GHz bolometers; the other two are 150 GHz. With or without time constant removal, these overlapping cases are consistent with a prediction of 90 degrees difference between the focal planes. We see a small bias in the corrected values. One possible reason for this is an offset in the physical position of the focal plane; in this case our observed slope of observed angle relative to detector azimuth (section 3.9.10)would create such a bias. Another possibility is that the detectors on one focal plane are a better fit to our single-pole model (section 3.11.3).

3.11 Observed detector time constants

3.11.1 Time constant as a function of wafer temperature

We show that a simple bolometer model predicts that bolometer time constant will be a function of wafer temperature. More thorough bolometer models can be found in Hubmayr [31]. Figure 3.65 illustrates our model. The bolometer consists of a spider web absorber with a transition edge

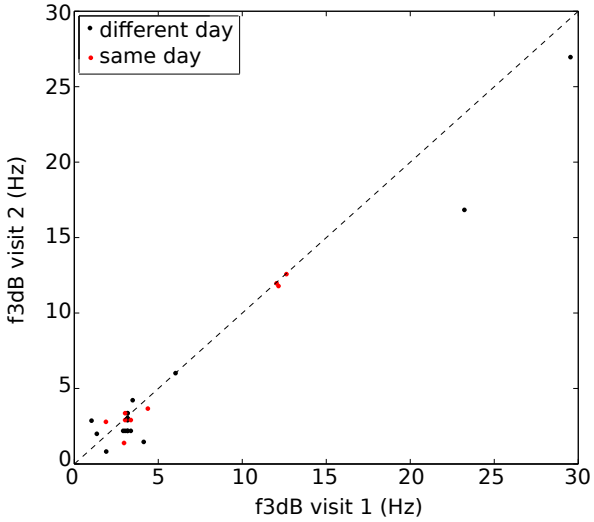

Figure 3.63: Time constants for revisits of 150 GHz and 250 GHz detectors, first visit plotted against second

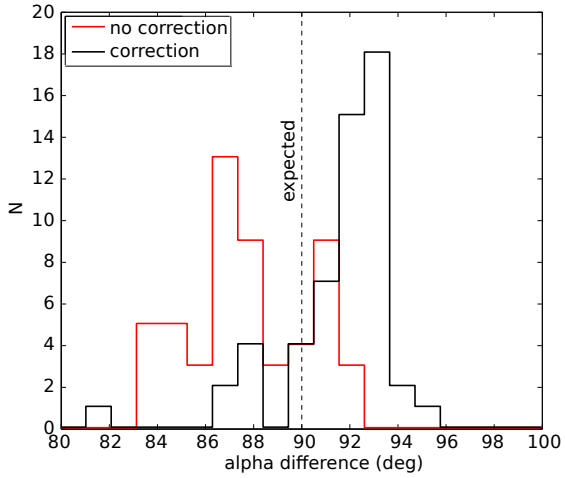

Figure 3.64: Difference between measured angles on detectors from H and V focal planes with same pointing on the sky, with and without time constant correction. A value of 90° is expected.

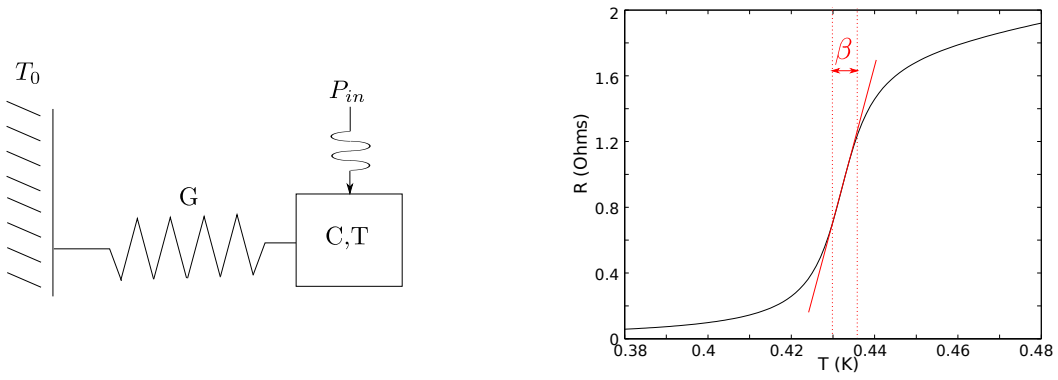

Figure 3.65: Left: A bolometer model shows the transition edge sensor as a thermal mass with a weak thermal link G to a bath (wafer) temperature T_0. Power P_{in} is applied via the bolometer's web. The bolometer has a steep superconducting transition $R(T)$ that we approximate as linear (right).

sensor (TES) modeled as a thermal mass with a weak thermal link G to a "bath" temperature T_0, which we will measure as our wafer temperature. Power $P_{in}$is absorbed in the web and coupled to the TES. The model suggests the following thermal balance equation:

$$C\frac{dT}{dt} = P_{in} + \frac{U^2}{R(T)} - G(T - T_0)$$

where U is a voltage bias applied dynamically to keep the total power constant and thus keep the bolometer in its linear regime (Figure 3.65, right). The bolometer is tuned to position it in the transition at a fractional depth defined by the ratio of its operating resistance R_1 and its normal resistance $R_N$such that $R_1 = \eta R_N$ with a corresponding nominal operating temperature T_1. We take into account the fact that G is a function of temperature, modeled with a power law such that

$$\tilde{G} = \tilde{G}^*(\frac{T}{T^*})^n$$

where $\tilde{G}^*$ is the measured thermal conductance at temperature $T*$ and n is measured to be between 2 and 3. Thus, the effective G is

$$G = \tilde{G}^*(\frac{T_0}{T^*})^n \frac{1}{n+1} \frac{(\frac{T_1}{T_0})^{n+1} - 1}{\frac{T_1}{T_0 - 1}}$$

and

$$G(T_1 - T_0) = \frac{\tilde{G}^* T^*}{n+1}\left[(\frac{T_1}{T^*})^{n+1} - (\frac{T_0}{T^*})^{n+1}\right]$$

which implies a bias voltage U of

$$U = \sqrt{\eta R_N \left\{\frac{\tilde{G}^* T^*}{n+1}\left[(\frac{T_1}{T^*})^{n+1} - (\frac{T_0}{T^*})^{n+1}\right] - P_0\right\}}$$

We define a dimensionless parameter α that approaches 0 for a saturated bolometer ($P_0 \sim (T - T_0)$) and is $>> 1$ in a nominal operating state where $P_0 >> G(T - T_0)$:

$$\alpha = \frac{U^2 \frac{\partial R}{\partial T}}{R_1^2 \tilde{G}_1} = \frac{U^2 \beta}{R_1^2 \tilde{G}_1 \eta^2}$$

in the case where we assume a linear transition with width β.

We find the bolometer responsivity $r = \frac{\tilde{I}}{\tilde{P}}$, where $\tilde{I}$ is the amplitude of an oscillating signal measured by the detector for given oscillating input light $\tilde{P}$ can be expressed in terms of α:

$$r = \frac{\alpha}{U(1+\alpha)}$$

We arrive at two measurable quantities, first, the relative responsivity sensitivity to base temperature

$$\frac{\frac{dr}{dT_0}}{r} = -\frac{\beta(\frac{T_0}{T_1})^n}{\eta(1+\alpha)^2}$$

and second, the effective time constant

$$\tau_e = \frac{\tau}{1+\alpha}$$

We show the results of the model in Figure 3.66. Our operating range during calibration tests was as planned for the H focal plane at 240–260 mK during beam scans, but running up to 287 mK during the extended-time "big grid" test (section 3.8). However, during Palestine 2012 calibration the V focal plane was typically 275–320 mK and as high as 400 mK. With the linear assumption, the normalized responsivity sensitivity to base temperature $\frac{\frac{dr}{dT_0}}{r}$ remains at values of less than 1%/mK until the wafer temperature is over 350 mK; it blows up quickly as the wafer temperature approaches the transition, a regime in which the value of $\frac{\frac{dr}{dT_0}}{r}$ becomes very sensitive to bolometer and tuning parameters. This suggests that a detector near its transition temperature, such as those on the V focal plane, will have relatively large changes in responsivity for small changes in wafer temperature.

The behavior of the time constant, and by extension the bolometer cutoff frequency, is

Parameter	Value	Units
T_c	0.432	K
$\Delta T = 1/\beta$	0.006	K
R_N	1.8	Ω
$\tilde{G}*$	42×10^{-12}	W/K
$T*$	0.380	K
C	8×10^{-12}	J/K
η	0.7	
P_0	2.35×10^{-12}	W

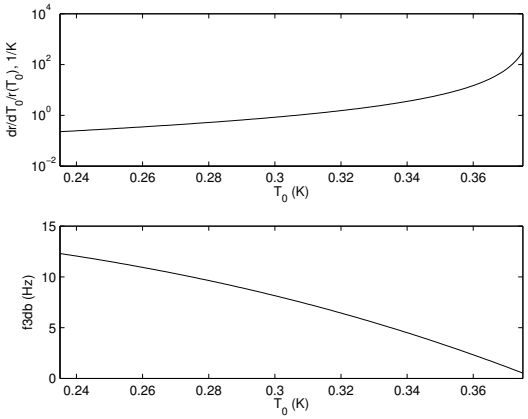

Figure 3.66: Left: Values used in bolometer model Right: Model predictions of relative responsivity sensitivity to base temperature (top) and effective time constant relative to base temperature (bottom).

considerably more linear, falling from its nominal value and approaching zero as the wafer temperature increases. Even within a normal operating area of 240-260 mK, this value varies 10 %.

We compare to this model data from the "big grid" calibration setup discussed in detail in section 3.8. This test had unusually high wafer temperatures, starting at 287 mK and 390 mK for the far wafers on the H and V focal planes respectively. Additionally, we were staring at an unchanging source for several hours, during which time the temperatures on the V focal plane climbed and oscillated with an overall delta of 15 mK. These conditions are ideal for probing the model discussed above.

Figure 3.67 shows typical results for detectors on each of the H and V focal planes. The peak to peak level and DC level are quite stable over several hours, although a change in time constant is observed when the wafer temperature increases. In the case of focal plane V, we see oscillations of peak to peak and DC level that are dramatic and are clearly correlated with wafer temperature; like the H detector, as the temperature climbs the detector becomes increasingly slow. We see clearly a qualitative consistency with our model.

We use peak to peak counts I_{pp} as a proxy for detector responsivity. A sample of responsivity vs. temperature curves for focal plane V is shown in Figure 3.68. We record the slopes $\frac{dr}{dT_0}$ linear fits and normalize by responsivity to obtain a histogram of $\frac{\frac{dr}{dT_0}}{r}$ (Figure 3.68, right). We obtain average values of 1.2 %/mK and 4.0 %/mK for focal planes H and V respectively. Extension of our model to use the non-linear $R(T)$ shown in Figure 3.65 predicts a value of 2 %/mK

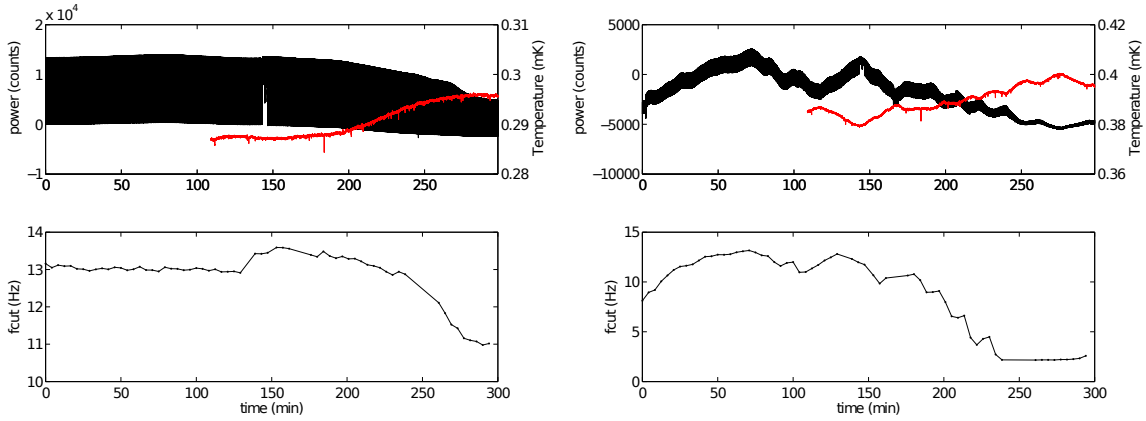

Figure 3.67: Left: Typical detector on focal plane H; top panel is raw time stream with focal plane temperature over plotted in red (right ordinate); bottom panel is detector time constant frequency cutoff f_{3dB}. Right: Typical detector on focal plane V.

and 11%/mK for the H and V focal planes respectively, although it is difficult to ascertain a number for focal plane V due to the extreme sensitivity to various parameters since the wafer temperatures T_0 are so near the transition temperatures T_c. We find that our measurements are consistent within the limitations of our model.

We measure the time constant for various temperatures (Figure 3.69) for all detectors averaged. Each temperature comes from a different 250 s data segment; we average all 186 available detectors (see section 3.8.4) and show 1σ error bars. Each focal plane shows a similar slope, as predicted by the model, although the data for focal plane V appears to break down as those detectors near T_c. Over a temperature range of 5 mK, the time constants for focal plane H change by about 5%. The model predicts 3% in this range (Figure 3.66).

3.11.2 Time constant as a function of incident power

We find that for a detector at a stable temperature, it is still possible to observe a variation in observed time constant. This is the case when high incident power causes the detector to leave its linear regime. We observe this effect during some beam scans. We investigate this effect and use it to make data cuts (section 3.9.9).

To investigate this effect, we run a beam calibration analysis on a detector following the process outlined in section 3.9.5. At the end of that process, the nominal beam is taken to be those data points within a circle of radius 0.04 degrees. Now we take concentric rings and follow the same process: within each ring we take the weighted average angle and the standard deviation. Following lessons learned in the simulation detailed in section 3.10.3, we take the

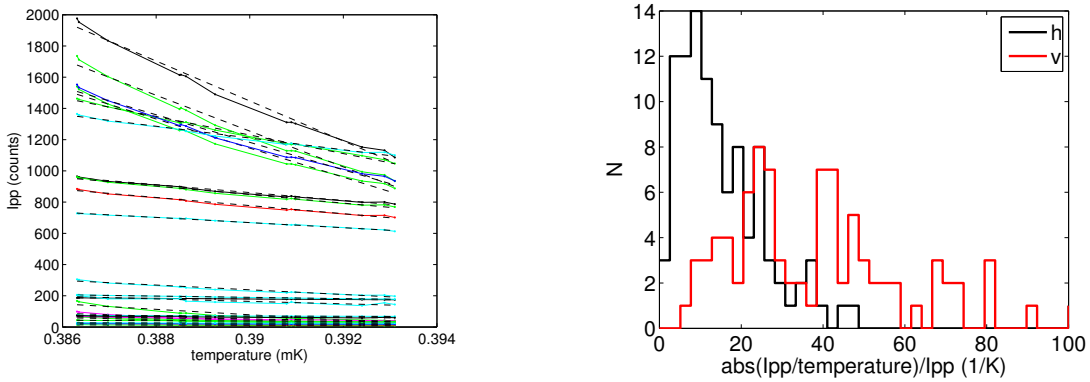

Figure 3.68: Left: A sample of detector peak to peak counts I_{pp} vs. temperature plots with linear fits. Right: Histogram of responsivity-normalized slopes of all detectors for focal planes H and V.

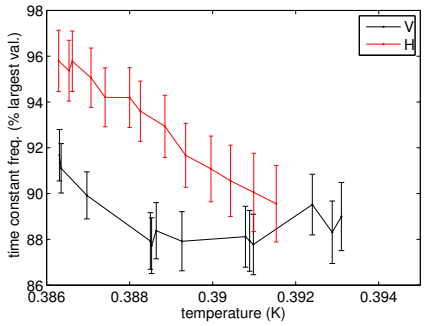

Figure 3.69: Detected time constant vs. wafer temperature. Data points are averages of 90 and 96 detectors for focal planes V and H, where each detector a time constant measured for one 250 s segment. Before averaging we reference each detector's data points to its largest value of f_{3dB}. We show 1σ error bars. Data for focal plane H is shifted +100 mK on the x-axis.

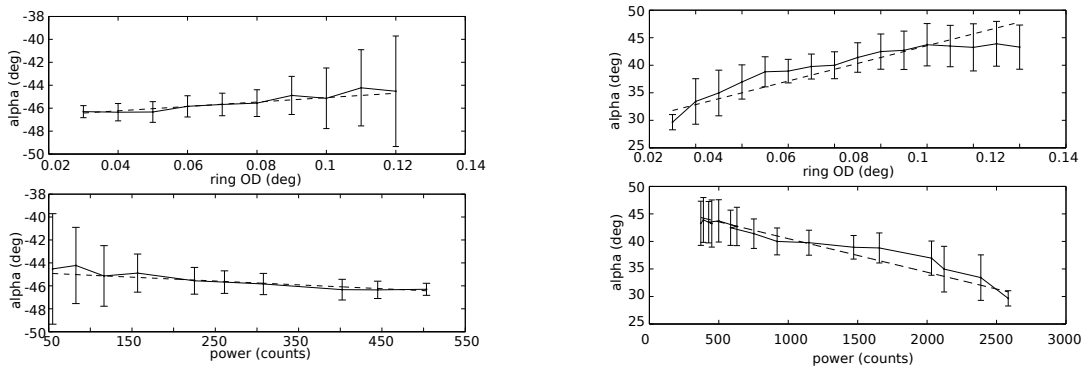

Figure 3.70: Average angle (y-axis) and standard deviation for specific detectors are analyzed at different sets of pointing, taken as rings starting from the beam center (x-axis). Bottom figures take the average measured polarized power in the ring as the y-axis. Left: typical detector shows no difference in measured angle α_{in} when taking cuts at different radii. Right: Some detectors show a significant effect

error on the mean to be half the standard deviation. For the majority of detectors, there is no significant difference in the observed angle α_{in} at large radii (although predictably the error increases). However, some detectors show a significant effect (Figure 3.70), with the reported value of α_{in} varying by 10° or more; typically, this angle increases as the radius increases, corresponding to a faster detector at lower incident power values I_p.

We make data cuts for the polarized beam calibration tests based on this observation. We examine the α vs. ring OD curves (top plots in Figure 3.70) and attempt to fit a line with a slope of zero. If this fit is excluded to 95% certainty, the scan is cut.

3.11.3 Direct measurement of time constants

As another probe of detector time constants, we measured the time constant response of the bolometers directly. We seek to find out whether our detectors have a rolloff profile that fits the single pole model we have assumed throughout our analysis.

We use the using the experimental setup shown in Figure 3.71. A chopped source illuminates part of the focal plane. The speed of this chop is varied from 1 to 40 Hz. A source was tuned to 150 GHz but the change in emissivity was sufficient to observe signal in all frequency bands. A photo diode is run into the HWP dfMUX board; its signal serves as a phase reference and we assume its time constant is much faster than our bolometers. We take into account the time delay between the two dfMUX board firmware versions detailed in section 3.6.1. 337 detectors pass a s:n cut of 75 at 13 Hz, where s:n is defined as the ratio of the peak height to the noise level in the frequency domain. We choose this level because fitting at high frequencies becomes

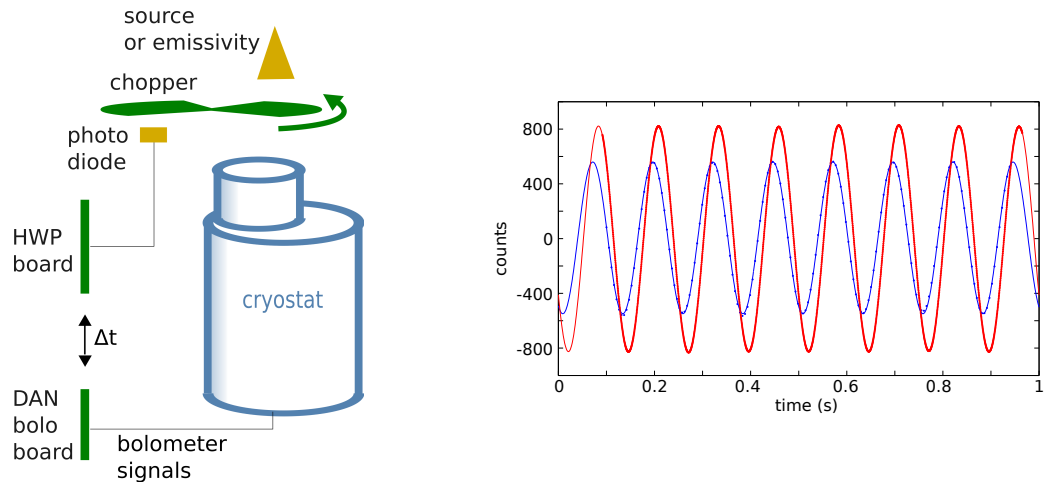

Figure 3.71: Left: Setup of direct time constant measurement. Right: Example of one step in the analysis process shows fitting of LED reference signal (red) and bolometer signal (blue).

increasingly unreliable at lower ratios s:n.

For each bolometer, for each chop speed, we fit to find the phase of the bolometer signal and photo diode signal. We record this phase difference and produce a plot of phase vs. frequency, examples of which we show in Figure 3.72. In some cases, the data fits the single-pole RC model very closely (Figure 3.72, top). In others, it serves only as an approximation (3.72, bottom). We refer to this test as the "direct phase time constant measurement" in later sections.

It is not clear that the detailed shapes of these curves are reproducible enough to use them to deconvolve each bolometer's filter for all other calibration tests; we find that a test of this method in our fixed polarization setup (section 3.8) yields significantly increased scatter in our resultant measured angles.

However, we use this data to make a statistical statement about the limitations of the single-pole assumption used to measure the time constant throughout this work. To investigate this question, we modify our simulation to create detectors with time constant phase behavior modeled after those we measured in this test. We then run our chopped calibration analysis code on the resultant simulated detectors, using our phase-based single-pole time constant removal technique. We record the value f_{3Db} obtained from this analysis, as well as the difference between the simulated angle and the value α_{in} we obtained after analysis. We repeat this procedure for each of the two chop speeds (3 Hz and 13 Hz) used in the fixed polarization and the polarized beam scan tests respectively.

In Figure 3.73 we compare the time constant observed after the simulation and analysis process to the best fit time constant from the direct phase test. We observe the degeneracy

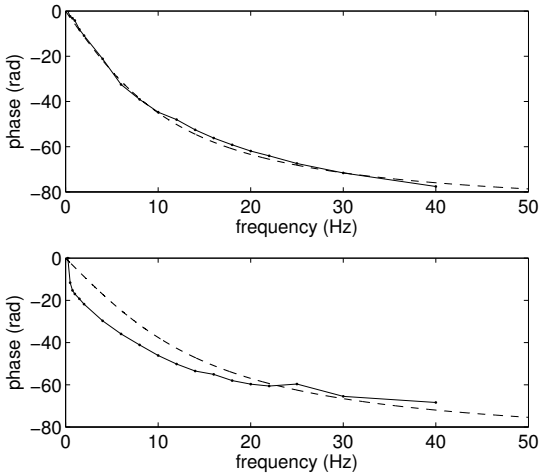

Figure 3.72: Frequency of chopped source vs. detector phase delay relative to optical reference signal (see text) for two detectors.

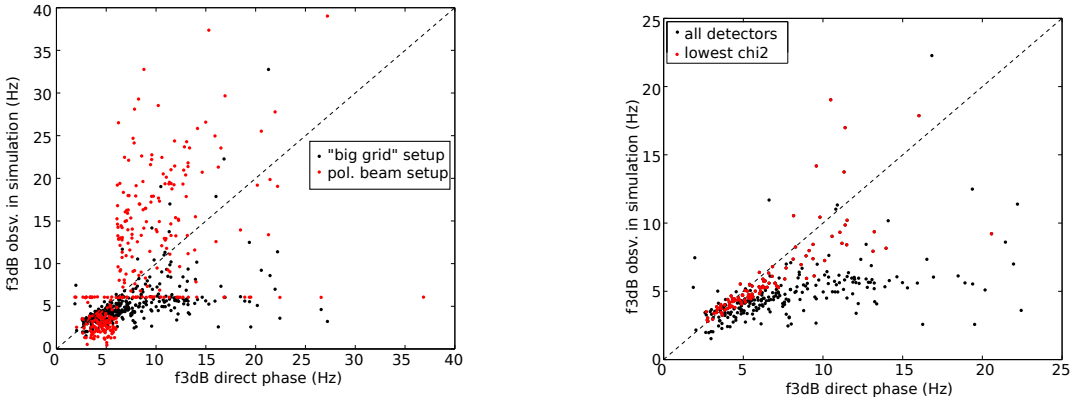

Figure 3.73: Left: Time constant observed after simulating each detector with its observed time constant phase curve and obtaining a time constant value using the phase method in our data analysis pipeline vs. the best fit time constant from the direct phase test. Deviation from the dashed line (slope= 1) illustrates the error intrinsic to making a single-pole assumption to find the time constant of a detector with a more complex response. Black has chop of 3 Hz, red chop of 13 Hz. Right: 3 Hz chop only, highlighting those detectors representing the lowest 30% chi-squared values observed in the direct phase test.

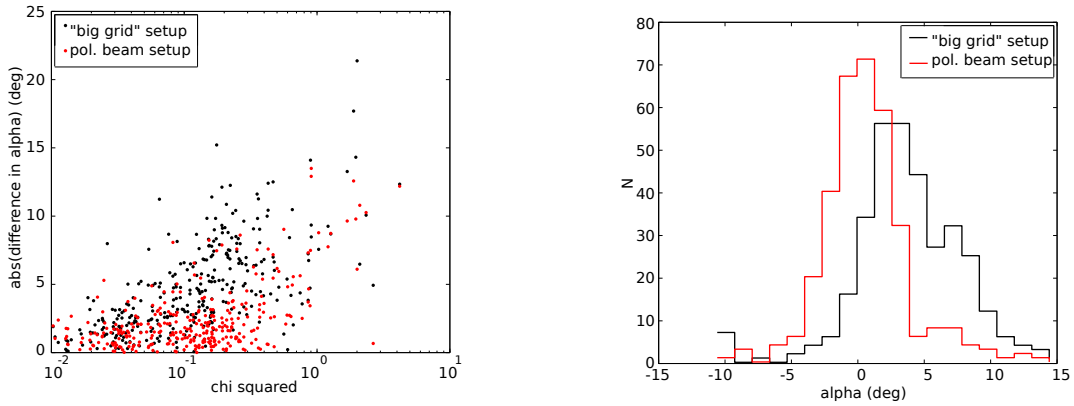

Figure 3.74: Left: Error in alpha observed after simulating and running analysis vs. chi-squared of fit during direct phase test. Right: histogram of error in alpha after simulating data with real detector phase curves and comparing to the direct phase measurement fit values; this is a histogram of the deviation from the line in Figure 3.73.

	"big grid"	polarized beam
150 GHz	4.1°	0.0°
250 GHz	1.5°	3.5°
410 GHz	1.9°	2.1°

Table 3.11: Bias due to assumption of single-pole rolloff in time constant correction process

in the 13 Hz case discussed in detail in section 3.3.2 (Figure 3.74, left). Moreover, we observe correlation as expected, which improves when selecting only those detectors with the best fits (the best 30% by χ^2) during the direct phase measurement (Figure 3.73, right).

The error in the single-pole assumption regarding the bolometer time constant propagates to an error in the observed angle α_{in}. In the case of a 3 Hz chop (big grid) time constant, we observe a standard deviation of 4.9° with a systematic offset of 3.5° (this same offset can be observed in the non-unity slope in Figure 3.73). The offset is a consequence of a systematic difference between the observed shape of phase vs. frequency curves and the single-pole assumption; most share the general shape of the bottom plot in Figure 3.72, steeper than the model at low frequencies and shallower at high. In the case of 13 Hz chop (as in the polarized beam scan test) we observe 3.2° and 0.6° respectively. We break the results down by frequency in Table 3.11.

An additional cross check is obtained by freeing up the time delay Δt between the HWP and bolometer dfMUX boards in the fit. We observe a value of 10.99±0.87 ms, consistent with the predicted value of 10.69 ms.

,

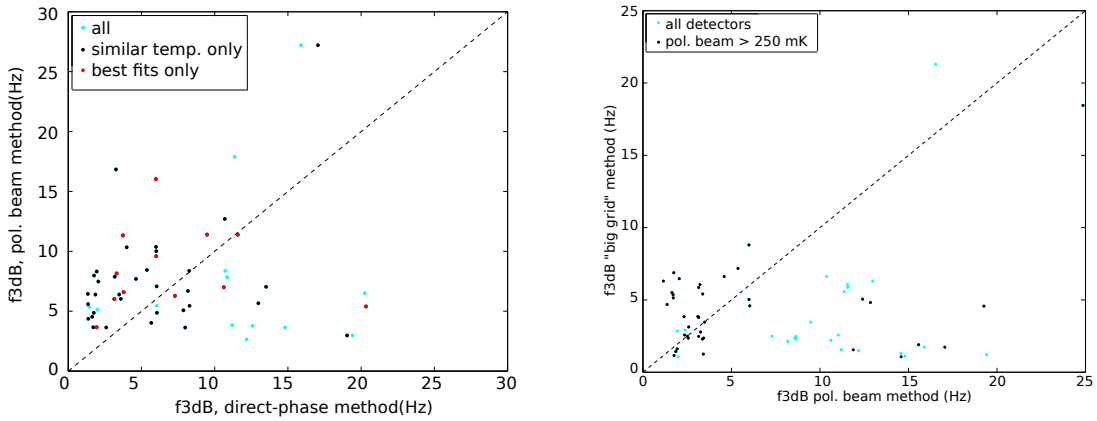

Figure 3.75: Left: Time constants measured in the direct phase measurement vs. the polarized beam scan setup. Right: Time constants measured in the big grid measurement vs. the polarized beam scan setup

3.11.4 Comparison of time constant across different calibration tests

We compare the observed bolometer time constants as measured across tests with different setups to see if a single time constant can be measured consistently for each detector. We compare measurements from the polarized beam scan setup (section 3.9) to those taken in the direct phase measurement (section 3.11.3) and the big grid measurement (section 3.8). In the case of duplicate scans in the beam scan test, we average the results.

In the former case, we can isolate scans which were taken within 6 mK of the direct phase measurement. Taking this cut in combination with 30% of direct phase measurements that yielded the lowest χ^2 fit values, we see some suggestion of consistency (Figure 3.75, left). Comparing to the big grid setup presents an additional challenge because the wafer temperatures during this measurement were 20 mK and 50 mK higher on focal planes H and V respectively than the warmest polarized beam scans. Still, we see that when isolating the warmest polarized beam measurements, the data suggests a repeatable time constant can be measured for some detectors, although some unexplained outliers remain. (Figure 3.75, right). While we see some indications of consistency, the variations in time constant observed with different focal plane temperatures and incident powers discussed in the previous sections lead us to not attempt to assign each detector a single time constant.

	nominal $\alpha_{in}{}^{\circ}$		**TC bias adj.**		**Band adj.**	**final** $\alpha_{in}{}^{\circ}$	
	pol. beam	"big grid"	pol. beam	"big grid"	pol. beam	big grid	"big grid"
150	64.6	72.8	-0.03	-4.10	2.40	67.0	68.7
250	93.0	89.4	-3.49	-1.51	0.00	89.5	87.9
410	73.7	74.1	-2.06	-1.92	1.05	72.7	72.2

Table 3.12: Summary of polarization calibration of EBEX

	polarized beam	big grid
150	-2.5	-4.1
250	-2.9	-3.2
410	-1.6	-2.0

Table 3.13: Summary of measured azimuth slope

3.12 Combined calibration results

3.12.1 Combined absolute results

We summarize the results of our two absolute calibration tests, the broad-band "big grid" stare test and the polarized beam scans, in Table 3.12. We begin with the focal plane center, time-constant corrected values presented in sections 3.8.3 and 3.9.10, subtracting the known value of incoming polarization in our cryostat symmetry frame. We apply two adjustments: first, the know time constant removal biases for each frequency and each configuration detailed in section 3.11.3, and further an adjustment based on our 4 K HWP model to account for the fact that our polarized beam scan single-frequency source was not set at the effective band center. We achieve our final calibrations, the values measured by EBEX when presented with incoming polarization parallel to the cryostat symmetry axis.

In Figure 3.76 we plot all calibration tests together and compare them to the value we expect to measure based on our instrument. We include the time constant bias adjustments to the data but not the band center adjustments (we plot them in the appropriate place on the x-axis). We show the Ebert-Fastie data in gray, adjusted vertically to best fit the absolute calibration data. We show the cold, warm, and directly-measured curves for our HWP (solid lines), adjusted vertically to best fit the absolute calibration data. Finally, we show our absolute prediction with no adjustment (dashed line), using the methodology discussed in section 3.6. We reiterate that error in the vertical placement of this curve is dominated by our ability to locate the HWP extraordinary and ordinary effective axes, as discussed in that section.

We summarize the slope of observed polarization angle vs. the detector's azimuth position on the focal plane in Table 3.13. We observe a similar effect in the broad band "big grid" and polarized beam scan calibration tests.

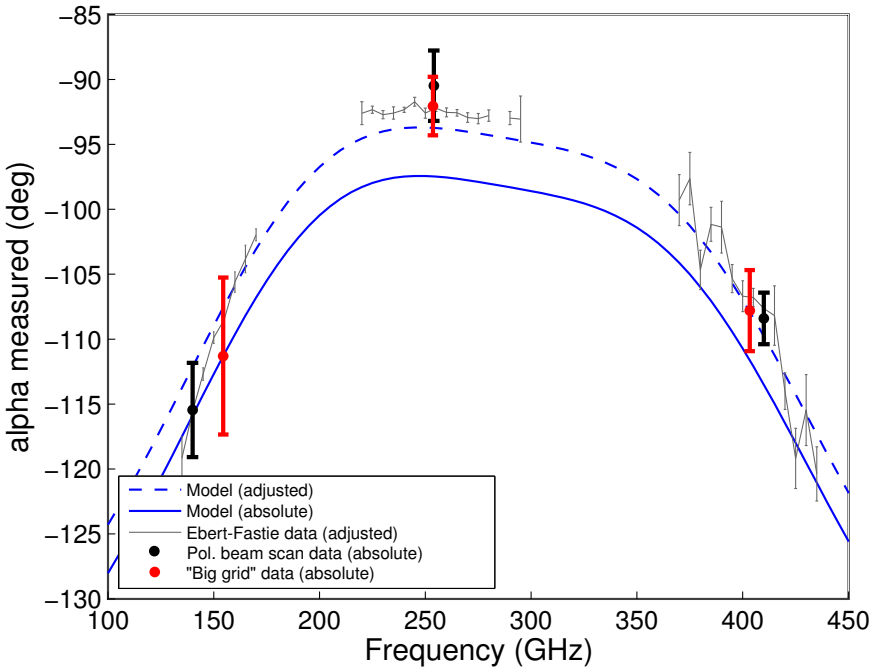

Figure 3.76: Absolute calibration, all tests combined. Big grid stare is shown in red, polarized beam scan in black; solid lines are HWP models and direct measurements adjusted to fit the data; dashed line is absolute prediction.

	polarized beam		big grid	
detector to detector variation				
statistical	1.0°	§3.10.3,pp.103	<0.1°	§3.10.3,pp.103
eff. increase (stat.) due to TC corr.	∼ ×2	§3.3.5,pp.54	∼ ×2	§3.3.5,pp.54
RC fit	3°	§3.11.3,pp.118	5°	§3.11.3,pp.118
calibrator orientation	<0.1°	§3.6.3.4,pp.68	<0.1°	§3.6.3.4,pp.68
absolute comparison to prediction				
calibrator orientation	<0.1°	§3.6.3.4,pp.68	<0.1°	§3.6.3.4,pp.68
HWP model/axis uncertainty	∼5°	§3.6.2,pp.68	∼5°	§3.6.2,pp.68
total expected variation				
revisits, same day	2.0°		-	
all detectors	3.4°		4.9°	
observed				
revisits, all	1.8°	§3.10.6,pp.108	-	
revisits, same day	1.7°	§3.10.6,pp.108	-	
all, absolute relative to prediction	+ 3.8°			§3.12.1,pp.123
relative rotation, error	-		1.9°	§3.8.3,pp.78
relative rotation, systematic	-		1.8°	§3.8.3,pp.78
error on mean, 150 GHz	3.6°	§3.9.10,pp.99	6.0°	§3.8.3,pp.78
error on mean, 250 GHz	2.7°	§3.9.10,pp.99	2.2°	§3.8.3,pp.78
error on mean, 410 GHz	2.0°	§3.9.10,pp.99	3.1°	§3.8.3,pp.78

Table 3.14: Summary of errors in calibration measurements

3.12.2 Summary of errors in calibration measurements

We compare the spread in angle observed in Figure 3.76 to that which we may expect based on detector noise (section 3.10), effectively increased noise due to the time constant correction process (section 3.3.5), and systematic errors such as departures from our nominal single-pole bolometer time constant model. We summarize these results in table 3.14.

We find that the spread in our calibration is dominated by our ability to remove detector time constant; specifically, by the departures of the actual detectors from our single-pole model. We are We find that the relative spread in the reported angles of our detectors in both calibration tests were consistent with the error we should expected when accounting for the sources of error investigated in this work. Error in comparing our calibration results to our absolute prediction is dominated by uncertainty regarding our HWP model and by extension knowledge of the position of the HWP effective axes.

References

[1] W. Hu and M. White, "A CMB Polarization Primer." *New Astronomy.* vol. 2 pp. 323 (1997)

[2] Dodelson, Scott, [Modern Cosmology], Academic Press (2003)

[3] BICEP2 Collaboration, "BICEP2 I: Detection Of B-mode Polarization at Degree Angular Scales," *Phys. Rev. Lett.* 112, 241101 (2014)

[4] M. Mortonson and U. Seljak, "A joint analysis of Planck and BICEP2 B modes including dust polarization uncertainty," arXiv: 1405.5857. (May 2014).

[5] Jones, T.J. and Klebe, D.I., "A simple infrared polarimeter," *PASP.* vol. 100, pp. 1158-1161 (1988).

[6] Richards, P.L. et. al. "The MAXIMA and MAXIPOL experiments," *AIP Conference Proc.* n. 616, p. 12-17 (2002).

[7] Oxley, P. et. al. "The EBEX Experiment," *Proc. SPIE Int. Soc. Opt. Eng,* vol. 5543 pp. 320-31 (2004).

[8] Sagiv, Ilan, et. al. "The EBEX Cryostat and Supporting Electronics." arXiv: 1005.3339 (May 2010).

[9] Reichborn-Kjennerud, B., et. al. "EBEX: a balloon-borne CMB polarization experiment," *Proc. SPIE Int. Soc. Opt. Eng,* vol. 7741 pp. 77411C (2010).

[10] Jarosik, N. et. al. "Seven-year Wilkinson Microwave Anisotropy Probe (WMAP*) observations: Sky maps, systematic errors, and basic results," *Astrophys. J. Suppl.* vol. 192, n. 2, pp. 14-29 (February 2011).

[11] Hanany, S. et. al. "Millimeter-wave achromatic half-wave plate," *Applied Optics*, vol. 44, n. 22, pp. 4666-4670 (August 2005)

[12] Hull, John R. "Superconducting Bearings," *Superconductor Science and Technology.* vol. 13, n. 2 (2000)

[13] Hull, John R. et. al. "Flywheel energy storage using superconducting magnetic bearings," *Applied Superconductivity.* vol. 2, pp. 449-455 (1994)

[14] Hanany, S. et. al. "A Cosmic Microwave Background Radiation Polarimeter Using Superconducting Bearings," *IEEE Trans. App. Supercond.* vol. 13, pp. 2128-2133 (June 2003).

[15] Hull, John R. et. al. "Characterization of a high-temperature superconducting magnetic bearing for use in a cosmic microwave background polarimeter," *Supercond. Sci. Technol.* vol. 18 pp. S1-S5 (2005).

[16] Matsumura, Tomotake et. al. "Magnetic Field Inhomogeneity and Torque in High Temperature Superconducting Bearings," *IEEE Trans. App. Supercond.* vol. 15, pp. 2316-2319 (June 2005).

[17] Bock, James Joseph. "Rocket-Borne Observation of Singly Ionized Carbon 158 μm Emission from the Diffuse Interstellar Medium" (PhD thesis, University of California at Berkeley) (1994).

[18] Palik, Edward D.; Ghosh, Gorachand.; Knovel (Firm), [Handbook of optical constants of solids], Academic Press, San Diego, pp. 761-779 (1998).

[19] Stoll, Richard L, [The Analysis of Eddy Currents], Clarendon Press, Oxford, (1974).

[20] Hull, John R. "Topical Overview: Superconducting Bearings," *Supercond. Sci. Technol.* vol. 13, pp. R1-R15 (2000).

[21] Shurcliff, W.A., [Polarized Light], Harvard U. P., Cambridge, (1966).Kulzer. G. et. al. "Cryogenic ratchet wheel drive for the ISOPHOT experiment," *Cryogenics*, vol. 27, n. 2, pp. 65-7, February 1987.

[22] Vallee, P. et. al. "Design of cryo-mechanisms for infared astronomy," *Proceedings of the SPIE - The International Society for Optical Engineering*, vol. 4841, pp. 656-66, 2003.

[23] Downey, C.H. et. al. "Arcsecond grating drive mechanism for operation at 4 K," *Cryogenics*, vol. 31, n.12, pp. 1030-7, December 1991.

[24] Nosaka, M. et. al. "Self-lubricating performance and durability of ball bearings for the LE-7 liquid oxygen rocket-turbopump," *Lubrication Engineering*, vol. 49, n.9, pp. 677-88, September 1993.

[25] Gould, S.G; Anderson, M. "Ball bearing lubricants for use in cryogenically cooled infrared telescopes," *Proceedings of the Low Temperature Engineering and Cryogenics Conference 1990*, pp. 06.1/1-6, 1990.

[26] Gould, S.G; Roberts, E.W. "The In Vacuo Torque Performance of Dry-Lubricated Ball Bearings at Cryogenic Temperatures," *23rd Aerospace Mechanisms Symposium; Huntsville, Alabama; USA; 3-5 May 1989*, pp. 319-333, 1989.

[27] Tomotake Matsumura. A Cosmic Microwave Background Radiation Polarimeter Using Superconducting Magnetic Bearings. Ph.D. Thesis, University of Minnesota, Twin Cities, 2009.

[28] John David Jackson. *Classical Electrodynamics.* Hamilton Printing Company, 1998.

[29] E. Hecht. *Optics*. Addison-Wesley, 1998.

[28] W.A. Shurclif. *Polarized Light*. Harvard U.P., Cambridge, 1966.

[30] J. Tinbergen. *Astrophysical Polarimetry*. Cambridge University Press, Cambridge, UK, 1996.

[31] Hannes Hubmayr. Bolometric detectors for EBEX: a balloon-borne cosmic microwave background polarimeter. Ph.D. Thesis, University of Minnesota, Twin Cities, 2009.

[32] Moncelsi, Lorenzo et. al. "Empirical modelling of the BLASTPol achromatic half-wave plate for precision submillimetre polarimetry," Monthly Notices of the Royal Astronomical Society, vol. 437, pp. 2772-2789, November 2013.

[33] Dan Polsgrove. Calibration of the E and B EXperiment (EBEX), A Balloon Borne Cosmic Microwave Background Polarimeter. Ph.D. Thesis, University of Minnesota, Twin Cities, 2009.

[34] Kyle Zilic. Calibration and Design of the E and B EXperiment (EBEX) Cryogenic Receiver. Ph.D. Thesis, University of Minnesota, Twin Cities, 2014.

[35] Chapman, Daniel. "STARS: A software application for the EBEX autonomous daytime star cameras," *Proceedings of the SPIE,* 2014

[36] Francois Aubin. Detector readout electronics for EBEX : a balloon-borne cosmic microwave background polarimeter. Ph.D. Thesis, McGill University, Montreal, Quebec, 2013

[37] Kevin MacDermid. Development and Performance of the Detectors and Readout of the EBEX Balloon-Borne CMB Polarimeter. Ph.D. Thesis, McGill University, Montreal, Quebec, 2014

[38] Didier, Joy. "The performance of the pointing system during the recent flight of the E and B Experiment (EBEX)". *Proc. IEEE Aerospace*, submitted. (July 2014).

[39] Britt Reichborn-Kjennerud. Building and Flying the E and B Experiment to Measure the Polarization of the Cosmic Microwave Background. Ph.D. Thesis, Columbia University, New York, New York, 2014.

[40] Milligan, Michael et. al. "Software systems for operation, control, and monitoring of the EBEX instrument," Proc. SPIE, vol. 7740, 774007 (2010).